

**PHASE DYNAMICS AND PHYSICO-MECHANICAL BEHAVIORS OF  
ELECTRONIC MATERIALS: ATOMISTIC MODELING AND  
THEORETICAL STUDIES**

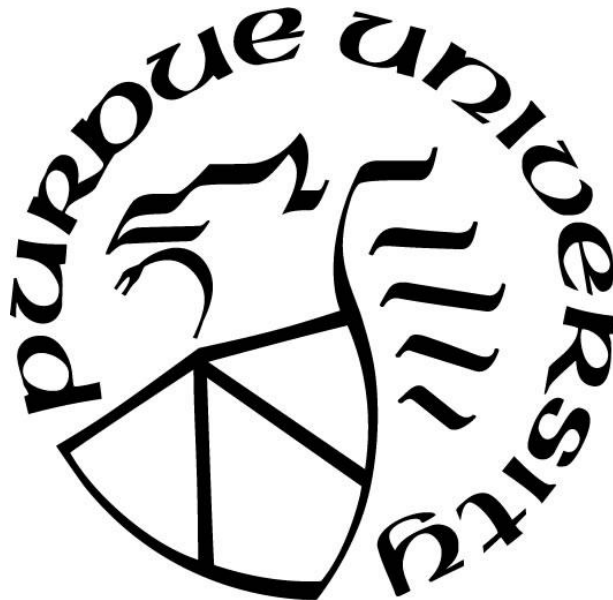
by  
**Hong Sun**

**A Dissertation**

*Submitted to the Faculty of Purdue University*

*In Partial Fulfillment of the Requirements for the degree of*

**Doctor of Philosophy**



School of Mechanical Engineering

West Lafayette, Indiana

December 2020

**THE PURDUE UNIVERSITY GRADUATE SCHOOL**  
**STATEMENT OF COMMITTEE APPROVAL**

**Prof. Kejie Zhao, Chair**

School of Mechanical Engineering

**Prof. Eric P. Kvam**

School of Materials Engineering

**Prof. Jianguo Mei**

School of Chemistry

**Prof. Peilin Liao**

School of Materials Engineering

**Approved by:**

Dr. Nicole L. Key

*Dedicated to my parents for their love, endless support and encouragement*

## ACKNOWLEDGMENTS

First and foremost, I would like to thank my advisor, Prof. Kejie Zhao, for his supervision and guidance throughout the completion of my Ph.D. study. I am deeply grateful for his patience, motivation, and insightful feedback, which help me sharpen my thinking and strengthen my research skills. This work would not have been possible without the tremendous support of Prof. Zhao.

I would also like to thank my committee members: Prof. Eric P. Kvam, Prof. Jianguo Mei, and Prof. Peilin Liao, for their valuable suggestions and comments on my thesis research, which brought my work to a higher level. I want to express my sincere appreciation to Prof. Kvam for his precious advice on my research subject - “Superelastic Organic Semiconductors”. I own my special thanks to Prof. Mei and Prof. Liao for their enormous help and support during my postdoc application. Many thanks are also extended to my collaborators, Prof. Ying Diao and Dr. Sangkyu Park, for many insightful discussions they held with me to advance my thesis research.

My sincere thanks also go to my colleagues: Luize Scalco de Vasconcelos, Nikhil Sharma, Dr. Rong Xu, etc. It has been a memorable experience befriending and working with such warm and delightful people. I cannot fully detail the thoughtful commentary and constructive conversations provided by them throughout my Ph.D. study. My special thanks are also extended to my friends for their encouragement, love, and support. Thanks for offering me the relief and distractions to help me go through the hardships during the journey. Thank you one and all.

Last but not least, I would like to express my utmost gratitude to my parents for their unconditional love and everlasting support. Sincere appreciation also goes to my brother and other family members for their understanding and encouragement. Your love and support have been indispensable to my success.

# TABLE OF CONTENTS

LIST OF TABLES .....	8
LIST OF FIGURES .....	9
ABSTRACT .....	16
CHAPTER 1. INTRODUCTION .....	17
1.1 Background and Aim .....	17
1.2 Overview of the Thesis .....	22
1.3 References .....	26
CHAPTER 2. ELECTRONIC STRUCTURE STUDY OF BATTERY MATERIALS.....	28
2.1 Electronic Structure and Comparative Properties of $\text{LiNi}_x\text{Mn}_y\text{Co}_z\text{O}_2$ Cathode Materials	28
2.1.1 Background and Motivation .....	28
2.1.2 Simulation Methods.....	29
2.1.3 Results and Discussion .....	31
2.1.3.1 Valence States and Bonding Analysis .....	32
2.1.3.2 Atomic Ordering in Super-lattice .....	35
2.1.3.3 Comparative Properties of NMC Compositions.....	37
2.2 Electron Density Analysis of Polarized Eutectic Electrolyte .....	47
2.2.1 Background.....	47
2.2.2 Simulation Methods.....	47
2.2.3 Results.....	48
2.3 References.....	51
CHAPTER 3. PHASE DYNAMICS AND ENERGY STORAGE MECHANISMS OF ELECTRODE MATERIALS .....	53
3.1 Atomistic Origins of High Capacity and High Structural Stability of Polymer-derived SiOC Anode Materials .....	53
3.1.1 Background and Motivation .....	53
3.1.2 Simulation Methods.....	54
3.1.2.1 Model Generation .....	54
3.1.2.2 Computational Methods .....	55
3.1.3 Results and Discussion .....	56

3.1.3.1	Formation Energy during Lithiation Process.....	56
3.1.3.2	Structural Evolution upon Lithiation.....	59
3.1.3.3	Electron Transfer between Lithium and Si-based Glass Ceramics .....	65
3.2	First-principles Studies on the Electrochemical and Mechanical Behaviors of $\alpha$ -MoO <sub>3</sub> in Li-ion Batteries .....	68
3.2.1	Background and Motivation .....	68
3.2.2	Simulation Methods.....	69
3.2.3	Results and Discussion .....	70
3.3	Evolution of Mechanical Properties of LiNi <sub>x</sub> Mn <sub>y</sub> Co <sub>z</sub> O <sub>2</sub> Cathode during Delithiation ....	73
3.3.1	Background.....	73
3.3.2	Simulation Methods.....	74
3.3.3	Results and Discussion .....	74
3.4	References.....	79
CHAPTER 4. THERMAL-INDUCED POLYMORPHIC TRANSITIONS IN ORGANIC SEMICONDUCTOR CRYSTALS.....		83
4.1	Introduction.....	83
4.1.1	Organic Crystals .....	83
4.1.2	Challenges in Atomistic Simulation .....	85
4.2	Simulation Methods.....	86
4.2.1	Ab-initio Modeling .....	86
4.2.2	Force Field Parameterization.....	88
4.2.3	Genetic-Algorithm Refined Molecular Dynamics.....	92
4.3	Results and Discussion .....	95
4.3.1	Structure Search.....	95
4.3.2	Molecular Rotations Dominated Polymorphic Transition.....	97
4.3.3	Thermodynamics Analysis .....	101
4.4	References.....	106
CHAPTER 5. SUPER- AND FERROELASTIC TRANSITION IN ORGANIC SEMICONDUCTOR CRYSTALS.....		108
5.1	Introduction.....	108
5.2	Simulation Methods.....	111

5.2.1	Ab-initio Molecular Dynamics .....	111
5.2.2	Molecular Dynamics.....	112
5.2.3	Structural Descriptor and Order Parameter .....	113
5.3	Results and Discussion .....	116
5.3.1	Superelasticity, Ferroelasticity and Cooperative Molecular Motions .....	116
5.3.1.1	Superelasticity .....	116
5.3.1.2	Ferroelasticity .....	118
5.3.2	Interconvertible Behavior of Superelasticity and Ferroelasticity .....	123
5.3.3	Molecular Twinning and Molecular Defects .....	126
5.3.4	Electronic Properties.....	132
5.4	References.....	136
CHAPTER 6. SUMMARY AND BROAD IMPLICATION .....		138
6.1	Summary of the Thesis .....	138
6.2	Outlook for the Future .....	140
VITA.....		142

## LIST OF TABLES

Table 2.1 Population of the short (S) and long (L) TM-O bonds in the five NMC compositions.	34
Table 2.2. Probability of TM-TM pairs in NMC333 .....	37
Table 2.3 TM and Li slab spacing and average bond length of TM-TM and TM-O pairs .....	42
Table 4.1. The atom symbol, atomic charges and atom type used in OPLS-AA force field.....	92
Table 4.2. Re-parameterized force field parameters for the bond lengths and angles associated with <i>sp</i> carbon atom and silicon atom in TIPS-P molecule. ....	92
Table 4.3. Re-parameterized force field parameters for the dihedral angles associated with <i>sp</i> carbon atom and silicon atom in TIPS-P molecule.....	92
Table 4.4. Coulombic partial charges for TIPS-pentacene molecules.....	94
Table 4.5. Van der Waals parameters for TIPS-pentacene molecules.....	95
Table 4.6. The six lattice parameters ( $a$ , $b$ , $c$ , $\alpha$ , $\beta$ , $\gamma$ ) of optimized polymorphs obtained from the structural searching algorithms agree well with the experimental data. The percentage differences between simulation and experimental data are shown in the parentheses. ....	97
Table 4.7. The simulated lattice parameters (red) agree well with the experimental data (blue). Their percentage differences are shown in the parentheses.....	100
Table 5.1. The six lattice parameters of three polymorphs in the shear stress-induced SE-I (left panel) and SE-II (right panel) agree well with the experimental data. The percentage differences between simulation and experimental data are shown in the parentheses. ....	112

## LIST OF FIGURES

Figure 2.1. Ionic radius and 3 <i>d</i> electron population of the six transition metal ions.....	32
Figure 2.2. TM-O octahedral complexes in NMC. (a) Ni, Mn, and Co reside at the octahedral site surrounded by six O atoms. (b) Local view of the TM-O octahedral complexes. Ni <sup>3+</sup> and Co <sup>2+</sup> are active Jahn-Teller ions. Ni <sup>2+</sup> , Co <sup>3+</sup> , and Mn <sup>4+</sup> are inactive Jahn-Teller species. The degree of distortion of the octahedra indicates the ionic states of the TM elements. The grey, blue, and purple spheres represent Ni, Co and Mn atoms in the TM layer, respectively, and the red sphere represents O atoms.....	33
Figure 2.3. The occupation fraction of Ni <sup>2+</sup> /Ni <sup>3+</sup> and Co <sup>2+</sup> /Co <sup>3+</sup> in the five NMC compositions.....	35
Figure 2.4. (a) NMC lattice with the <i>R3m</i> space group. (b) Population map of the 81 configurations for each NMC. Different configurations are made of different arrangements of Ni/Mn/Co in the TM layer. 81 configurations are constructed for each NMC composition and are categorized in five groups according to the difference of free energy per atom relative to the lowest energy state. Atomic arrangement from (c) the top-view and (d) the <i>a</i> -axis view of the TM layer in a NMC supercell consisting of 36 energetically favorable configurations. The dashed lines mark the possible cluster units. Multiple clusters with random population indicate the absence of long-range atomic ordering.....	36
Figure 2.5. Molecular orbital diagram of the transition metal complex showing the <i>d</i> orbital electron population of Co <sup>3+</sup> and O 2 <i>p</i> orbital.....	38
Figure 2.6. Total and partial density of states of (a) NMC333, (b) NMC442, (c) NMC532, (d) NMC622, and (e) NMC811, respectively. The dashed lines represent the total density of states. The blue, red, and green lines represent the partial density of states of the TM 3 <i>d</i> orbital, O 2 <i>p</i> orbital, and Li <i>s</i> orbital, respectively. Fermi energy is shifted to zero. Energy level below -4 eV shows large overlaps between O 2 <i>p</i> and TM 3 <i>d</i> orbitals due to the strong covalent interactions. The <i>t2g</i> population for the TM 3 <i>d</i> orbital dictates the energy range of -2 to 0 eV. The higher energy region above the Fermi level represents the anti-bonding states between the <i>eg</i> * population in the TM 3 <i>d</i> orbital and partial O 2 <i>p</i> orbital. The band gap gradually closes and the Fermi energy shifts to larger values from NMC333 to NMC811 due to the increasing portion of Ni.....	39
Figure 2.7. Crystal orbital overlap population analyses of the TM-O pairs. A positive value represents the bonding state, whereas a negative value shows the anti-bonding state. The broad bonding regime (-9 ~ -4 eV) corresponds to the strong covalent states between TMs and O. Near the Fermi energy, the <i>t2g</i> level contributes to the anti-bonding states and nearly no bonding at the Fermi level. Above the Fermi energy, negative COOP indicates the repulsion of TMs and O because of the interactions of the <i>eg</i> * level and O 2 <i>p</i> orbital.....	40
Figure 2.8. Lattice constants in (a) the <i>a</i> -axis and (b) the <i>c</i> -axis directions of the five NMC compositions. The average (symbols) and standard deviation (error bars) are calculated from the 81 configurations in each NMC composition. (c) Variation of the (001) plane spacing in different NMC compositions. The theoretical predictions (green line) show the same trend compared with the XRD measurement (black line).....	41

Figure 2.9. Young's modulus of the five NMC compositions calculated from the supercell model (VASP) and the virtual crystal approximation model (CASTEP and ABINIT) in comparison with the experimental values..... 43

Figure 2.10. (a-e) Phonon dispersion and phonon density of states of NMC333, NMC442, NMC532, NMC622, and NMC811, respectively. In the phonon dispersion curves, the three lowest branches represent the acoustic mode and other thirty three branches represent the optical mode. In the DOS curves, the high- and medium-frequency regimes are contributed by Li and O, while the low-frequency regime is mainly contributed by TMs. From (a) to (e), the two peaks in the low-frequency regime sharpen and slightly shift toward higher values, indicating the increase of the TM-O bonding strength. (f) Longitude acoustic frequency in the five NMC compounds around the Gamma point. The acoustic frequency increases from NMC333 to NMC811 due to the weaker electron screening effect..... 45

Figure 2.11. Thermal properties of NMC including the Helmholtz free energy  $F$ , the vibrational entropy  $S$ , and the constant-volume specific heat capacity  $C_v$ ..... 46

Figure 2.12. Thermal stability (experimental values, blue triangles) and cohesive energies (theoretical results, red rectangles) of the five NMC compositions. Thermal stability gradually degrades in the Ni-rich compounds. .... 46

Figure 2.13. Optimized structures and charge distributions for choline-like chloride, urea and local DES cluster..... 48

Figure 2.14. Calculated interaction energy for two types of hydrogen bonds in DES cluster..... 49

Figure 2.15. Extended cluster model(contains 208 atoms) after AIMD optimization and charge density analysis over circled area. .... 50

Figure 3.1. The atomic model of silicon oxycarbide (SiOC) consisting of the C phase,  $\text{SiO}_x\text{C}_{4-x}$  units, and nano-voids. (a) An overview of the supercell with an applied periodic boundary condition. (b) The unit cell shows a series of vertex-sharing tetrahedra including  $\text{SiO}_4$ ,  $\text{SiO}_3\text{C}$ ,  $\text{SiO}_2\text{C}_2$ , and  $\text{SiOC}_3$ . The gray atoms represent the segregated C phase which forms the backbone of the network. Excess C atoms are randomly distributed and topological defects of five and seven C-C rings exist. The blue dotted circles mark the nano-voids percolated in the lattice which contribute to the low density of SiOC molecule..... 57

Figure 3.2. Two-step lithiation of SiOC shown in (a) the formation energy per Li in  $\text{Li}_x\text{SiOC}$  and (b) the volumetric strain as a function of Li concentration. The solid lines represent the average values of the formation energy per Li or the volumetric strain from the five configurations at a given Li concentration, and the error bars represent the standard deviation. The red lines indicate Li intercalation at the nano-voids. The formation energy per Li in this stage shows a large variation at a given Li concentration because of the large difference in the local bonding environment. The lattice volume decreases due to the structural relaxation mediated by Li insertion. The blue lines delineate Li reactions with the SiOC tetrahedron units and the C phase. Both the formation energy and volumetric strain reach a steady slop as Li inserts in stage II..... 59

Figure 3.3. The structural feature of lithiated SiOC represented by (a) the coordination number of Si-O, C-C, and Si-C, (b) the coordination number of O-Li and C-Li, (c) the number of  $\text{SiO}_x\text{C}_{4-x}$  tetrahedral units, and (d) the radial distribution function (RDF) of Si-O and C-C before and after

lithiation. The coordination number in (a) corroborates the two-step lithiation that little change of chemical bonding is involved when Li composition is below  $\text{Li}_{42}\text{Si}_{28}\text{O}_{42}\text{C}_{68}$ , while further lithiation is associated with the breaking of Si-O bonds. The increasing coordination number of O-Li and C-Li in (b) indicates that Li are attracted by the O and C atoms. The statistics of  $\text{SiO}_x\text{C}_{4-x}$  tetrahedral units in (c) shows that the number of the interior units caged in the network steadily decreases, while the units residing in the vicinity of the segregated C phase remain nearly unperturbed upon lithiation. The RDF of Si-O and C-C in (d) again shows the local stable bonding of C-C and severe breaking of Si-O when Li inserts. .... 60

Figure 3.4. (a) The evolution of atomic configurations of SiOC during lithiation. The backbone of segregated C phase stabilizes the structure. The cell volume changes up to 22% after full lithiation. (b) Local structural rearrangement in the atomic configurations in (a) includes stretching and breaking of Si-O bonds, geometry perturbation of Si-C-C-Si clusters, and bond switching in C rings. The purple, red, gray, and green spheres represent the Si, O, C, and Li atoms, respectively. .... 62

Figure 3.5. The bond angle distribution of C-C-C, Si-C-C, and Si-C-Si clusters in five representative  $\text{Li}_x\text{SiOC}$  compositions. The salient features are that the probability of bond angles larger than  $145^\circ$  steadily decreases while the distribution of bond angles between  $115^\circ$  and  $130^\circ$  increases significantly upon lithiation. This demonstrates the geometry optimization of C atoms toward the  $sp^2$  type coordinated by Li insertion. .... 63

Figure 3.6. The evolution of two molecular orbitals contributed by two centered C atoms in a Si-C-C-Si cluster. (a) Before lithiation, the  $p_y$  orbitals of the two C atoms overlap to form one  $\pi$  type molecular orbital,  $\pi_y$ . (b) Similarly, two  $p_z$  atomic orbitals overlap to form the  $\pi_z$  orbital. (c) After lithiation, the original  $\pi_y$  orbital is perturbed by the virtual orbital of the nearby Li atoms (not shown in the diagram) and is split into two atomic orbitals in different orientations, which promotes the formation of the hybrid  $sp^2$  orbital. (d) In comparison, there is no obvious difference in  $\pi_z$  which remains perpendicular to the  $sp^2$ -hybrid planar orbital before and after lithiation. .... 65

Figure 3.7. The map of charge density difference in different regions of  $\text{Li}_{66}\text{Si}_{28}\text{O}_{42}\text{C}_{68}$ . From left to right, it shows the charge density difference of the segregated C interface, the Si-O-C mixed regime, and the amorphous silica domain before and after Li insertion, respectively. In the graphene-like C phase, charge transfer takes place at the imperfection sites such as the five or seven C rings or the edge of C atoms. The saturated  $sp^2$  C atoms remain inactive and serve as the stable backbone to maintain the structure. In the mixed Si-O-C regime, charge transfer mainly occurs around the O atoms and unsaturated C atoms. For the  $\text{SiO}_4$  tetrahedral units in the silica domain, positive charge is accumulated around the O atoms. .... 66

Figure 3.8. The density of states (DOS) of (a) pristine SiOC, (b)  $\text{Li}_2\text{Si}_{28}\text{O}_{42}\text{C}_{68}$ , (c)  $\text{Li}_4\text{Si}_{28}\text{O}_{42}\text{C}_{68}$ , and (d)  $\text{Li}_6\text{Si}_{28}\text{O}_{42}\text{C}_{68}$ , respectively. The DOS of pristine SiOC has an insulator character with a band gap of 1.3 eV. During initial lithiation, the electron transfer from Li to O and defective C atoms induces electron states near the Fermi level. The band gap is significantly reduced by the insertion of four Li atoms. Up to six Li, the band gap vanishes which indicates that the electronic conductivity of SiOC molecule can be enhanced by the dopant Li. .... 67

Figure 3.9. First-principles modeling on the two-step lithiation of  $\alpha\text{-MoO}_3$ . (a) The interlayer and intralayer sites are the two favorable interstitial positions for Li intercalation in  $\alpha\text{-MoO}_3$ . (b, c) Li

occupies the favorable interstitial sites which induces the formation of crystalline  $\text{Li}_2\text{MoO}_3$ . (d, e) The conversion reaction causes solid-state amorphization of the structure. (f) RDF plot of the Mo-Mo pairs in  $\text{MoO}_3$ ,  $\text{Li}_2\text{MoO}_3$  and  $\text{Li}_6\text{MoO}_3$ . The compositions in (b)-(e) are  $\text{Li}_{1.5}\text{MoO}_3$ ,  $\text{Li}_2\text{MoO}_3$ ,  $\text{Li}_{3.75}\text{MoO}_3$ , and  $\text{Li}_6\text{MoO}_3$ , respectively. The atomic configurations are expanded views consisting of  $3 \times 1 \times 3$  unit cells. The blue, red, and green spheres represent Mo, O, and Li atoms. .... 70

Figure 3.10. Diffusion barrier of a single Li from the interlayer to the intralayer site calculated by the nudged elastic band (NEB) method. .... 72

Figure 3.11. The two-step lithiation of  $\text{MoO}_3$  evident in (a) the formation energy per Li in  $\text{Li}_x\text{MoO}_3$  and (b) strains in the in-plan ( $\epsilon_x$ ) direction, out-of-plan ( $\epsilon_y$ ) direction, and the total volumetric strain ( $\epsilon_v$ ). The solid symbols represent the average values of the formation energy per Li or strains from five different configurations of  $\text{Li}_x\text{MoO}_3$ , and error bars represents the standard deviation. .... 73

Figure 3.12. First-principles results on (a) the Young's modulus and cohesive energies, (b) the Bader charge of O and transition metal ions, and (c) the map of electron density difference in NMC at different states of charge. .... 75

Figure 3.13. The Ni-O bond length distribution in NMC at different states of charge. During delithiation, the Ni-O bond length decreases implying the transition from  $\text{Ni}^{2+}$  into  $\text{Ni}^{3+}$ . .... 76

Figure 3.14. The gradual increase of Bader charge of Ni during delithiation. .... 77

Figure 3.15. The gradual increase of Li-O bond length and *c*-axis lattice parameter during delithiation of NMC. .... 78

Figure 3.16. Molecular orbital diagram of the transition metal complex showing the *d* orbital electron population of  $\text{Co}^{3+}$  and O *2p* orbital. .... 78

Figure 4.1. Molecular lattices of TIPS-pentacene polymorphs Form I, II, and III. .... 85

Figure 4.2. Structural search during heating and mechanical load in ab initio molecular modeling ..... 88

Figure 4.3. The atom symbol of OPLS-AA force field assigned to each atom in TIPS-P molecule. **CA** and **HA** are for carbon atom and hydrogen atom of pentacene backbone, respectively. **CT<sup>I</sup>** and **HC<sup>I</sup>** are for carbon atom and hydrogen atom of the methyl group in the TIPS unit, respectively. **CT<sup>II</sup>** is for carbon atom connecting Si atom and two methyl groups in the TIPS unit. **HC<sup>II</sup>** is for hydrogen atom bounded to **CT<sup>II</sup>** atom. **CZ<sup>I</sup>** and **CZ<sup>II</sup>** are for the *sp* carbon atoms. .. 90

Figure 4.4. The comparison between DFT single point energies (blue dots) and the fitted curve (red lines) using the OPLS force field equations for the specific bond length, angle and dihedral angles. .... 91

Figure 4.5. **a** The temperature fluctuations and **b** the average pressure fluctuations of the  $24 \times 48 \times 1$  supercell model of Form I for the equilibrium 5 ps after running the MD simulation under NPT ensemble at 27°C and zero pressure for 200 ps. .... 91

Figure 4.6. (A) Flowchart of parametric training for coulombic and Van der Waals parameters. (B) The workflow of the Genetic-Algorithm training module. .... 94

Figure 4.7. Preliminary modeling results of phase transition (Form I – Form II) in TIPS-pentacene induced by heating and mechanical load. The transition is reversible, with a energy barrier of 43 meV.....	96
Figure 4.8. (A) A unit cell of the TIPS-pentacene molecular crystal. (B) The experimental (blue squares) and simulation (red circles) results of the change in the <i>b</i> -lattice parameter during heating. (C) Molecular crystal structures of Form I (blue) and Form II (red) show the angular rotation $\theta$ of the molecular orientation in the <i>ab</i> plane. (D) Contour map of the order parameter of 14 molecules when temperature increases. The average order parameter demonstrates the 2 <sup>nd</sup> order and 1 <sup>st</sup> order phase transitions upon heating. (E) Phonon density of states show the phonon softening when the structure morphs from Form I (green curve) to Form II (red curve).....	98
Figure 4.9. Molecular trajectories of Form I-to-II transition upon heating. ....	100
Figure 4.10. Energy barrier of Form I – II phase transition determined by AIMD and NEB calculations (a), and measured by differential scanning calorimetry experiments (b). ....	102
Figure 4.11. Raman spectrum for different polymorphs under their equilibrium temperatures. ....	105
Figure 5.1. A sketch of the phase diagram of the TIPS-pentacene semiconductor crystal in the space of temperature-stress-strain exhibiting thermoelasticity (TE), superelasticity (SE), and ferroelasticity (FE).....	111
Figure 5.2. The resolved shear stress and shear strain at (210) plane in FE-II are calculated based on the above equations (left). Here the value of $\theta = 19^\circ$ is deduced from the analysis of geometric relations (right), where $\theta = 90^\circ - (180^\circ - 80^\circ - 29^\circ)$ . The lattice angle $\gamma$ is $80^\circ$ for Form I and the angle between the <i>b</i> axis and (210) plane (along backbone direction) is $29^\circ$ . The stress and strain components $\sigma_x$ , $\sigma_y$ , $\tau_{xy}$ , $\epsilon_{xx}$ , $\epsilon_{yy}$ , $\epsilon_{xy}$ , are all obtained from MD simulation of FE-II.....	113
Figure 5.3. <b>a</b> The point molecule scheme of TIPS-P. <b>b</b> The center-of-mass distances between the center molecule and its four nearest neighbor molecules used to define the structural descriptor. ....	115
Figure 5.4. The value of structural descriptor $\rho$ of each molecule in the $24 \times 24 \times 1$ superlattice of three polymorphs at the equilibrium states of MD simulation in the canonical NVT ensemble at $27^\circ\text{C}$ . Each solid line represents the mean value of all calculated structural descriptors (black dots) with the standard deviation shown in the shaded area for each polymorph. ....	115
Figure 5.5. (a) AIMD modeling of superelastic transition induced by temperature or shear strain. (b) molecular motions of superelastic transition at 400K.....	117
Figure 5.6. (a) The rotational angle of the backbone when the polymorphs evolve from Form I to Form II, and then to Form III. (b) The experimental determination of the relative orientation between the polymorphs. ....	118
Figure 5.7. The DFT calculated strain-stress curves for <b>a</b> SE-I and <b>b</b> SE-II transitions by the static shear loading.....	118

Figure 5.8. (a) six representative simulation snapshots of FE-I. The corresponding stress-strain curve is plotted in (b). (c) depicts the twinning interface. (d) Experimental observation of FE-I before and after the transition. ....	120
Figure 5.9. (a) six representative simulation snapshots of FE-II. The corresponding stress-strain curve is plotted in (b). (c) depicts the twinning interface. (d) Experimental observation of FE-II before and after the transition. ....	121
Figure 5.10. (a) The evolution of rotational angles of four molecules in a (0 1 0) layer in FE-I. (b) the evolution of displacement of four molecules in a (2 1 0) layer in FE-II.....	122
Figure 5.11. Time-dependent order parameter evolution of three adjacent molecular layers, upon FE-I transformation. Characteristic times $t_1 - t_5$ are indicated by the dotted line. The plot clarifies layer-by-layer molecular cooperativity by showing a well-established transformation sequence, as summarized in the table below. ....	123
Figure 5.12. (A) The molecular trajectories of the interconvertible SE and FE of Form II by $\langle 1\ 0\ 0 \rangle$ shear at 400 K. Their corresponding stress-strain responses are shown in (B). The molecules in (A) are color-coded by the order parameter representing the different phases as marked in the color bars.....	124
Figure 5.13. (A) Sketch of the lattice transformation of ferroelasticity and superelasticity in Form II. The cells of different colors represent different polymorphs of distinct molecular orientations. (B) Contour plot of the molecular rotation of 10 molecules in Form II under $\langle 1\ 0\ 0 \rangle$ shear load. The black arrows are the vectors representing the direction of the molecular orientation. (C) The molecular potential energy as a function of the shear strain when Form II is deformed by shear. The insets show the deformation twinning associated with FE (left) and lattice transition from Form II to Form I associated with SE (right).....	125
Figure 5.14. (A) The molecular trajectories of FE-I and FE-II of Form I by $1\ 0\ 0$ shear and $0\ 1\ 0$ tension at 300K, respectively. Their corresponding stress-strain responses are shown in (B). The molecules in (A) are color-coded by the order parameter representing the different phases as marked in the color bars.....	127
Figure 5.15. (A) Illustration of the twinning elements of FE-I in Form II. (B) Snapshots of the molecular structure showing the metastable phase (red) and the twinned phase (blue). The twinning angles in the modeling match well with the experimental observation (optical image). (C) Correlation between the molecular rotational angle (red) and the angle ( $2\alpha$ ) between the conjugated twinning planes (blue). The dotted curves denote the mean values for five different cells in the modeling and the shaded areas represent the standard deviations. (D) The two-step twinning formation achieved by molecular disclination dipoles. ....	128
Figure 5.16. (A) The twinning elements of FE-II in Form II. (B) Snapshots of the molecular structure upon mechanical load showing the metastable phase (red) and the twinned phase (blue). The optical image shows the crystallography of twinning and a surface crack in experiments. (C) The two-step formation mechanism of twinning by the stacking faults. (D) Snapshots (upper panel) demonstrate the ejection of a molecular dislocation accompanying the twinning process. Lower panel shows the magnified view of vacancy formation and dislocation climb in the $2\ 1\ 0$ layers.....	130

Figure 5.17. (a) HOMO and LUMO orbitals of Form I. (b) The values of HOMO, LUMO, and band gap for Form I and Form II. .... 133

Figure 5.18. The charge integral map for ten molecules across the twinning zone in FE-II transition. .... 135

## ABSTRACT

Global demand for high performance, low cost, and eco-friendly electronics is ever increasing. Ion/charge transport ability and mechanical adaptability constitute two critical performance metrics of battery and semiconductor materials, which are fundamentally correlated with their structural dynamics under various operating conditions. It is imperative to reach the mechanistic understanding of the structure-property relationships of electronic materials to develop principles of materials design. Nevertheless, the intricate atomic structure and elusive phase behaviors in the operation of devices challenge direct experimental observations. Herein, we employ a spectrum of modeling methods, including quantum chemistry, ab-initio modeling, and molecular dynamics simulation, to systematically study the phase dynamics and physico-mechanical behaviors of multiple electronic materials, ranging from transition-metal cathodes, polymer derived ceramics anodes, to organic semiconductor crystals. The multiscale atomistic modeling enriches the fundamental understanding of the electro-chemo-mechanical behaviors of battery materials, which provides insight on designing state-of-the-art energy materials with high capacity and high structural stability. By leveraging the genetic-algorithm refined molecular modeling and phase transformation theory, we unveil the molecular mechanisms of thermo-, super- and ferroelastic transition in organic semiconductor crystals, thus promoting new avenues of adaptive organic electronics by molecular design. Furthermore, the proposed computational methodologies and theoretical frameworks throughout the thesis can find use in exploring the phase dynamics in a variety of environmentally responsive electronics.

# CHAPTER 1. INTRODUCTION

## 1.1 Background and Aim

Electronics encompass our modern lives daily. Functional materials with the ability of energy conversion and/or charge transfer play the key roles in electronics, which evolve fast to meet the growing demand for modern technologies. One of the milestone achievements in the electronics field is the invention of rechargeable battery in 1859, which opened the door for the application of portable devices. Batteries convert chemical energy to electricity, wherein the electrons shuttle between the anode and the cathode accompanying the ions transporting through the electrolyte. In the past several decades, we have witnessed the great advancement in battery technology, which is manifested by the emergence of new electrode materials from lead dioxide, nickel-cadmium to lithium transition metal oxides. Nowadays, Li-ion batteries are state-of-the-art choices for powering portable electronics and electric vehicles, fueled by their advantages of high energy density and excellent cyclability<sup>1</sup>. A myriad of electrode formulations have been extensively explored in recent years. The typical anode materials include metallic lithium<sup>2</sup>, graphite<sup>3</sup>, and silicon-based materials<sup>4</sup>. The common choices of cathode materials are lithium manganese oxide<sup>5</sup>, lithium cobalt oxide<sup>6</sup>, FeS<sub>2</sub><sup>7</sup>, lithium nickel cobalt manganese oxide (NMC)<sup>8</sup>, etc. Although those electrode materials exhibit remarkable electric performance in operation, their development is still far behind in meeting the mounting demand for rapid (dis)charging rate, high energy consumption, and eco-sustainability. To this end, enormous efforts from the research community and industry have been devoted to developing next-generation battery technology to enable much larger-scale energy storage and other wide range applications. Another emerging field in the realm of electronics is the semiconductor devices, which usually serve as the information processing component widely used in laptops and cellphones. To date, silicon is the most widely used semiconductor material thanks to its low cost, easy processing, and thermal stability. In recent decades, other semiconducting materials such as two-dimensional metal dichalcogenides<sup>9,10</sup>, zinc oxide<sup>11</sup>, perovskites<sup>12</sup>, and organic conjugated molecules<sup>13,14</sup> are actively pursued as they present the advantage of solution processing, which substantially simplifies the device fabrication. Among them, organic semiconductor materials warrant particular attention from researchers owing to their advantage of versatility in chemical synthesis

and compatibility with flexible substrates with a process temperature  $< 100$  °C. Besides, they usually comprise toxic-free and environmentally benign elements such as carbon and hydrogen, which attracts vast interest in the application of wearable electronics and biocompatible devices.

Ion/Charge transporting constitutes the fundamental physics of battery and semiconductor materials. For Li-ion batteries, the major figure of merit in terms of physical performance is the high energy/power density, which is primarily determined by the ability of ion storage and diffusion in the host electrode materials. The energy capacities of common lithium metal oxides cathodes range from 100 Ah/kg to 300 Ah/kg. Their ion storage mechanisms are generally divided into two types: insertion and conversion. For the insertion type metal oxides, such as  $\text{CoO}_2$  and  $\text{V}_2\text{O}_5$ , the lithium atoms populate in the two-dimensional Van der Waals layers or reside at the octahedron/tetrahedron interstitial sites in the crystalline structures<sup>15-18</sup>. The available vacant sites set the limit of Li-ion storage capacity of insertion-type oxides cathode. In the conversion-type metal oxides, such as  $\text{Co}_3\text{O}_4$  and  $\text{NiO}$ , the intercalation of lithium ions distorts the original crystalline structure and transforms the metal oxides into the elemental metal and lithium oxides<sup>18,19</sup>. The amorphization of conversion-type metal oxides promises a higher capacity than the insertion-type cathodes. One of the most commonly used anode materials is graphite owing to its stable cyclability and high coulombic efficiency<sup>20</sup>. But the low reversible capacity of  $\sim 300$  Ah/kg limits its application in high-energy-density batteries. A variety of silicon-based composites are currently being explored to replace the conventional graphite anodes<sup>21</sup>. 1 Si atom can alloy with 3.75 Li atoms, while 6 C atoms can only host 1 Li, which results in the specific capacity of Si 10 times higher than that of graphite. For either cathode or anode materials, their energy storage capacity is dictated by the structural dynamics during the (de)lithiation process. Likewise, the molecular packing structure plays a crucial role in determining the charge transport physics in organic semiconductors. Recent years have witnessed great advancement in improving the charge transfer mobility of organic semiconductors by the means of molecular design. The first organic semiconductor-based field-effect transistors invented in the late 1980s demonstrated the very low charge mobility values of  $10^{-6}\sim 10^{-5}$   $\text{cm}^2\text{V}^{-1}\text{s}^{-1}$ . Later, many conjugated polymers and small molecules emerge with the charge mobility exceeding  $1$   $\text{cm}^2\text{V}^{-1}\text{s}^{-1}$ , which is on par with the mobility of conventional amorphous silicon semiconductors. Nowadays, the best performing small molecular semiconductors such as BTBT<sup>22</sup> and DBTTT<sup>23</sup> can reach the charge carrier mobility on the order

of  $10 \text{ cm}^2\text{V}^{-1}\text{s}^{-1}$  in their crystalline form. The donor-acceptor (D-A) copolymers such as DPP-BTz<sup>24</sup> and CDT-BTz<sup>25</sup> demonstrate the reliable charge mobility of  $7\sim 10 \text{ cm}^2\text{V}^{-1}\text{s}^{-1}$ . Compared to the intricate entanglement of chains in polymer materials, small-molecule semiconductors, especially in its crystalline form, exhibit well-determined molecular structures, which can be utilized as the perfect physical platform to study the relationships of molecular packing and charge transport property. Typically, there are four different types of packing structures in molecular semiconductor crystals: slipped stack, slipped pi-stack, brick wall, and herringbone pack. Fundamentally, the charge transport ability of organic semiconductor molecules is dominated by the overlap of two neighboring orbitals, i.e., highest occupied molecular orbital (HOMO) and lowest unoccupied molecular orbital (LUMO). The feasible transport pathways are usually determined by the closed molecular packing direction, wherein the orbital overlap of two neighbor molecules is deemed uttermost. Slipped-stack or slipped pi-stack molecules usually present a strong anisotropic transport property, wherein the charge carriers are mostly favored in one specific packing direction. While the herringbone molecular packing guarantees isotropic transport properties as the charge transfer is almost equally fast in three directions<sup>26,27</sup>. The brick-wall packing with two favorable charge transfer paths falls in an intermediate regime. Generally, the molecular systems with isotropic charge transfer exhibit higher charge carrier mobilities<sup>28,29</sup>, excepting for the slipped  $\pi$ -stacked rubrene molecule possesses the highest reproducible charge mobility ( $> 15 \text{ cm}^2\text{V}^{-1}\text{s}^{-1}$ ) to date.

Another important performance metric for both Li-ion battery and organic semiconductors is the mechanical property. For most Li-ion electrode materials, energy storage capacity and mechanical stability are mutually exclusive properties: A gain in capacity is often associated with the large volumetric change and sacrifice of the structural stability of the host material upon lithiation. For example, the silicon material undergoes the drastic volumetric change (up to 400%) associated with Li insertion and extraction, which causes tremendous mechanical issues in the practical implementation of silicon-based anodes<sup>30,31</sup>. Mechanical stability is also a key factor plaguing the cyclic performance of NMC materials. Several reports have demonstrated that the NMC cathode material, albeit of only  $\sim 5\%$  volumetric change upon lithiation, suffers from heavy structural disintegration and mechanical failure after several cycles which significantly increase the ionic and electric impedance of batteries<sup>31-34</sup>. Hence, it's imperative to mitigate the potential mechanical failure of high-capacity electrodes to pursue high-performance Li-ion

batteries. Compared to the Li-ion batteries, organic semiconductor devices demand even more stringent mechanical properties since they are anticipated to be easy-processable and flexible. Polymer semiconductor materials usually present robust mechanical flexibility. Some experiments have shown that conjugated polymers such as high molecular weight P3HT thin film can sustain a remarkable extendibility of nearly 300%<sup>35</sup>. The external stress is mitigated by the rapid rearrangements of the polymer chain networks by bond breaking and reformation. After cycles, the polymeric structure will disintegrate and cause device failures. Besides, the batch-to-batch variation in the synthesis of polymer semiconductor films also challenges the control of their structural stability. Such synthesis issues are absent in the small-molecule semiconductor thanks to their well-determined structure. But in terms of mechanical flexibility, small-molecular semiconductors lag far behind the conjugated polymer system. For most conjugated molecular semiconductors, high crystallinity is desired to achieve high charge transfer mobility as it offers well-connected channels for charge carrier hopping. However, the high molecular ordering impedes the mechanical flexibility of molecular semiconductors. Single crystals of small-molecule semiconductors are brittle and usually crack within 2% strain due to their weak intermolecular interactions (e.g., Van der Waals forces and hydrogen bonding). Thus, incorporating mechanical flexibility into highly ordered molecular semiconductors is desired to promote organic electronics with ultra-flexibility and high charge mobility.

To improve the physical and mechanical performance of electronic materials, materials scientists and chemists have proposed a variety of strategies. For example, to mitigate the mechanical failure of high-capacity silicon-based anodes, a ceramics compound with hybrid Si-C atomic bonds was designed<sup>36</sup>, which can combine the strength of C (superior structural stability in lithiation cycles) and Si (high capacity) to overcome the tradeoff between capacity and mechanical stability. Such silicon-based glass ceramics react with Li at a potential ranging from 0 to 2.5 V (v/s Li/Li+) and deliver a charge capacity of ~ 600 mAh/g with robust mechanical stability over a thousand cycles<sup>37</sup>. Moreover, these ceramics can be conveniently molded into any desired shape, size, structure, or morphology as demanded by the application, and the final properties of the ceramics can be tailored by the type of the polymeric precursor and processing conditions<sup>38-41</sup>. To achieve high flexibility in molecular semiconductors, the concepts of superelasticity are borrowed from the shape memory metallurgy field and devised into organic semiconductor crystals. Recently, with the concerted experiments and simulation efforts, we

unveiled super- and ferroelasticity in TIPS-pentacene crystal which can tolerate a tensile strain of over 13 % while maintaining the high charge carrier mobility<sup>42</sup>. This finding provides a pathway to achieve the ultra-flexible high-performance single-crystal organic electronics. In the above two cases, a profound mechanistic understanding of structure-property relationships is vital to guide the design of materials with high physico-mechanical performance. Nevertheless, most of the novel electronic materials possess unconventional atomic/molecular structures, which challenge the existing experimental characterization techniques such as X-ray diffraction. Besides, the intricate dynamics of the atomic structures during the operation of devices usually evades a direct experimental observation as such events occur in an extremely short time scale (usually within seconds). For instance, the polymer derived SiOC anode material owns a hybrid atomic structure which compromises the segregated graphene network and SiO<sub>4</sub> polyhedrons, whose lattice information is ambiguous and hard to be characterized by experiments. Besides, the injection of lithium atoms into the ceramic matrix will cause instantaneous changes in its electronic structure, chemistry states, and physical properties. It's a grand challenge to capture such subtle structural responses in the course of lithiation. To this end, an atomistic simulation approach is desired to scrutinize the phase dynamics and its relations with the physico-mechanical properties of electronic materials.

Powered by the high-performance computing resources, computational modeling can conduct “virtual” experiments under ultra-fine time steps (fs/ps) and well-controlled simulation conditions (e.g. heat, stress, current). The atomistic simulation can inform the “real” experiments and significantly reduce the cost of massive trials and errors. However, there are still formidable challenges in the simulation due to its general limitations of size and time scale. Atomistic simulation mainly refers to ab initio atomic modeling and molecular dynamics simulation. Ab-initio modeling is famous for its transferable pseudopotential and accurate descriptions of electronic structure, while it suffers from the expensive computing cost for a simulation size exceeding 200 atoms. Empirical molecular dynamics simulation works efficiently for relatively large length scales (Å~μm) and time scales (fs ~ ns) but the adopted empirical atomic potential makes the simulation accuracy doubtful. Balancing these two seemingly exclusive aspects in atomistic simulation, i.e. confidence of accuracy and simulation scale, incurs great challenges to examine the structure-property relationships of electronic materials. For instance, semiconducting molecules comprise conjugated carbon backbones to enable efficient charge

transfer, which requires much larger simulation sizes compared to the atomic compound like silicon. Thus, it's computationally unfavorable to conduct ab-initio atomistic modeling for such complicated molecular systems. While the lack of accurate force fields for conjugated molecules also makes it hard to investigate its phase dynamics by molecular dynamic simulation on a larger scale. To mitigate such a challenge, the revolutionary genetic algorithm is adopted in this work to refine the empirical force field which enables the successful simulation of phase transition of molecular semiconductor materials at the molecular level. In this thesis, a spectrum of simulation methods ranging from quantum mechanics, density functional theory to molecular dynamics simulation are employed to systematically study the structure-property relations of several electronic materials from the level of electronic structure to the phase dynamics. We primarily focus on investigating the energy storage mechanisms of lithium electrode materials based on the structural dynamics during ion transport, and understanding the environmental adaptability of organic semiconducting materials achieved by the polymorphic transitions under the thermo-mechanical loads.

## 1.2 Overview of the Thesis

This thesis is organized as described below:

Chapter 1 outlines the background and the aim of the thesis work. Chapters 2&3 discuss the electronic structure, phase dynamics, and energy storage mechanisms of battery materials. Chapters 4&5 focus on the thermal-mechanically induced thermo-, super- and ferroelasticity in molecular semiconductor crystals. The contents of the four chapters are described in three subsections: background and motivation, simulation methods, and results and discussion. The summary of the thesis and its broad implications are provided in Chapter 6.

In chapter 2, we investigate the electronic structure of two battery materials based on first-principle simulation and quantum chemistry calculations. In Section 2.1, we study the electronic structure and valence states in  $\text{LiNi}_x\text{Mn}_y\text{Co}_z\text{O}_2$  (NMC) materials and compare the resulting electronic, structural, mechanical, and thermal properties of a class of NMC compositions. Two types of atomic models, i.e. supercell model and virtual crystalline approximation model, are constructed and compared in simulating the electronic and mechanical properties of NMC compositions. The crystal orbital overlap population (COOP) analysis and density of states analysis reveal that the Jahn-Teller distortion in the transition metal (TM) octahedral complex

determines the ionic states of the TM elements and further affects the structural stability, electrical conductivity, and thermal stability. We further show that long-range atomic ordering is absent in NMC lattice through intensive computational screening for over 80 structures built by the structural evolutionary algorithm. The first-principles modeling provides a theoretical foundation on a complete understanding of the physicochemical properties of NMC at the level of electronic structures. In Section 2.2, we theoretically predict the formation of solid-state electrolytes with a eutectic interface by properly mixing two organic molecules. The interaction energy analysis and electronic density difference population unveil that the sufficient electron transfer and formation of hydrogen bonds are responsible for decreasing the melting point of mixtures and forming the eutectic interface.

Chapter 3 discusses the energy storage mechanisms and phase evolution during the (dis)charging of three electrode materials. In Section 3.1, we investigate the atomistic origins of the unique chemo-mechanical performance of carbon-rich SiOC using the first-principles theoretical approach. The segregated C phase and the interface between the graphene-like C network and the Si-C-O units are generated by exploring over 180 possible local configurations using an evolutionary algorithm. The formation energy analysis unveils the thermodynamics origins of high capacity SiOC ceramics anode by demonstrating two-step lithiation mechanisms. We perform detailed statistical analysis on the microstructural features, including the evolution of the local bonding environment, tetrahedral units, geometry perturbation and relaxation, and electron transfer, to provide a complete understanding of the electro-chemo-mechanical behavior of the SiOC anode material. Section 3.2 presents the mechanistic understanding of energy storage mechanisms of  $\alpha$ -MoO<sub>3</sub> cathode materials. We mimic the lithiation process by incrementally increasing Li concentration with the aid of the Delaunay triangulation algorithm. The energetic and structural dynamics analyses predict two types of lithiation mechanisms (i.e. insertion and conversion) existing in  $\alpha$ -MoO<sub>3</sub> cathode. In Section 3.3, we conduct first-principle modeling to scrutinize the relationships of elastic property and structure changes of NMC materials at different states of charge. The results show the elastic modulus of NMC linearly decreases during lithiation, which qualitatively agrees with the experimental result. The underlying reason is unveiled by electron density analysis, wherein the Jahn-Teller distortion of NMC destabilizes the crystal lattice and reduces the mechanical strength during lithiation.

In Chapter 4, we firstly give an introduction to the molecular semiconductor crystals and its shortcoming in mechanical performance. The molecular investigation of phase dynamics in molecular solids presents many challenges such as intricate structural motions and ambiguous intermolecular interactions. To overcome those challenges, a variety of calculation methods and simulation tools are adopted in this work and are generally described as three parts in Section 4.2. The unit-cell evolution of three polymorphic structures of TIPS-pentacene molecules are captured by employing an automated structure searching algorithm accompanying the first-principle simulation. To simulate the interface kinetics and phase transition on a large scale, molecular dynamics simulation implemented with the empirical force field is adopted. The parameterization of the force field consists of two steps. Firstly, we use the quantum mechanics modeling to fit the intramolecular energetic parameters regarding the bond stretching, angle bending, and torsion. Next, we intensively explore the intramolecular parameters associated with Van der Waals force and electrostatic interactions using the evolutionary genetic algorithm. Upon this, we are able to model the polymorphic transition under varied temperature conditions. By leveraging the phase transformation theory, we demonstrate that three-dimensional molecular rotations dictate the lattice transformation in the thermoelastic transitions. And, the thermodynamic analysis reveals that phonon softening plays an essential role in the promotion of molecular symmetry and backbone rotations in the heating induced polymorphic transition.

We investigate the mechanically induced cooperative transitions of molecular semiconductor crystals in Chapter 5. The TIPS-pentacene semiconductor crystals exhibit outstanding mechanical flexibility through cooperative phase transitions, which is manifested by superelasticity and ferroelasticity. Section 5.1 introduces the concepts of super- and ferroelastic transition and discusses the emergence of flexible organic crystals. Simulation methods including ab-initio molecular dynamics modeling, molecular dynamics simulation, and order parameter analyses are described in Section 5.2. The quantitative agreement with molecular modeling, phase transformation theory, and experiments demonstrate that the three-dimensional molecular rotations dictate the lattice transformation in the super- and ferroelastic transitions. The interconvertible behavior of super- and ferroelastic transitions represents the distinct directional responses of the molecular crystal under a shear load. The rotational elastic recovery in the superelastic transition renders an unconventional diffusive phase boundary. The molecular twinning of ferroelasticity is achieved by homogenous shear deformation of the organic lattice

accompanying the molecular motions, which can be quantitatively evaluated by the phenomenological framework. We elucidate for the first time the molecular defects of disclination dipoles and molecular stacking faults leading to the formation of molecular twinning. Rotational disclination dipoles promise strong structural integrity as they evolve sequentially and eliminate potential packing faults, while the displacive gliding governed molecular stacking faults may cause undesired materials damage in operation.

Chapter 6 summarizes the main contributions of the thesis and discusses the broader impacts of the thesis work. The key contributions of this thesis work are three-fold. The first important contribution is that we enrich the fundamental understanding of the energy storage mechanisms of Li-ion battery materials. The second contribution is that, for the first time, we leverage the phase transformation theory and genetic-algorithm refined modeling to reveal the versatile cooperative transitions in molecular semiconductor materials. The proposed computational methodologies and theoretical frameworks, such as the lithium intercalation algorithm, genetic algorithm refined force field, and phase descriptors, make the third contribution of the thesis. In the end, we envision that the future work based on the thesis research will advance the emerging field of environmentally adaptive electronics, wherein the phase dynamics under external stimuli like heat and stress can rapidly modulate the physico-mechanical behaviors of electronic materials.

### 1.3 References

1. Scrosati, Bruno, *J. of Solid State Electrochemie.*, **2011**, *15*, 1623–1630.
2. Xu, W.; Wang, J.; Ding, F.; Chen, X.; Nasybulin, E.; Zhang, Y.; Zhang, J.G., *Energy Environ. Sci.*, **2014**, *7*, 513-537.
3. Yan, Z.; Hu, Q.; Yan, G.; Li, H.; Shih, K.; Yang, Z.; Li, X.; Wang, Z.; Wang, J., *Chem. Eng. J.*, **2017**, *321*, 495-501.
4. Casimir, A.; Zhang, H.; Ogoke, O.; Amine, J.C.; Lu, J.; Wu, G., *Nano Energy*, **2016**, *27*, 359-376.
5. Yang, Y.; Shu, D.; Yu, H.; Xia, X.; Lin, Z., *J. Power Sources*, **1997**, *65*, 227-230.
6. Shu, J.; Shui, M.; Huang, F.; Ren, Y.; Wang, Q.; Xu, D.; Hou, L., *J. Phys. Chem. C*, **2010**, *114*, 3323-3328.
7. Tran, D.T.; Dong, H.; Walck, S.D.; Zhang, S.S., *RSC Adv.*, **2015**, *5*, 87847-87854.
8. Kim, Y., *ACS Appl. Mater. Interfaces*, **2012**, *4*, 2329-2333.
9. Zeng, M.; Xiao, Y.; Liu, J.; Yang, K.; Fu, L., *Chem. Rev.*, **2018**, *118*, 6236.
10. Qiao, J.; Kong, K.; Hu, Z.; Yang, F.; Ji, W., *Nat. Commun.*, **2014**, *5*, 4475.
11. Paterson, A. F.; Anthopoulos, T.D., *Nat. Commun.*, **2018**, *9*, 5264.
12. Fortunato, E.; Barquinha, P.; Martins, R., *Adv. Mater.*, **2012**, *24*, 2945.
13. Klauk, H., *Organic Electronics: Materials, Manufacturing, and Applications*, John Wiley & Sons, Weinheim, Germany **2006**.
14. *Organic Electronics. 2: More Materials and Applications* (Ed: H. Klauk), Wiley-VCH-Verl, Weinheim, Germany **2012**.
15. Tang, Y.; Zhang, Y.; Deng, J.; Wei, J.; Tam, H.L.; Chandran, B.K.; Dong, Z.; Chen, Z.; Chen, X., *Adv. Mater.*, **2014**, *26*, 6111-6118.
16. Liu, S.; Wang, Z.; Yu, C.; Wu, H.B.; Wang, G.; Dong, Q.; Qiu, J.; Eychmüller, A.; Lou, X.W.; A. Eychmüller, A., *Adv. Mater.*, **2013**, *25*, 3462-3467.
17. Chernova, N.A.; Roppolo, M.; Dillon, A.C.; Whittingham, M.S., *J. Mater. Chem.*, **2009**, *19*, 2526-2552.
18. Mai, L.; Xu, L.; Han, C.; Xu, X.; Luo, Y.; Zhao, S. and Zhao, Y., *Nano Lett.*, **2010**, *10*, 4750-4755.
19. Li, Y.; Tan, B.; Wu, Y., *Nano Lett.*, **2008**, *8*, 265-270.
20. Simon, B.; Flandrois, S.; Guerin, K.; Fevrier-Bouvier, A.; Teulat, I.; Biensan, P., *J. Power Sources*, **1999**, *81*, 312-316.
21. Kasavajjula, U.; Wang, C.; Appleby, A. J., *J. Power Sources* **2007**, *163*, 1003-1039.

22. Ebata, H.; Izawa, T.; Miyazaki, E.; Takimiya, K.; Ikeda, M.; Kuwabara, H.; Yui, T., *J. Am. Chem. Soc.*, **2007**, *129*, 15732–15733.
23. Park, J.I.; Chung, J.W.; Kim, J.Y.; Lee, J.; Jung, J.Y.; Koo, B.; Lee, B.L.; Lee, S.W.; Jin, Y.W.; Lee, S.Y., *J. Am. Chem. Soc.*, **2015**, *137*, 12175–12178.
24. Yamashita, Y. et al., *Chem. Mater.* **2016**, *28*, 420–424.
25. Schott, S.; Gann, E.; Thomsen, L.; Jung, S.H.; Lee, J.K.; McNeill, C.R.; Sirringhaus, H., *Adv. Mater.*, **2015**, *27*, 7356–7364.
26. Mitsui, C.; Okamoto, T.; Yamagishi, M.; Tsurumi, J.; Yoshimoto, K.; Nakahara, K.; Soeda, J.; Hirose, Y.; Sato, H.; Yamano, A.; Uemura, T., *Adv. Mater.*, **2014**, *26*, 4546–4551.
27. Schweicher, G.; Lemaur, V.; Niebel, C.; Ruzié, C.; Diao, Y.; Goto, O.; Lee, W.Y.; Kim, Y.; Arlin, J.B.; Karpinska, J.; Kennedy, A.R., *Adv. Mater.*, **2015**, *27*, 3066–3072.
28. Podzorov, V.; Menard, E.; Borissov, A.; Kiryukhin, V.; Rogers, J.A.; Gershenson, M.E., *Phys. Rev. Lett.*, **2004**, *93*, 086602.
29. Schweicher, G.; Olivier, Y.; Lemaur, V.; Geerts, Y. H., *Isr. J. Chem.*, **2014**, *54*, 595–620.
30. Zhang, S.; Zhao, K.; Zhu, T.; Li, J., *Prog. Mater. Sci.*, **2017**, *89*, 479–521.
31. Xu, R.; Zhao, K., *J. of Electrochem. Energy Convers. Storage*, **2016**, *13*, 030803.
32. Kim, N.Y.; Yim, T.; Song, J.H.; Yu, J.S.; Lee, Z., *J. Power Sources*, **2016**, *307*, 641.
33. Lang, M.; Darma, M.S.D.; Kleiner, K.; Riekehr, L.; Mereacre, L.; Pérez, M.Á.; Liebau, V.; Ehrenberg, H., *J. Power Sources*, **2016**, *326*, 397.
34. Sun, G.; Sui, T.; Song, B.; Zheng, H.; Lu, L.; Korsunsky, A.M.; *Extreme Mech. Lett.*, **2016**, *9*, 449.
35. Koch, F. P. V.; Rivnay, J.; Foster, S.; Müller, C.; Downing, J. M.; Buchaca-Domingo, E.; Westacott, P.; Yu, L. Y.; Yuan, M. J.; Baklar, M., *Prog. Polym. Sci.*, **2013**, *38*, 1978–1989.
36. Bhandavat, R.; Pei, Z.; Singh, G., *Nanomater. Energy* **2012**, *1*, 324–337.
37. David, L.; Bhandavat, R.; Barrera, U.; Singh, G., *Nat. Commun.*, **2016**, *7*, 10998.
38. Ahn, D.; Raj, R., *J. Power Sources* **2010**, *195*, 3900–3906.
39. Shen, J.; Ahn, D.; Raj, R., *J. of Power Sources*, **2011**, *196*, 2875–2878.
40. Fukui, H.; Nakata, N.; Dokko, K.; Takemura, B.; Ohsuka, H.; Hino, T.; Kanamura, K., *ACS Appl. Mater. Inter.*, **2011**, *3*, 2318–2322.
41. Shen, J.; Raj, R., *J. Power Sources*, **2011**, *196*, 5945–5950.
42. Park, S. K.; Sun, H.; Chung, H.; Patel, B. B.; Zhang, F.; Davies, D. W.; Woods, T. J.; Zhao, K.; Diao, Y., *Angew. Chem. Int. Ed.*, **2020**, *59*, 13004.

## CHAPTER 2. ELECTRONIC STRUCTURE STUDY OF BATTERY MATERIALS

This chapter is based, in part, on the research described in the following publication

Sun, H.; Zhao, K., *J. Phys. Chem. C*, **2017**, *121*, 6002-6010.

### 2.1 Electronic Structure and Comparative Properties of $\text{LiNi}_x\text{Mn}_y\text{Co}_z\text{O}_2$ Cathode Materials

#### 2.1.1 Background and Motivation

Electrification of automotive transportation and integration of renewable energies constitute two critical pathways toward reduction of gas emissions and mitigation of environmental risks<sup>1</sup>. These imperative demands incur challenges in terms of energy storage technologies, for which Li-ion batteries emerge as a versatile and efficient option.  $\text{LiNi}_x\text{Mn}_y\text{Co}_z\text{O}_2$  ( $x+y+z=1$ ) is the state-of-the-art choice of cathode materials for high-capacity Li-ion batteries in the electric vehicle applications<sup>2, 3</sup>. NMC is formed by partially replacing Co in  $\text{LiCoO}_2$  by Ni and Mn to achieve the improved electrochemical performance while reducing the material cost<sup>4</sup>. The composition of Ni, Mn, and Co can be tuned to optimize the capacity, cyclic rate, electrochemical stability, and lifetime.

The class of NMC materials has the same hexagonal  $\alpha\text{-NaFeO}_2$  ( $R3m$ ) structure, where Li, O, and transition metals (TMs) occupy alternating atomic layers and the TM elements reside at the center of the O octahedron<sup>5</sup>. Ni, Mn, and Co contribute to the enhanced performance of NMC in different ways. Ni-rich compositions have high discharge capacity up to 202 mAh/g<sup>6</sup>, Mn-rich compositions maintain better cycle life and thermal safety, while Co-rich compositions provide excellent rate capability<sup>7</sup>. On the other hand, the addition of Ni and Mn is also associated with different challenges, for instance, Ni-rich cathode suffers from structural degradation during cycles because of the Ni mixing with the Li sites, while Mn-rich material has a reduced capacity because of the inactivity of  $\text{Mn}^{4+}$  during Li reactions<sup>8, 9</sup>. Therefore, there is an ample room to optimize the composition of the ternary material NMC to reach a balanced behavior among the capacity, rate capability, structural stability, and cyclability.

We study the electronic structure and valence states in NMC and compares the resulting electronic, structural, mechanical, and thermal properties of a class of NMC materials based on the first-principles theoretical calculations. We select five different NMC compositions,  $\text{LiNi}_{1/3}\text{Mn}_{1/3}\text{Co}_{1/3}\text{O}_2$  (NMC333),  $\text{LiNi}_{0.4}\text{Mn}_{0.4}\text{Co}_{0.2}\text{O}_2$  (NMC442),  $\text{LiNi}_{0.5}\text{Mn}_{0.3}\text{Co}_{0.2}\text{O}_2$  (NMC532),  $\text{LiNi}_{0.6}\text{Mn}_{0.2}\text{Co}_{0.2}\text{O}_2$  (NMC622), and  $\text{LiNi}_{0.8}\text{Mn}_{0.1}\text{Co}_{0.1}\text{O}_2$  (NMC811), to systematically vary the composition of the TM elements and map their physicochemical properties. The theoretical predictions are in excellent agreement with the existing experimental results. Furthermore, the superlattice ordering in NMC is largely unknown which prohibits the implementation of atomistic models of NMC. We screen 81 configurations for each composition and conclude that there is no long-range atomic ordering in the TM layer due to the mixture of ionic states and similar ionic radii of the TM elements.

### 2.1.2 Simulation Methods

**Supercell model.** The supercell models are built using Vienna Ab-initio Simulation Package (VASP)<sup>10, 11</sup>. The NMC supercell is constructed with the  $R3m$  space group, where Li, O, and TM occupy the  $3b$ ,  $6c$ , and  $3a$  sites, respectively. 120 atoms are contained for each NMC composition. Projector-augmented-wave (PAW) potentials are used to mimic the ionic cores, while the generalized gradient approximation (GGA) in the Perdew-Burke-Ernzerh (PBE) flavor is employed for the exchange and correlation functional. To model the Coulombic repulsion between localized electrons in TMs, DFT+U method is adopted. The Hubbard U-J values for Ni, Mn, and Co are set as 6.7, 4.2, and 4.91, respectively<sup>12</sup>. The plane-wave set is expanded within an energy cutoff of 520 eV. The  $2\times 1\times 1$  mesh of  $k$  points in the Monkhorst-Pack scheme is chosen for the Brillouin zone sampling. Energy optimization is considered complete when the magnitude of force per atom is smaller than  $0.04 \text{ eV}/\text{\AA}$ .

**Virtual crystalline approximation (VCA) method.** The VCA method significantly reduces the computational expense and smoothly handles all complicated stoichiometric portion of compositions. The VCA model for NMC contains 6 O atoms, 3 Li atoms, and 3 virtual TM atoms whose pseudopotentials are constructed within the first-principles VCA scheme. In the calculations of mechanical properties, electronic structure, and thermal properties, VCA models built by ABINIT and CASTEP are adopted. In ABINIT, norm-conserving pseudopotentials

generated by the Troullier-Martins method and local density approximation (LDA) of exchange correlation functional are used. A  $k$ -point mesh of  $6\times 6\times 2$  in Monkhorst-Pack scheme is adopted for Brillouin zone sampling. The first self-consistent convergence is achieved within an energy cut-off of 50 Hartree when the tolerant potential residual  $V(r)$  is less than  $1.0\times 10^{-18}$  Hartree. Before calculation, optimization of atom positions is done using the conjugated gradient method until the maximum force per atom is less than  $1\times 10^{-6}$  Hartree/Bohr. In CASTEP, the ultrasoft pseudopotentials are expanded within a plane-wave cutoff energy of 550 eV and generalized gradient approximation of PBE is described as the exchange-correlation functional. The  $k$ -point of  $6\times 6\times 2$  mesh is used in Brillouin zone sampling.

**Generation of 81 configurations for each NMC composition.** We adopt the structural evolutionary algorithm implemented in USPEX to create a series of different configurations for each NMC composition. The NMC lattice with  $R3m$  space group built by VASP is used as the seed structure. The successive 80 structures for each NMC composition are developed by four evolutionary generations using the merely permutation method, which randomly swaps the atomic positions of Ni, Mn, and Co in the lattice. Every structure created by USPEX is input and relaxed in VASP to obtain the free energy.

**COOP analysis.** The COOP analysis is implemented in the LOBSTER tool which generates the overlap population-weighted density of states by processing the electronic-structure output from the self-consistent simulations in VASP.

**Density of states.** Total density of states is calculated using the Fearing technique with a Fearing parameter of 0.005 Ha. Partial density of states for Li, O, and TM are plotted based on the tetrahedron method using a non-shifted  $k$ -point grid in the whole Brillouin Zone. Phonon frequencies are obtained by diagonalizing the dynamical matrix based on the density functional perturbation theory (DFPT). To compute the phonon band structure and phonon density of states in the Brillouin zone, an elaborate Fourier interpolation of force constants is used by a  $4\times 4\times 2$   $k$ -point sampling.

**Mechanical properties.** In the supercell model, we employ the uniaxial tension simulation in the three directions and calculate the average Young's modulus from the slope of the stress-strain curves. In order to avoid the uncertainty due to the structural deviation, five different atomic configurations for each NMC composition are adopted in VASP. In the VCA model, the matrix of elastic constants is calculated based on the elastic response with respect to

the displacement perturbation in full set of directions. The Voigt-Reuss scheme is employed to obtain the mechanical properties<sup>13</sup>. According to the Voigt approximation, bulk and shear modulus are obtained by:

$$B_V = \frac{1}{9} \{2(C_{11} + C_{22}) + 4C_{13} + C_{33}\}$$

$$G_V = \frac{1}{30} \{C_{11} + C_{12} + 2C_{33} - 4C_{13} + 12C_{44} + 12C_{66}\}$$

In terms of the Reuss approximation:

$$B_R = \{(C_{11} + C_{12})C_{33} - 2C_{12}^2\} / (C_{11} + C_{12} + 2C_{33} - 4C_{13})$$

$$G_R = \left(\frac{5}{2}\right) \{[(C_{11} + C_{12})C_{33} - 2C_{12}^2]C_{55}C_{66} / \{3B_V C_{55}C_{66} + [(C_{11} + C_{12})C_{33} - 2C_{12}^2]^2(C_{55} + C_{66})\}\}$$

Based on the above approximation, we obtain the effective moduli

$$B = \frac{1}{2}(B_V + B_R), \quad G = \frac{1}{2}(G_V + G_R)$$

Young's modulus is further calculated as:

$$Y = 9BG / (3B + G)$$

**Thermal properties.** Based on the phonon structure, thermal properties are calculated by the finite volume method using the quasi-harmonic approximation according to the following equations<sup>14</sup>:

$$F = 3nNk_B T \int_0^{\omega_{\max}} \ln \left\{ 2 \sinh \left( \frac{\hbar\omega}{2k_B T} \right) \right\} g(\omega) d\omega$$

$$S = 3nNk_B \int_0^{\omega_{\max}} \left[ \left( \frac{\hbar\omega}{2k_B T} \right) \coth \left( \frac{\hbar\omega}{2k_B T} \right) - \ln \left\{ 2 \sinh \left( \frac{\hbar\omega}{2k_B T} \right) \right\} \right] g(\omega) d\omega$$

$$C_v = 3nNk_B \int_0^{\omega_{\max}} \left( \frac{\hbar\omega}{2k_B T} \right)^2 \operatorname{csch}^2 \left( \frac{\hbar\omega}{2k_B T} \right) g(\omega) d\omega$$

### 2.1.3 Results and Discussion

We study the electronic structure and valence states in  $\text{LiNi}_x\text{Mn}_y\text{Co}_z\text{O}_2$  (NMC) materials and compare the resulting electronic, structural, mechanical, and thermal properties of a class of NMC compositions. Through intensive computational screening, we further show that long-range atomic ordering is absent in NMC lattice due to the mixture of the ionic states and similar

ionic radii of the TM elements. The first-principles modeling provides a theoretical foundation on a complete understanding of the physicochemical properties of NMC at the level of electronic structures.

### 2.1.3.1 Valence States and Bonding Analysis

Figure 2.1 shows the ionic radius and 3d electron population of the six TM ions<sup>15</sup>, Ni<sup>2+</sup>/Ni<sup>3+</sup>, Co<sup>2+</sup>/Co<sup>3+</sup>, and Mn<sup>3+</sup>/Mn<sup>4+</sup>. The size of the TM ions can be generally divided into two groups. The TM elements with low oxidation states (Ni<sup>2+</sup>, Co<sup>2+</sup>, Mn<sup>3+</sup>) have similar ionic radius in the range of 64 ~ 69 pm, while the high oxidation states (Ni<sup>3+</sup>, Co<sup>3+</sup>, Mn<sup>4+</sup>) are associated with smaller radius of 53 ~ 56 pm. Figure 1 also shows that the 3d orbital electron population splits into the *eg*\* level with a higher energy and the *t2g* level with a lower energy due to the  $\sigma$  interaction between TMs and O and the JT distortion effect<sup>16</sup>. The low-spin (LS) Co<sup>3+</sup>, Ni<sup>2+</sup>, and Mn<sup>4+</sup> are inactive JT ions. In comparison, the low-spin Ni<sup>3+</sup>, low-spin Co<sup>2+</sup>, and high-spin (HS) Mn<sup>3+</sup> with a singly occupied orbital at the *eg*\* level are active JT species.

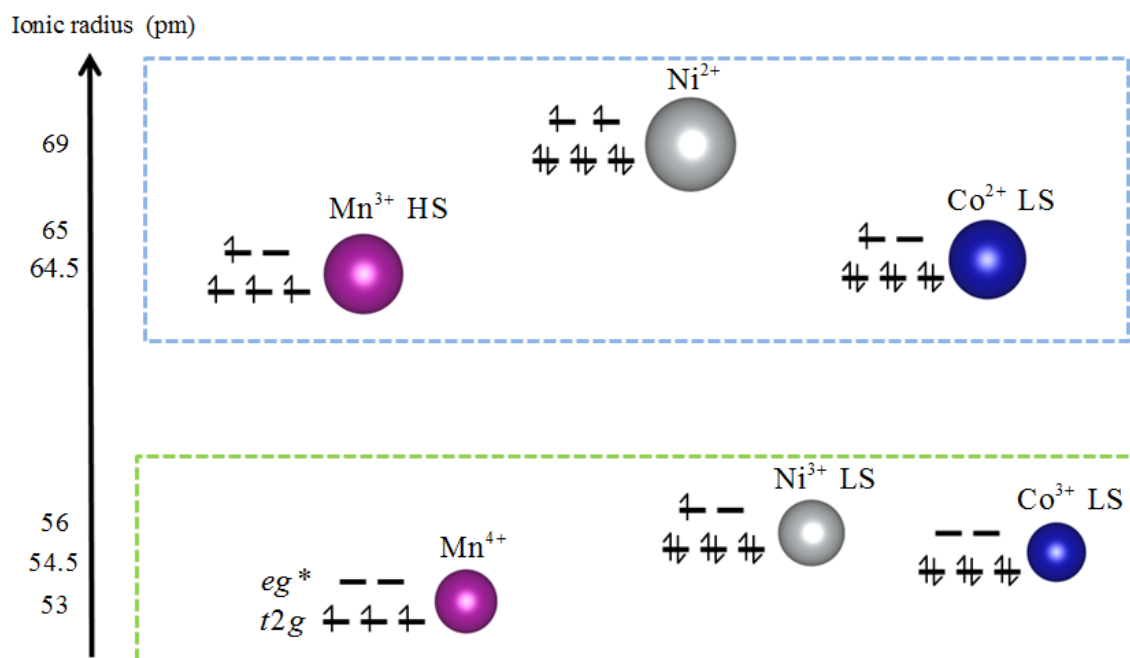


Figure 2.1. Ionic radius and 3d electron population of the six transition metal ions.

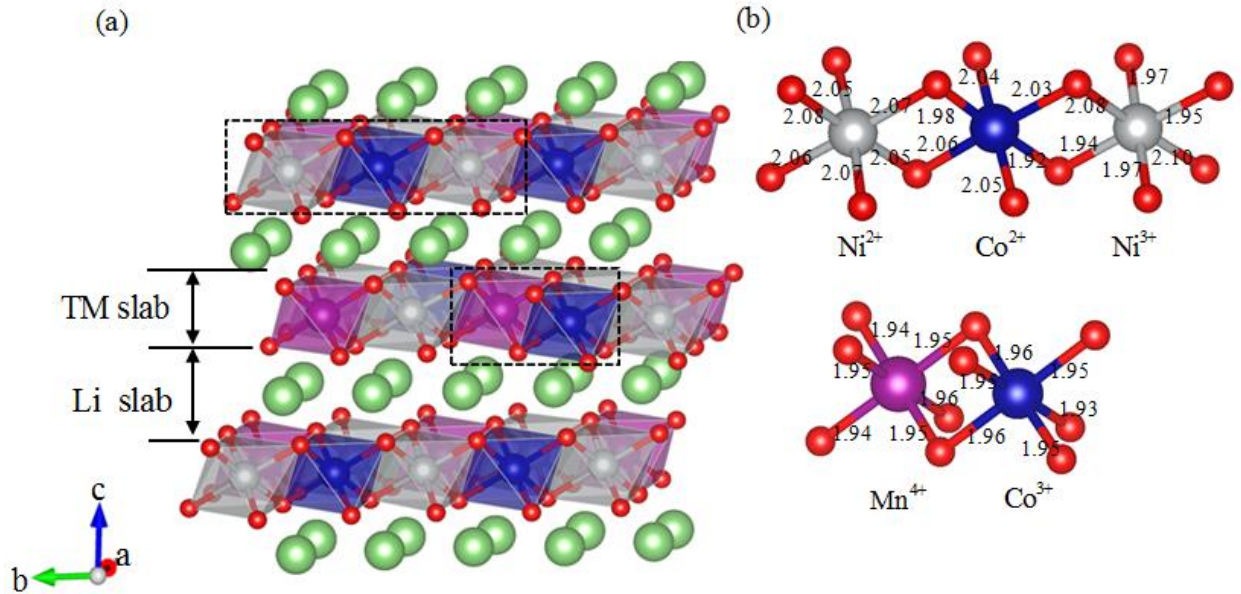


Figure 2.2. TM-O octahedral complexes in NMC. (a) Ni, Mn, and Co reside at the octahedral site surrounded by six O atoms. (b) Local view of the TM-O octahedral complexes. Ni<sup>3+</sup> and Co<sup>2+</sup> are active Jahn-Teller ions. Ni<sup>2+</sup>, Co<sup>3+</sup>, and Mn<sup>4+</sup> are inactive Jahn-Teller species. The degree of distortion of the octahedra indicates the ionic states of the TM elements. The grey, blue, and purple spheres represent Ni, Co and Mn atoms in the TM layer, respectively, and the red sphere represents O atoms.

The oxidation state of TM elements determines the JT effect as well as the TM-O bond length. Figure 2.2 (a) shows the atomic lattice of NMC. The TM elements reside at the octahedral site surrounded by six O atoms. Figure 2.2 (b) shows the local view of five representative TM-O octahedral complexes in the NMC lattice. Because of the multivalence state of Ni, Co, and Mn cations, different TM-O bond lengths co-exist for each TM element. We find that the TM-O bond length can be roughly divided into two groups, long bonds which are above 2.0 Å and short ones below 1.98 Å. The octahedra of inactive JT ions (Co<sup>3+</sup>, Ni<sup>2+</sup>, Mn<sup>4+</sup>) are of the similar bond length in the fourfold symmetry axes, while the active JT ions (Co<sup>2+</sup>, Ni<sup>3+</sup>, Mn<sup>3+</sup>) distort the octahedral complexes in one of the three fourfold symmetry axes – the short and long bonds co-exist in the TM-O octahedra, as shown in Figure 2.2 (b). Specifically, one of the fourfold axes in the Co<sup>2+</sup> octahedron shortens, while one axis in the Ni<sup>3+</sup> octahedron elongates, to form the distorted complexes. The bond length analysis and JT distortion in the TM-O octahedral complexes allow us to determine the ionic states of the TM elements. We perform radial distribution function analyses using a cut-off distance of 2.2 Å to calculate the population of the short and long TM-O bonds in the five NMC compositions. As shown in Table 2.1, all the Mn-O

bonds are short bonds of the length 1.94 ~ 1.96 Å, indicating that the Mn valence state is exclusively Mn<sup>4+</sup>. Based on the populated percentages of the short and long bonds of Ni-O and Co-O, we can determine the occupation fractions of Ni<sup>2+</sup>/Ni<sup>3+</sup> and Co<sup>2+</sup>/Co<sup>3+</sup> in the five NMC compositions.

Table 2.1 Population of the short (S) and long (L) TM-O bonds in the five NMC compositions.

NMC	Ni-O		Co-O		Mn-O
	S	L	S	L	S
333	0%	100%	86%	14%	100%
442	2%	98%	80%	20%	100%
532	8%	92%	64%	36%	100%
622	24%	76%	70%	30%	100%
811	38%	62%	100%	0%	100%

Figure 2.3 shows the occupation percentage of the Ni and Co cations as the NMC composition varies. In NMC333, NMC442, and NMC532, Ni<sup>2+</sup> is predominant over Ni<sup>3+</sup>, indicating an enhanced structural stability in the three compounds. As Ni content increases, the occupation of Ni<sup>3+</sup> steadily increases at the cost of Ni<sup>2+</sup>. The Ni<sup>3+</sup> fraction is up to 58% in NMC811 and the large fraction of Ni<sup>3+</sup> will deteriorate the structural stability in the Ni-rich compounds. This may explain the common observation that the high Ni-content NMC is more vulnerable of structural degradation – a mechanism in addition to the Li/Ni disorder effect in the electrochemical cycles. It is also worth pointing out that Ni occupies the largest portion among the three TM elements in NMC materials. The variation of Ni valence state will predominantly control the overall physicochemical properties of NMC cathodes. For Co, when the Ni composition increases, the fraction of Co<sup>3+</sup> first decreases until it reaches minimum in NMC532 and then gradually increases in NMC622 and NMC811. The occupation of Co<sup>2+</sup> shows the opposite behavior with a maximum fraction in NMC532. From the above analysis, we learn that NMC333, with the dominant inactive JT cations Ni<sup>2+</sup> and Co<sup>3+</sup>, possesses much improved structural stability over other compositions.

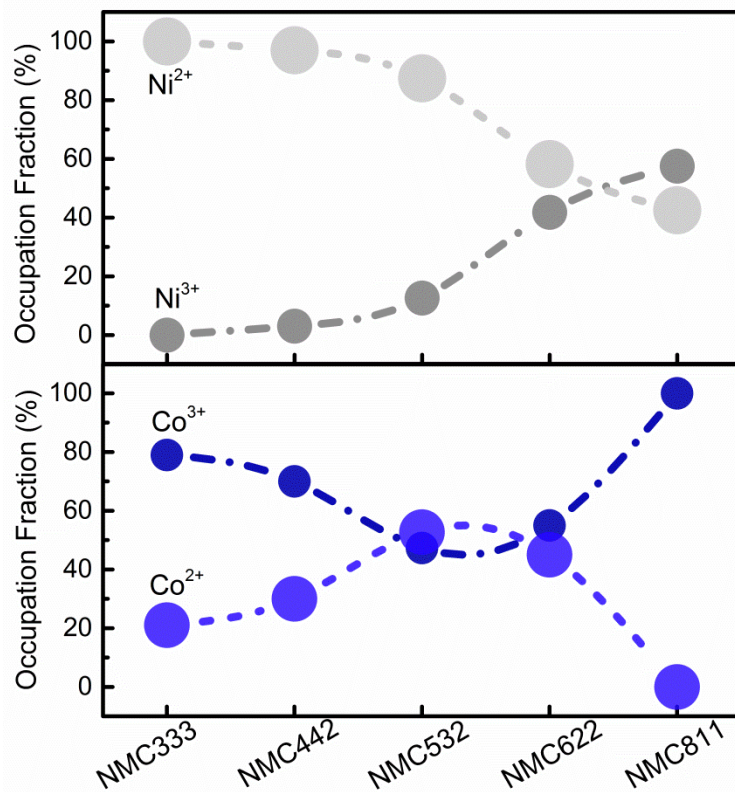


Figure 2.3. The occupation fraction of Ni<sup>2+</sup>/Ni<sup>3+</sup> and Co<sup>2+</sup>/Co<sup>3+</sup> in the five NMC compositions.

### 2.1.3.2 Atomic Ordering in Super-lattice

The atomic arrangement in the NMC lattice is elusive in literature. Based on the above analysis of the fractional occupation of TM cations, we expect that the co-existence of the aliovalent ions and similar ionic radii (Figure 2.1) would suppress the long-range atomic ordering in the TM layer of NMC. Figure 2.4 (a) shows the supercell structure of NMC with the space group  $R3m$ . The supercell contains 120 atoms with an alternative sequence of Li-O-TM layers along the  $c$ -axis. To explore the atomic ordering in the TM layer, we construct 81 distinct configurations for each NMC composition (details in the computational method section) and screen their energetics. In each configuration, the Ni, Mn, and Co sites are randomly assigned in the TM layer using the USPEX program<sup>17</sup>. We perform the energetic relaxation and classify the 81 configurations into five groups based on the energy difference per atom relative to lowest-energy configuration. In Figure 2.4 (b), each column represents the probability of NMC configurations within a given interval. In general, the maximum energy difference per atom in the overall 81 configurations for each composition is less than 0.05 eV. Considering that the

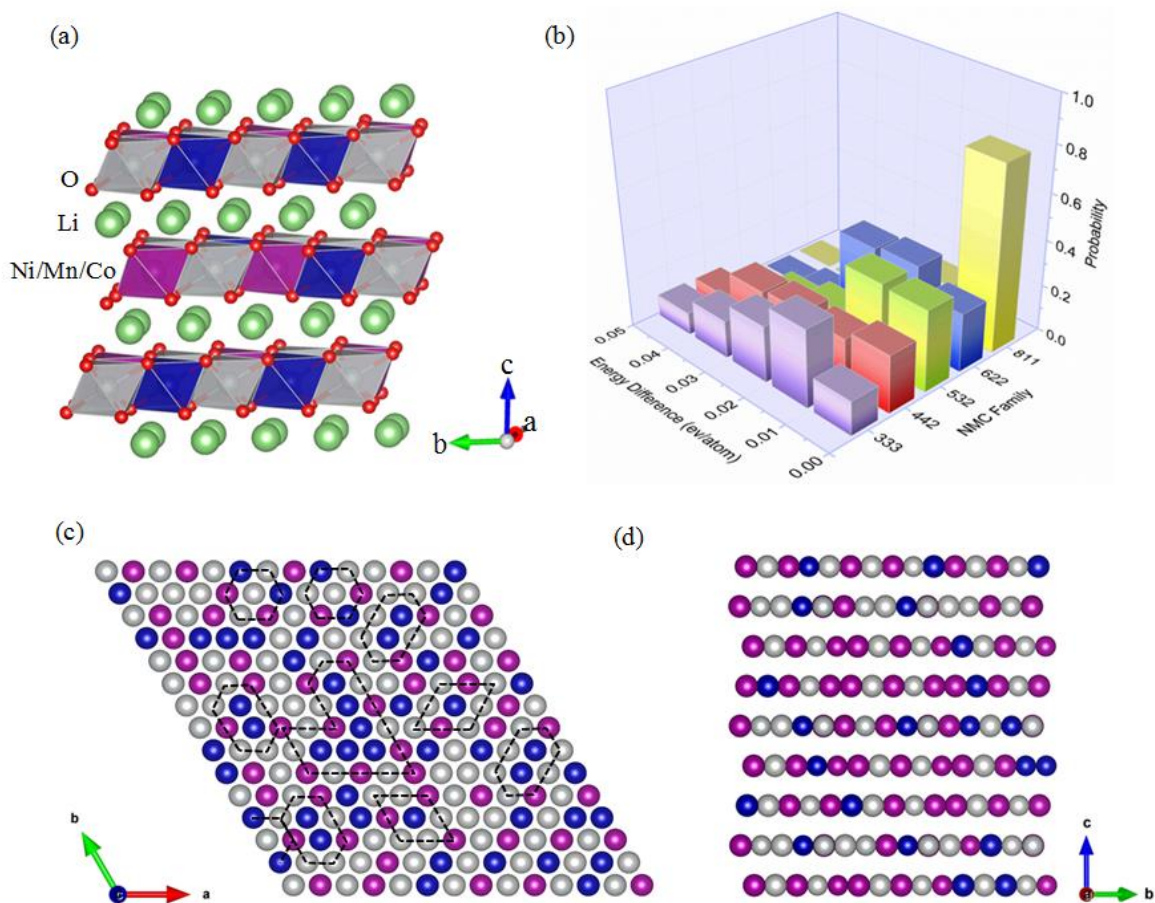


Figure 2.4. (a) NMC lattice with the  $R3m$  space group. (b) Population map of the 81 configurations for each NMC. Different configurations are made of different arrangements of Ni/Mn/Co in the TM layer. 81 configurations are constructed for each NMC composition and are categorized in five groups according to the difference of free energy per atom relative to the lowest energy state. Atomic arrangement from (c) the top-view and (d) the  $a$ -axis view of the TM layer in a NMC supercell consisting of 36 energetically favorable configurations. The dashed lines mark the possible cluster units. Multiple clusters with random population indicate the absence of long-range atomic ordering.

average energy per atom in the supercell is around 5.5 eV, the small energy difference per atom (less than 1%) among the 81 configurations indicates that the random arrangement of TM elements gives similar thermodynamics states of NMC. More specifically, the configuration population shows more even distribution for NMC333 and NMC442 due to the similar portions of Ni, Mn, and Co, which may provide more possibilities of atomic mixing. When the Ni content increases, most configurations are located in the regime of the small energy difference less than 0.03 eV, which may result from the similar coordination environment where Ni is dominant. It is clear that there is not a single favorable pattern of Ni, Mn, and Co, of long-range ordering, in the TM layer in the NMC supercell. We show the top-view (Figure 2.4 (c)) and the  $a$ -axis view

(Figure 2.4 (f)) of the atomic arrangement in the TM layer in a  $7\times 3\times 3$  supercell using a cluster expansion approach<sup>18</sup> that consists of 36 energetically favorable configurations of NMC532. The dashed lines mark the possible cluster units of TM elements. Multiple clusters of random geometries and population are observed, confirming that no specific ordering exists in the superlattice scale. This is consistent with the previous experiments using X-ray diffraction and neutron diffraction characterization on  $\text{Li}_{2/3}[\text{Co}_x\text{Ni}_{1/3-x}\text{Mn}_{2/3}]\text{O}_2$  which demonstrated that Co suppressed the superlattice ordering when  $x > 1/6$ <sup>19</sup>. A special note on NMC333 is that the valance states for Ni and Co are dominantly  $\text{Ni}^{2+}$  and  $\text{Co}^{3+}$ . The radii difference of  $\text{Ni}^{2+}$  and  $\text{Co}^{3+}/\text{Mn}^{4+}$  is larger than 15% which may lead to the short-range pattern<sup>20-22</sup>, while the long-range ordering is compromised by the co-existence of  $\text{Co}^{2+}$  and  $\text{Co}^{3+}$ . We calculate the population of the TM-TM pairs in NMC333. Table 2.2. Probability of TM-TM pairs in NMC333 shows that indeed the TM elements distribute dispersedly in the short range and thus a  $[\sqrt{3}\times\sqrt{3}]R30^\circ$ -type superlattice (in the Wood's notation) may exist for NMC333<sup>23</sup>.

Table 2.2. Probability of TM-TM pairs in NMC333

TM	Ni	Mn	Co
Ni	20.6%	35.3%	44.1%
Mn	35.5%	25.8%	38.7%
Co	41.6%	33.4%	25.0%

### 2.1.3.3 Comparative Properties of NMC Compositions

Next, we study the electronic properties of NMC and seek to understand the interactions of aliovalent TM cations with O. According to the ligand field theory, the interaction between TMs and the ligand (O) is mainly  $\sigma$ -bonding with small contribution of  $\pi$ -bonding in the TM-O octahedral complex<sup>24</sup>. Figure 2.5 shows an example molecular orbital diagram of the TM complex with the  $3d$  orbital electron population of  $\text{Co}^{3+}$  and O  $2p$  orbital. The  $eg$  level has a large overlap in the energy scale with the O  $2p$  orbital and constitutes the covalent bonding orbital with a large coefficient for the ligand orbital. The three degenerated  $t2g$  orbitals,  $d_{xy}$ ,  $d_{xz}$ , and  $d_{yz}$ , contribute to both the non-bonding and anti-bonding states. Other anti-bonding interactions are contributed by the two degenerated  $eg^*$  orbitals  $d_{z^2}$  and  $d_{x^2-y^2}$ <sup>25</sup>. The orbital interactions are depicted in the plot of density of states (DOS). Figure 2.6 shows the total and

partial DOS of the five NMC compositions. The dashed lines represent the total DOS. The blue, red, and green lines are the partial DOS of the TM 3d orbital, O 2p orbital, and Li s orbital, respectively. Fermi energy has been shifted to zero. Overall, there is little contribution of the Li s orbital in the energy range of -9 ~ 3 eV of the total DOS. Energy level below -4 eV shows a large

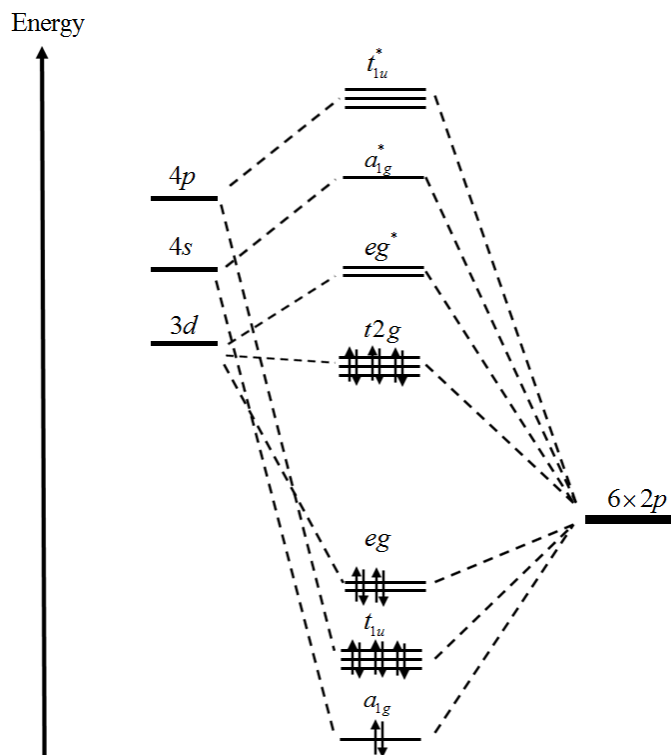


Figure 2.5. Molecular orbital diagram of the transition metal complex showing the *d* orbital electron population of  $\text{Co}^{3+}$  and O 2p orbital.

overlap between the O 2p and TM 3d orbitals due to the strong covalent interactions. The *t2g* population for the TM 3d orbital dominates the energy range of -2 to 0 eV. The higher energy region above the Fermi level represent the anti-bonding states between the *eg\** population in the TM 3d orbital and partial O 2p orbital. Comparing the DOS of the five NMC compounds, the Fermi energy shifts toward larger values when the Ni content increases because more valence electrons fill in the 3d orbital of Ni than Mn and Co. Furthermore, the band gap gradually closes from NMC333 to NMC811 indicating the metallic character of Ni-rich compounds. As discussed in Figure 2.3, when the Ni portion increases, more Ni transits to  $\text{Ni}^{3+}$  which increases the density of the electron/hole carriers and thus enhances the overall electrical conductivity<sup>26</sup>. Previous experimental measurements indeed showed a significant increase of electrical conductivity from

NMC333 to NMC811 that is in good agreement with the DOS plot<sup>7</sup>. Another interesting fact that stronger JT distortion associated with the Ni-rich compound is also reflected in the density of states. The ligand field theory indicates that the distorted bond in TM octahedral complexes result in further splitting of the  $t2g$  orbitals, leading to the partial electron occupation at a lower energy level. Figure 2.6 shows that the peak value of the  $t2g$  orbital decreases with more DOS filling in between the lower valence regime and the  $t2g$  peak. The DOS at the  $eg^*$  level slightly decreases as well because of the transition from  $Ni^{2+}$  to  $Ni^{3+}$  from NMC333 to NMC811.

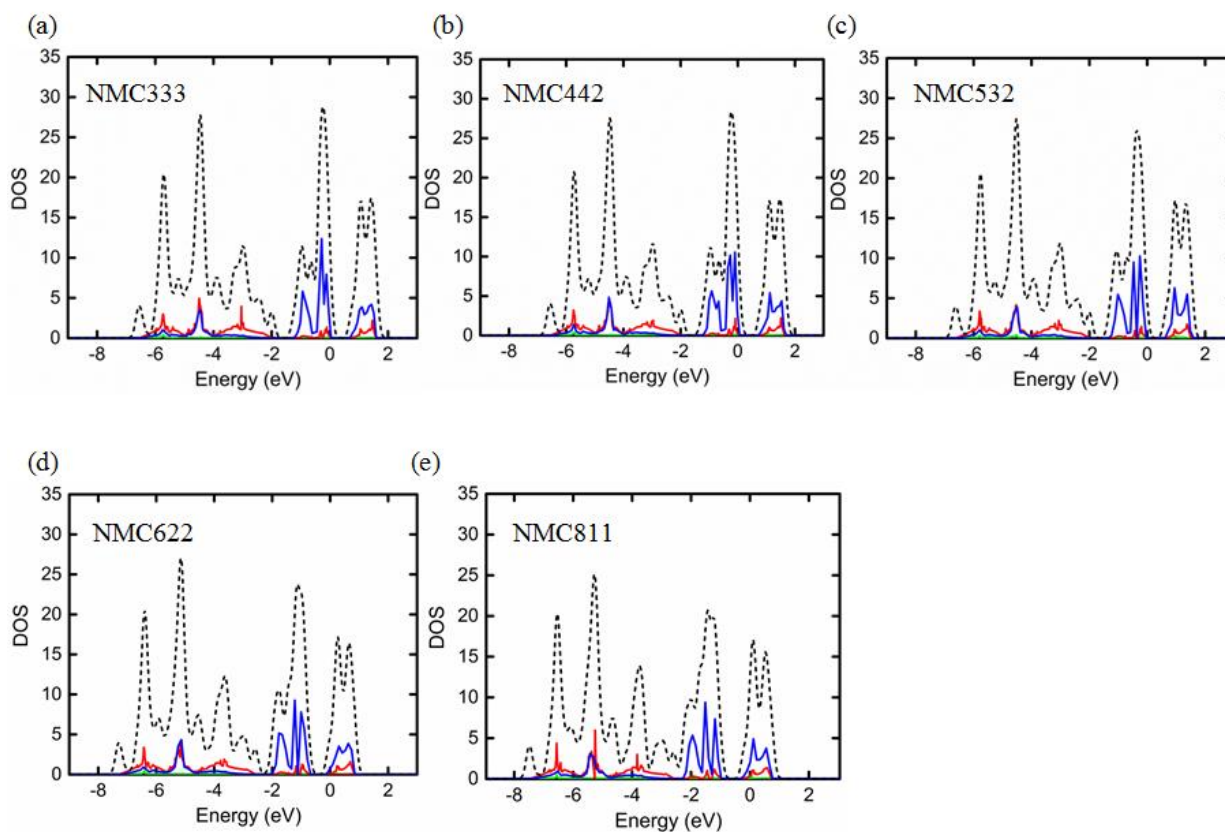


Figure 2.6. Total and partial density of states of (a) NMC333, (b) NMC442, (c) NMC532, (d) NMC622, and (e) NMC811, respectively. The dashed lines represent the total density of states. The blue, red, and green lines represent the partial density of states of the TM  $3d$  orbital, O  $2p$  orbital, and Li  $s$  orbital, respectively. Fermi energy is shifted to zero. Energy level below  $-4$  eV shows large overlaps between O  $2p$  and TM  $3d$  orbitals due to the strong covalent interactions. The  $t2g$  population for the TM  $3d$  orbital dictates the energy range of  $-2$  to  $0$  eV. The higher energy region above the Fermi level represents the anti-bonding states between the  $eg^*$  population in the TM  $3d$  orbital and partial O  $2p$  orbital. The band gap gradually closes and the Fermi energy shifts to larger values from NMC333 to NMC811 due to the increasing portion of Ni.

The comparative TM-O interactions can be revealed using the crystal orbital overlap population (COOP) analysis<sup>27</sup>. Figure 2.7 shows the COOP values for the TM-O pairs in

NMC333. Positive values represent the bonding states and negative values show the anti-bonding interaction. The broad positive regime around -5 eV correspond to the strong covalent bonding between the  $eg$  level and the O  $2p$  orbital. Around the Fermi level, the  $t2g$  level contributes to the anti-bonding and nearly non-bonding states at the Fermi level. In the conduction band, the COOP demonstrates the anti-bonding states between the  $eg^*$  level and partial O  $2p$  orbital. At the Fermi level, Co-O bond shows the minimum anti-bonding characteristic which might be related to the stable  $3d$ -electron configuration of  $Co^{3+}$ . Besides, less anti-bonding in the conduction band is observed for Ni-O compared with Mn-O and Co-O. Mn-O exhibits the largest anti-bonding effect which may elongate the TM-O bonds in Mn-rich NMC compounds.

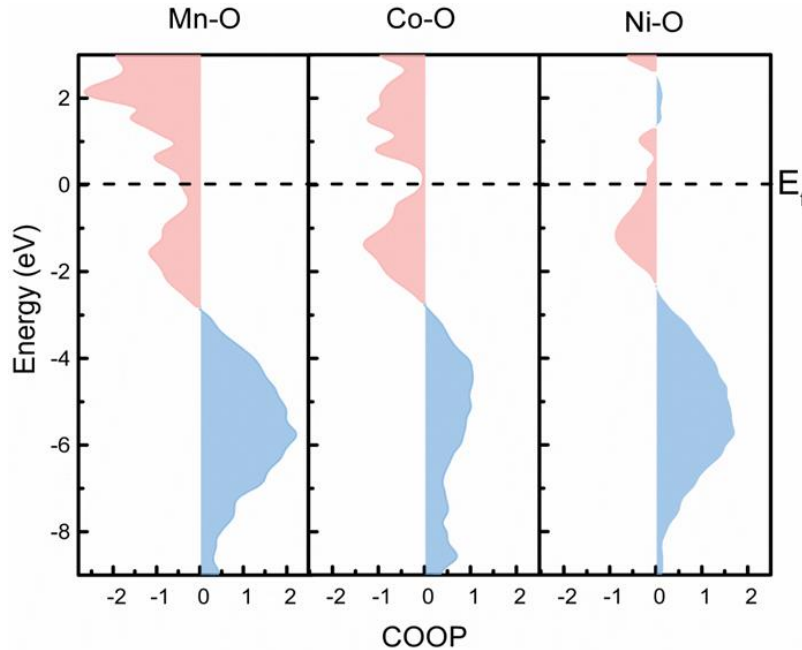


Figure 2.7. Crystal orbital overlap population analyses of the TM-O pairs. A positive value represents the bonding state, whereas a negative value shows the anti-bonding state. The broad bonding regime (-9 ~ -4 eV) corresponds to the strong covalent states between TMs and O. Near the Fermi energy, the  $t2g$  level contributes to the anti-bonding states and nearly no bonding at the Fermi level. Above the Fermi energy, negative COOP indicates the repulsion of TMs and O because of the interactions of the  $eg^*$  level and O  $2p$  orbital.

The TM-O and TM-TM interactions determine the lattice parameters of NMC. A slight change in the lattice parameters has a significant effect on Li transport. It was predicted that when the Li slab space (Figure 2.2) increases by 0.1 Å, the activation barrier of Li diffusion decreases by 100 meV<sup>28</sup>. Figure 2.8 (a) and (b) show the lattice constants in the  $a$ -axis and  $c$ -

axis directions of the five NMC compositions, respectively. The average (symbols) and standard deviation (error bars) are calculated from the 81 configuration for each NMC composition. The

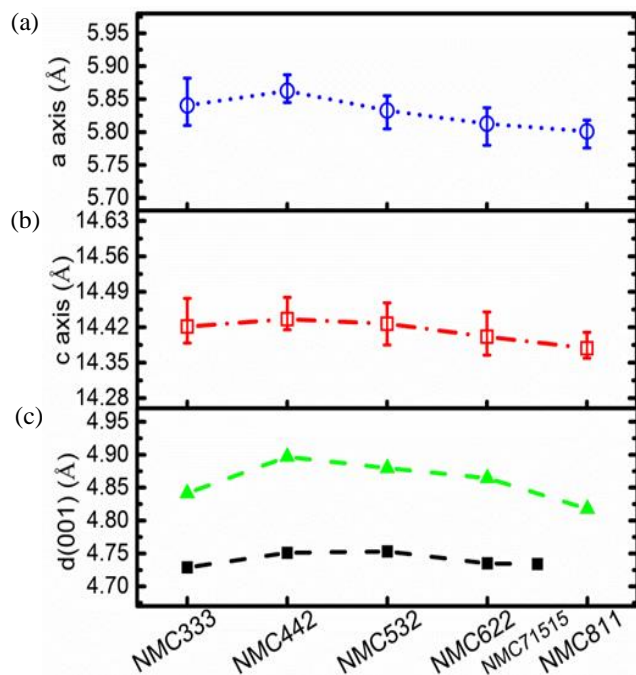


Figure 2.8. Lattice constants in (a) the *a*-axis and (b) the *c*-axis directions of the five NMC compositions. The average (symbols) and standard deviation (error bars) are calculated from the 81 configurations in each NMC composition. (c) Variation of the (001) plane spacing in different NMC compositions. The theoretical predictions (green line) show the same trend compared with the XRD measurement (black line).

lattice constants in the both orientations show the similar parabolic behavior and reach maximum in NMC 442. Figure 2.8 (c) plots the variation of the (001) plane distance in NMC in comparison with XRD measurements (black curve)<sup>29</sup>. The (001) plane distance is the sum of the Li slab and TM slab distances (Figure 2.2). Although a  $\sim 0.1$  Å systematic difference exists in the theoretical calculation compared with the experimental results which is mostly due to the generalized gradient approximation (GGA) correlation functional adopted in the DFT calculation, their results follow the exactly same trend. The lattice constants increase from NMC333 to NMC442 and then gradually decrease with the rise of the Ni content. Table 2.3 gives more detailed information on the average TM-O and TM-TM pairs. As expected, the TM slab and Li slab distances follow the same trend of the (001) plane distance. The general decrease of the *c*-axis lattice constant is due to the weaker anti-bonding effect of the TM 3*d* orbital as we discussed in Figure 2.6 when the Ni content increases. Meanwhile, since NMC442 contains the largest

content of Mn, and the Mn-O has the strongest repulsive interaction, the  $c$ -axis lattice parameter reaches maximum in NMC442. The TM-TM distance determines the  $a$ -axis lattice parameter. The average length of Ni-Mn and Ni-Co pairs are relatively larger than that of Mn-Co due to the larger ionic radius of Ni. Since NMC442 has the largest mixing of Ni and Mn, a relatively larger value of  $a$ -axis lattice constant is expected.

Table 2.3 TM and Li slab spacing and average bond length of TM-TM and TM-O pairs

NMC	Slab spacing ( $\text{\AA}$ )		Average length ( $\text{\AA}$ )					
	TM layer	Li layer	Ni-Mn	Mn-Co	Ni-Co	Mn-O	Ni-O	Co-O
333	2.19	2.64	2.93	2.89	2.92	1.95	2.06	1.99
442	2.23	2.66	2.93	2.91	2.92	1.95	2.07	1.99
532	2.23	2.65	2.91	2.91	2.92	1.94	2.05	1.98
622	2.22	2.64	2.91	2.88	2.91	1.94	2.02	1.97
811	2.19	2.63	2.91	2.85	2.88	1.94	2.00	1.94

Next, we explore the comparative mechanical, dynamic, and thermal properties of NMC materials and understand the electronic origin of the physicochemical properties. The finding that no long-range ordering is present in the TM layer of NMC allows us to use the virtual crystalline approximation (VCA) method which treats the TM elements as disordered alloying atoms (details in the computational method)<sup>30</sup>. The VCA model significantly reduces the computational cost and smoothly handles the stoichiometric variation in the five NMC compositions. Here we use both the supercell model and the VCA method to calculate the elastic modulus of NMC. Figure 2.9 shows the variation of Young's modulus in the five NMC compositions calculated by the two methods in comparison with the experimental values. The three solid lines show the Young's modulus calculated separately by VASP, CASTEP, and ABINIT. The green dots mark the experimental values of NMC333 and NMC532 measured by nanoindentation<sup>31-33</sup>. The theoretical predictions and experimental measurements quantitatively agree with each other. Elastic modulus monotonically decreases from NMC333 to NMC622 and then slightly increases in NMC811. Figure 2.5 shows the bulk modulus of the five NMC compositions calculated from the VCA model. NMC622 has the minimum values of both Young's modulus and bulk modulus. Mechanical properties are closely related with the electronic structure. The valence electron density (per atomic volume) determines the bulk modulus of materials and a large valence electronic density will result in a high bulk modulus.

From the DOS plot and the COOP analysis, we learn that the valence orbitals (*eg* level for TM and *2p* for O) contribute to the covalent bonding of TM-O, and the *t<sub>2g</sub>* and *eg\** levels contribute to the broad anti-bonding state. In the valence band (-9 ~ -3 eV, Figure 2.6), all the five NMC compositions have similar amount of valence electrons. Thus the TM atomic size will be a determining factor on the valence electron density. Considering the difference in the Co stoichiometry is small and Mn remains the same valence state in the different compounds, the variation of atomic size is mainly controlled by Ni. As Ni has larger ionic radii compared to Co and Mn (Figure 2.1), the overall average atomic size increases when the Ni composition increases. Therefore the valence electron density would generally decrease when the Ni content increases and so does the bulk modulus. Nevertheless, the ionic size decreases when a number of Ni cations undergo the transition from 2+ to 3+ oxidation state from NMC333 to NMC811. The above two competing factors on the ionic size result in the minimum valence electron density and modulus in NMC622 – the difference in the elastic modulus between NMC333 and NMC622 is around 21 GPa.

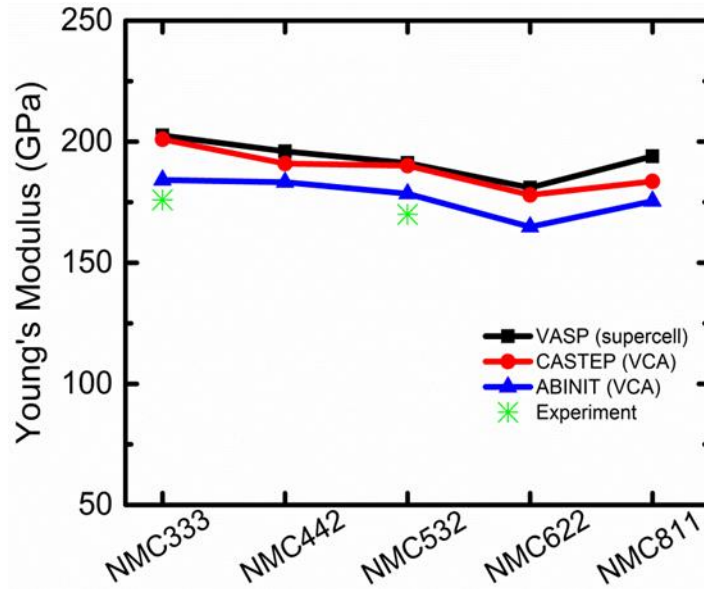


Figure 2.9. Young's modulus of the five NMC compositions calculated from the supercell model (VASP) and the virtual crystal approximation model (CASTEP and ABINIT) in comparison with the experimental values.

On the dynamic properties, Figure 2.10 (a)-(e) show the phonon dispersion curves for the phonon population along the  $\Gamma$ -K- $\Gamma$ -A-L path in the reciprocal space and the phonon density of states contributed by Li, O, and TMs in the five NMC compounds. The VCA model contains 12

atoms and thus there are 3 acoustic branches and 33 optical branches in the phonon dispersion curves. The acoustic branches locate at the lowest energy regime. Figure 2.10 (f) shows that the longitudinal acoustic frequency around the Gamma point gradually increases from NMC333 to NMC811 due to the weaker electron screening effect when the electron DOS at the Fermi level decreases (Figure 2.6). Furthermore, the low phonon frequency branches (marked by two arrows in (a)-(e)) slightly move toward a higher frequency regime when the Ni content increases. From the plot of phonon density of states, it shows that the medium and high frequency regimes are contributed by Li and O, and the low frequency regime is mainly contributed by the TM elements. The sharpening and shift of the two peaks in the low frequency regime indicate the strengthening of the TM-O bonds in the Ni-rich compound, which is consistent with the general decreasing lattice constant in the *c*-axis.

We further calculate the thermal properties of NMC including the vibrational Helmholtz free energy  $F$ , the vibrational entropy  $S$ , and the constant-volume specific heat capacity  $C_v$ . Figure 2.11 shows the results in the range of 50 K to 450 K. The thermal properties of the five NMC compounds are nearly identical and are similar to  $\text{LiCoO}_2$ <sup>14</sup>. This is understood that the crystalline symmetry mainly determines the thermal properties. Both  $\text{LiCoO}_2$  and NMC lattice have the  $R3m$  space group, resulting in similar phonon vibration modes in lattice. Figure 2.11 also shows that the heat capacity approaches to the classical Dulong-Petit asymptotic limit when the temperature increases to infinity. In the VCA model, the primitive cell contains 4 atoms. Thus the constant-volume heat capacity approaches the limit value of  $12R$  (99.7 J/mol/K, where  $R$  is the gas constant in the unit of J/mol/K) when temperature tends to the positive infinity. Thermal stability of the electrodes is a key issue for the safe operation of Li-ion batteries. We show the correlation of calculated cohesive energies, defined as the energy required to break the compositions up into isolated free atoms, with the thermal stability of the five NMC compositions in Figure 2.12. Thermal stability is represented by the exothermic reaction peak temperature in the calorimetry experiments<sup>34</sup>. The cohesive energy steadily decreases when the Ni content increases which corroborates that the thermal stability degrades in the Ni-rich compounds. The thermal stability is also closely related with the structural stability as a stable structure will experience a high phase transition temperature. Thus, the JT effect we discussed earlier can be an indicator of the thermal stability. Recall that the JT distortion in NMC is mainly

induced by the increasing portion of  $\text{Ni}^{3+}$ , the degradation of thermal stability in the Ni-rich compounds is expected.

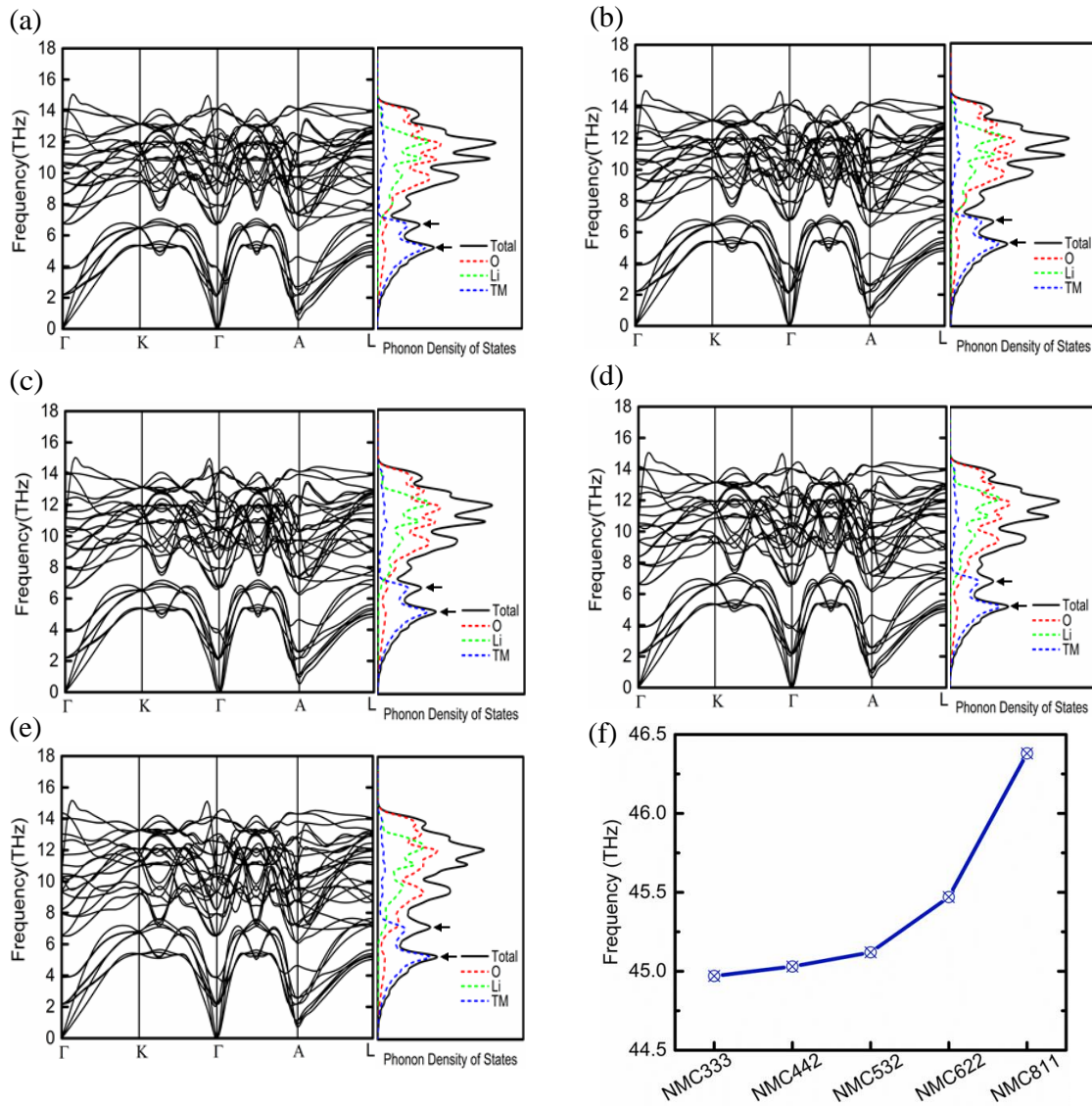


Figure 2.10. (a-e) Phonon dispersion and phonon density of states of NMC333, NMC442, NMC532, NMC622, and NMC811, respectively. In the phonon dispersion curves, the three lowest branches represent the acoustic mode and other thirty three branches represent the optical mode. In the DOS curves, the high- and medium-frequency regimes are contributed by Li and O, while the low-frequency regime is mainly contributed by TMs. From (a) to (e), the two peaks in the low-frequency regime sharpen and slightly shift toward higher values, indicating the increase of the TM-O bonding strength. (f) Longitude acoustic frequency in the five NMC compounds around the Gamma point. The acoustic frequency increases from NMC333 to NMC811 due to the weaker electron screening effect.

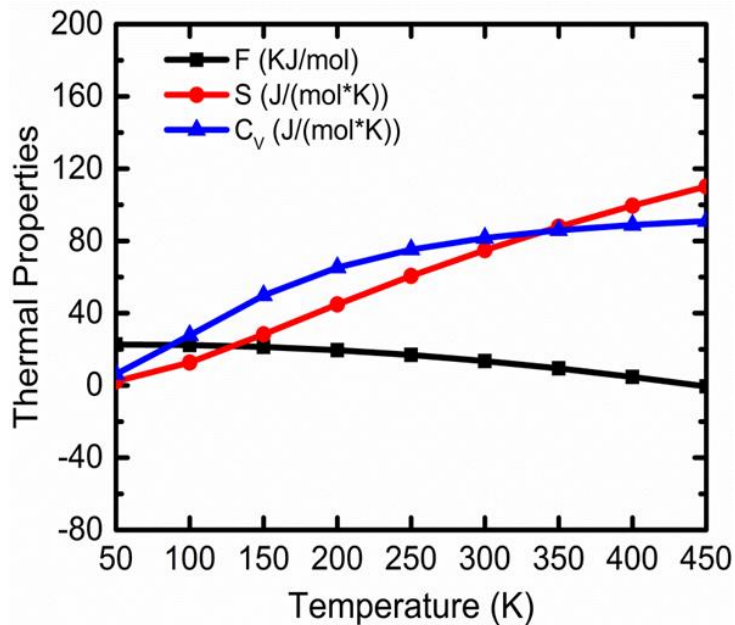


Figure 2.11. Thermal properties of NMC including the Helmholtz free energy  $F$ , the vibrational entropy  $S$ , and the constant-volume specific heat capacity  $C_v$ .

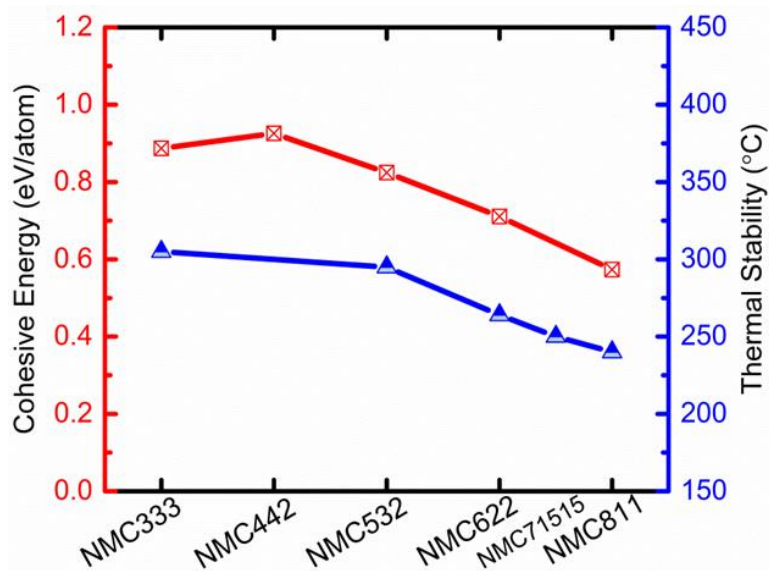


Figure 2.12. Thermal stability (experimental values, blue triangles) and cohesive energies (theoretical results, red rectangles) of the five NMC compositions. Thermal stability gradually degrades in the Ni-rich compounds.

## 2.2 Electron Density Analysis of Polarized Eutectic Electrolyte

### 2.2.1 Background

Conventional Li-ion batteries based on liquid electrolytes suffer from the tremendous concern of safety, capacity degradation, and issues of hermetic sealing. The emergence of solid state conducting electrolyte is anticipated to address the above issues, which has sparked vast attention in the battery field. While, the relatively low ion conductivity and poor mechanical strength of solid electrolytes impede their application in most Li-ion batteries. A new class of polymer/inorganic composites with eutectic interfaces is considered as a promising material to produce high performance solid state ion conductors. The high ionic conductivity can be achieved by engineering the highly polarized liquid-like eutectic interfaces which serve as efficient ion transport pathways. And, its mechanical modulus can be tuned by the selection of matrix polymer, the nature of functionalized fillers, and the interactions between polymers and fillers. A key challenge in synthesizing the eutectic solid electrolyte is to determine the proper portion of organic reactants to ensure the formation of the eutectic interface. A eutectic interface has a melting point (glass transition) much lower than either of the individual components, which presents locally liquid-like states in the solid ion conductors. By employing quantum chemistry simulation, we unveiled that the sufficient electron transfer and formation of hydrogen bonds are responsible for decreasing the melting point of mixtures and forming the eutectic interface.

### 2.2.2 Simulation Methods

The geometries of isolated choline-like chloride and urea molecules are optimized in Gaussian 09 package<sup>35</sup>. The hybrid functional B3LYP with the 6-31+G\*\* basis set is employed for all DFT calculations. The vibrational frequency analysis was performed to check if configurations reach optimized minima. In order to examine whether choline-like Cl and urea form the deep eutectic solvent (DES), we start to study the local cluster conformation composed of one choline-like Cl and two urea molecules according to molar ratio of 1:2. Three different initial cluster structures were constructed and optimized in Gaussian09 tool. The structure which reaches the best energy convergence is selected as the favorable initial cluster model. Then ab-initio MD was applied to further optimize this initial cluster model. Projector-augmented-wave (PAW) potentials with generalized gradient approximation (GGA) of PBE exchange and

correlation functional in VASP package<sup>10,11</sup> are used. Nosé thermostat maintains the temperature at  $T = 300$  K. Optimized structure is obtained when the total energy change is smaller than  $10^{-4}$  eV.

### 2.2.3 Results

To estimate interaction strength in the cluster model, we employ single point calculations to obtain the total free energy of isolated molecules and cluster structure. The interaction energy between choline-like chloride and urea molecules is determined as the energy difference between DES cluster and isolated molecules. An energy difference of  $-141.57$  kJ/mol indicates that the DES cluster configuration is energetically stable which means it's energy favorable for urea and chcl-like molecules to form local DES structure. The charge distributions also reflect the enhanced electrostatic interactions between chcl-like and urea molecules in DES cluster. The atomic charge population is calculated using the restrained electrostatic potential (RESP) charge derivation method. As shown in Figure 2.13, in the isolated choline-like chloride molecule, the computed charges over choline-like fragment and chloride are  $+0.774$  e<sup>-</sup> and  $0.774$  e<sup>-</sup>, respectively. However, in the cluster, the charge of choline-like fragment decreases to  $+0.747$  while chloride increase its charge to  $0.831$  e<sup>-</sup>. Some charges are transferred from chloride to two urea molecules as the cost of reducing coulombic attraction between choline-like and chloride ionic pair.

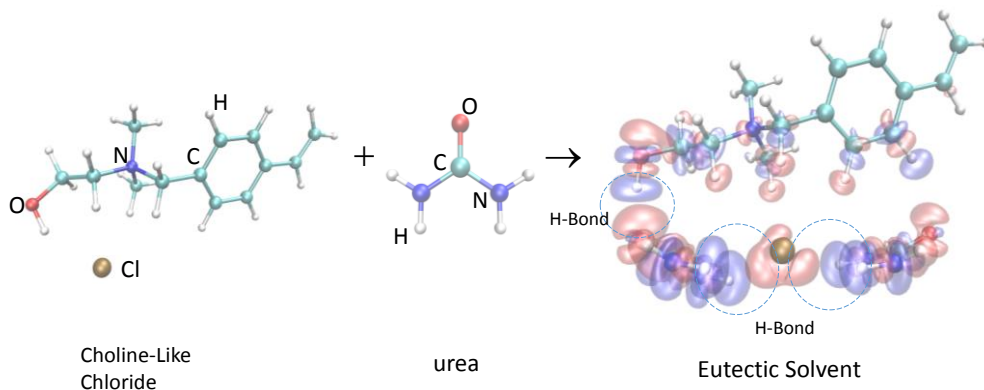


Figure 2.13. Optimized structures and charge distributions for choline-like chloride, urea and local DES cluster.

Electronic density difference population shows the electrostatic interaction among molecules in a more direct way. Difference map of electron density is plotted by Multiwfn software<sup>36</sup>. In

Figure 2.14, the red isosurfaces represent that electron density increased whereas the blue isosurfaces represent that electron density decreased after choline-like chloride and urea molecules form DES cluster. Obviously, the electron density is shifted from chloride to neighbor urea molecules. Also there exists electron transfer from oxygen atom in one urea molecule to the O-H group in choline-like fragment. These interactions correspond to two kinds of hydrogen bond. In order to quantify the interaction strength of these hydrogen bond, we calculate the ESP (electrostatic potential) at nuclear positions in the DES cluster. The interaction energy is obtained based on the ESP difference between the hydrogen donor and acceptor nucleus. As shown in fig2, the interaction energy between O atom in urea and O-H group in choline-like fragment is about -22.28kJ/mol, which is well consistent with the known O..H-O bond strength (21KJ/mol). The interaction energy between four H-N groups in urea and chloride are about 20 kJ larger than O ..H-O group, which means key interaction happens in urea-chloride pairs.

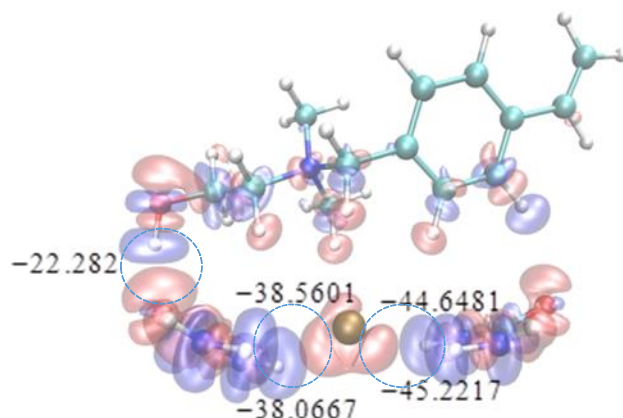


Figure 2.14. Calculated interaction energy for two types of hydrogen bonds in DES cluster.

From the above analysis, we confirm that it's locally favorable for choline-like chloride and urea molecules to form DES cluster due to enhanced electrostatic interaction of hydrogen bonds. In order to investigate the interaction in a larger scale, we perform ab-initio molecular dynamics modeling over an extended cluster model which consists of 208 atoms (Figure 2.15). The electron density analysis is conducted on selected cluster area. The strong interaction between urea molecules and choline-like chloride is confirmed in a large region. Besides, electron density

transfer between urea-urea, choline-like and chloride are also observed which indicates that a wide hydrogen bond network might be formed in large DES model.

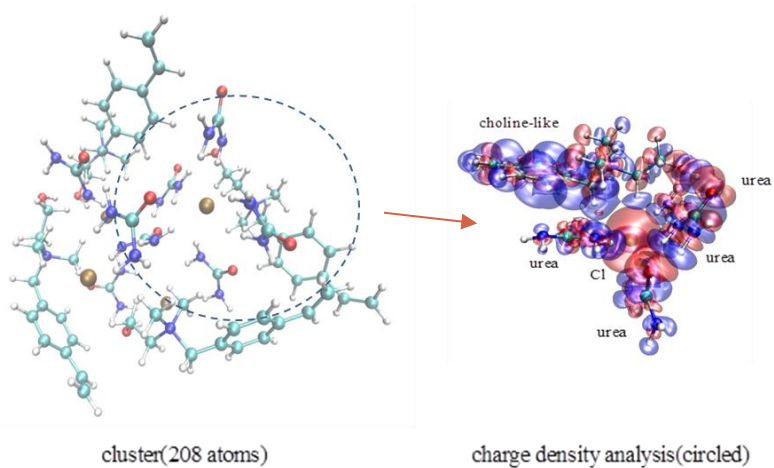


Figure 2.15. Extended cluster model(contains 208 atoms) after AIMD optimization and charge density analysis over circled area.

## 2.3 References

1. Palacín, M.; de Guibert, A., *Science* **2016**, *351*, 1253292.
2. Rozier, P.; Tarascon, J. M., *J. Electrochem. Soc.*, **2015**, *162*, A2490-A2499.
3. Mohanty, D.; Li, J.; Nagpure, S. C.; Wood, D. L.; Daniel, C., *MRS Energy Sustain.*, **2015**, *2*, E15.
4. Ohzuku, T.; Makimura, Y., *Chem. Lett.*, **2001**, *8*, 744-745.
5. Lu, Z.; MacNeil, D.; Dahn, J., *Electrochem. Solid-State Lett.*, **2001**, *4*, A200-A203.
6. Kim, M.-H.; Shin, H.-S.; Shin, D.; Sun, Y.-K., *J. Power Sources*, **2006**, *159*, 1328-1333.
7. Noh, H.-J.; Youn, S.; Yoon, C. S.; Sun, Y.-K., *J. Power Sources* **2013**, *233*, 121-130.
8. Etacheri, V.; Marom, R.; Elazari, R.; Salitra, G.; Aurbach, D., *Energy Environ. Sci.*, **2011**, *4*, (9), 3243-3262.
9. Xu, B.; Qian, D.; Wang, Z.; Meng, Y. S., *Mater. Sci. Eng.: R*, **2012**, *73*, (5), 51-65.
10. Kresse, G.; Furthmüller, *J. Phys. Rev. B*, **1996**, *54*, 11169.
11. Kresse, G.; Joubert, D. *Phys. Rev. B*, **1999**, *59*, 1758.
12. Zhou, F.; Cococcioni, M.; Marianetti, C. A.; Morgan, D.; Ceder, G., *Phys. Rev. B*, **2004**, *70*, 235121.
13. Bannikov, V. V.; Shein, I. R.; Ivanovskii, A. L., *Phys. Status Solidi (b)*, **2011**, *248*, 1369-1374.
14. Du, T.; Xu, B.; Wu, M.; Liu, G.; Ouyang, C., *J. Phys. Chem. C*, **2016**, *120*, 5876-5882.
15. Shannon, R. t., *Acta Cryst. Sec. A*, **1976**, *32*, 751-767.
16. Czyżyk, M.; Potze, R.; Sawatzky, G., *Phys. Rev. B*, **1992**, *46*, 3729.
17. Glass, C. W.; Oganov, A. R.; Hansen, N., *Comput. Phys. Commun.*, **2006**, *175*, 713-720.
18. Kubota, K.; Asari, T.; Yoshida, H.; Yaabuuchi, N.; Shiiba, H.; Nakayama, M.; Komaba, S., *Adv. Func. Mater.*, **2016**, *26*, 6047-6059.
19. Lu, Z.; Donaberger, R.; Dahn, J. *Chem. Mater.*, **2000**, *12*, 3583-3590.
20. Meng, Y.; Ceder, G.; Grey, C.; Yoon, W.-S.; Jiang, M.; Breger, J.; Shao-Horn, Y., *Chem. Mater.*, **2005**, *17*, 2386-2394.
21. Meng, Y.; Ceder, G.; Grey, C.; Yoon, W.-S.; Shao-Horn, Y., *Electrochem. Solid-State Lett.*, **2004**, *7*, A155-A158.
22. Wang, Y.; Xiao, R.; Hu, Y.-S.; Avdeev, M.; Chen, L., *Nat. Commun.*, **2015**, *6*, 6954.
23. Karino, W., *Ionics*, **2016**, *22*, 991-995.
24. Ballhausen, C. J., *Ligand field theory*. McGraw-Hill, New York: **1962**; Vol. 256.

25. Doublet, M.-L., *Orbital Approach to the Electronic Structure of Solids*. Oxford University Press: **2012**.
26. Kickelbick, G., *Hybrid materials: synthesis, characterization, and applications*. John Wiley & Sons: **2007**.
27. Dronskowski, R.; Bloechl, P. E., *J. Phys. Chem.*, **1993**, *97*, 8617-8624.
28. Kang, K.; Meng, Y. S.; Bréger, J.; Grey, C. P.; Ceder, G., *Science*, **2006**, *311*, 977-980.
29. Cui, S.; Wei, Y.; Liu, T.; Deng, W.; Hu, Z.; Su, Y.; Li, H.; Li, M.; Guo, H.; Duan, Y.; Wang, W.; Rao, M.; Zheng, J.; Wang, X.; Pan, F., *Adv. Energy Mater.*, **2016**, *6*, 1501309.
30. Hua, G.; Li, D. *RSC Adv.*, **2015**, *5*, 103686-103694.
31. Vasconcelos, L. S.; Xu, R.; Li, J.; Zhao, K., *Extreme Mech. Lett.*, **2016**.
32. Zeng, K.; Zhu, *J. Mech. Mater.*, **2015**, *91*, 323-332.
33. Kim, D.; Shim, H. C.; Yun, T. G.; Hyun, S.; Han, S. M., *Extreme Mech. Lett.*, **2016** *9*, 439-448.
34. Bak, S.-M.; Hu, E.; Zhou, Y.; Yu, X.; Senanayake, S. D.; Cho, S.-J.; Kim, K.-B.; Chung, K. Y.; Yang, X.-Q.; Nam, K.-W., *ACS Appl. Mater. Inter.*, **2014**, *6*, 22594-22601.
35. Frisch, M.; Trucks, G.; Schlegel, H.; Scuseria, G.; Robb, M.; Cheeseman, J.; Scalmani, G.; Barone, V.; Mennucci, B.; Petersson, G., *Gaussian 09 Package*. Gaussian. Inc.: Wallingford, CT, USA **2009**.
36. Lu, T.; Chen, F., *J. Comput. Chem.*, **2012**, *33*, 580-592

## CHAPTER 3. PHASE DYNAMICS AND ENERGY STORAGE MECHANISMS OF ELECTRODE MATERIALS

This chapter is based, in part, on the research described in the following publications

Sun, H.; Zhao, K., *ACS Appl. Mater. Interfaces*, **2017**, 9, 35001-35009.

Li, Y.; Sun, H.; Cheng, X.; Zhang, Y.; Zhao, K., *Nano Energy*, **2016**, 27, 95-102.

Xu, R.; Sun, H.; de Vasconcelos, L.S.; Zhao, K., *J. Electrochem.*, **2017**, 164, A3333-A3341.

### 3.1 Atomistic Origins of High Capacity and High Structural Stability of Polymer-derived SiOC Anode Materials

#### 3.1.1 Background and Motivation

Li-ion batteries (LIBs) are the current choice for powering portable electronics and electric vehicles. The capacity of a LIB is theoretically limited by the electrode materials. The most commonly used anode in LIBs is graphite due to its stable cycle ability, high Coulombic efficiency, and structural stability<sup>1</sup>. But the key drawback of low reversible capacity limits its application in high-energy-density batteries<sup>2</sup>. A variety of Si-based composites are currently being explored to replace the conventional graphite anodes. 1 Si atom can alloy with 3.75 Li atoms, while 6 C atoms can only host 1 Li, which results in the specific capacity of Si 10 times higher than that of graphite. However, the limiting factor with Si is the drastic volumetric change (up to 400%) associated with Li insertion and extraction, which causes tremendous mechanical issues in the practical implementation of Si anodes<sup>3,4</sup>. In fact, capacity and structural stability are mutually exclusive properties of most electrodes: A gain in capacity is often associated with the large volumetric change and sacrifice of the structural stability of the host material upon lithiation. To mitigate the mechanical failure of high-capacity electrodes, many novel hybrid chemistries and architectures have been proposed<sup>5-7</sup>. Nevertheless, a composite made of separate phases such as Si and C does not resolve the issue of intrinsic volumetric expansion and subsequent degradation of Si – the continuous shedding of Si upon lithiation cycles remains a major challenge in spite of many clever designs of composite structures.

So, a natural question is that, is there a compound, likely with hybrid Si-C atomic bonds, which can combine the strength of C (superior structural stability in lithiation cycles) and Si (high capacity) to overcome the tradeoff between capacity and mechanical stability? Polymer-

derived ceramics (PDCs, such as silicon oxycarbide) presents a viable solution<sup>8</sup>. The Si-based glass ceramics react with Li at a potential ranging from 0 to 2.5 V (v/s Li/Li+) and deliver a charge capacity of ~ 600 mAh/g with a robust mechanical stability over a thousand cycles<sup>9</sup>. Moreover, these ceramics can be conveniently molded into any desired shape, size, structure, or morphology as demanded by the application, and the final properties of the ceramics can be tailored by the type of the polymeric precursor and processing conditions<sup>10-13</sup>.

The electrochemical capacity of SiOC is attributed to its amorphous nano-domain structure, which is composed of segregated C network,  $\text{SiO}_x\text{C}_{4-x}$  tetrahedral units, and nano-voids<sup>9</sup>. This paper aims to explore the thermodynamics of Li reactions and microstructural evolutions in SiOC and to investigate the atomistic origins of the high capacity and high structural stability of the Si-based glass ceramic during Li insertion. We adopt a carbon-rich  $\text{Si}_{28}\text{O}_{42}\text{C}_{68}$  model to capture the salient features of Si-O-C composites: A continuous network of  $\text{SiO}_x\text{C}_{4-x}$  tetrahedral units are caged by graphene-like  $sp^2$  C cellular network while nano-voids are percolated in the lattice. The nano-domain size in the model is well consistent with the experimental result<sup>14</sup>. The high capacity originates from Li absorption at the percolated nano-void sites, followed by Li reactions with the C phase and Si-O-C units. The segregated  $sp^2$  C interface remains nearly inactive in the lithiation process and serves as the backbone to maintain the structural stability of the host material. SiOC expands up to 22% in volumetric strain after complete lithiation, which is several times smaller than the typical conversion- or insertion-type anode materials<sup>15</sup>. We perform detailed statistical analysis on the microstructural features, including the evolution of the local bonding environment, tetrahedral units, geometry perturbation and relaxation, and electron transfer, to provide complete understanding of the electro-chemo-mechanical behavior of the SiOC anode material.

### 3.1.2 Simulation Methods

#### 3.1.2.1 Model Generation

A reliable atomic structure of the glass ceramic is the key for small-scale quantum modeling. We generate the Si-O-C continuous network by randomly replacing O atoms in  $\text{SiO}_4$  tetrahedra by C. Different types of Si-O-C tetrahedron units including  $\text{SiO}_4$ ,  $\text{SiO}_3\text{C}$ ,  $\text{SiO}_2\text{C}_2$ , and  $\text{SiOC}_3$  are distributed in the network. The C-doped silica domain is caged by graphene-like cellular network.

The segregated C phase and the interface between the graphene-like C network and the Si-C-O units are generated by exploring over 180 possible local configurations using evolutionary algorithm implemented in USPEX program<sup>16</sup>. The optimized cluster model containing C network and  $\text{SiO}_x\text{C}_{4-x}$  units is input as the seed structure. The successive 180 structures are developed by 10 evolutionary generations, and each generation is produced by the combined variation method of heredity, random space group specificity, soft mutation, and lattice mutation. The most energetically favorable interface configuration is taken as the best structure. The whole amorphous cell is subject to annealing by ab-initio molecular dynamics. NVT ensemble is maintained by Nosé thermostat. Temperature is gradually increased from 300 K to 1200 K, and is maintained at a constant temperature 1200 K for 2 ps. Then the structure is slowly quenched from 1200 K to 300 K, and is energetically relaxed at 0 K. After the annealing and quenching process, the amorphous cell has a nano-domain size of  $\sim 1.5$  nm and a mass density of  $1.8 \text{ g/cm}^3$  which are in good agreement with the experimental measurements<sup>14, 17</sup>. The generated supercell contains the salient features of SiOC including the continuous Si-O-C network, segregated C interface, and nano-voids.

### 3.1.2.2 Computational Methods

We employ first-principles modeling within the framework of Density Functional Theory (DFT) to investigate the microscopic mechanism of lithiation in SiOC. Projector-augmented-wave (PAW) potentials in Vienna Ab-initio Simulation Package (VASP) are used to mimic the ionic cores, and the generalized gradient approximation (GGA) in the Perdew-Burke-Ernzerh (PBE) flavor is employed for the exchange and correlation functional<sup>18, 19</sup>. The atomic structures and system energy are calculated with an energy cutoff of 400 eV. For Brillouin zone sampling, a  $2 \times 2 \times 2$  mesh of  $k$  points in the Monkhorst-Pack scheme is sufficient in the energetic relaxation of  $\text{Li}_x\text{SiOC}$ . The energy optimization is considered complete when the magnitude of the force on each atom is smaller than  $0.04 \text{ eV} \cdot \text{\AA}^{-1}$ .

Energetic calculations are employed to examine the thermodynamics of Li insertion. We incrementally increase Li concentration to model the lithiation process. We consider *five* possible configurations of  $\text{Li}_x\text{SiOC}$  at a given Li concentration with different Li distributions in each, to eliminate the large variations inherent to the small model size. At each Li concentration, we perform the Delaunay triangulation analysis to identify the possible favorite sites for Li

insertion<sup>20, 21</sup>. Formation energy per Li at various Li concentrations is calculated to represent the thermodynamic driving force of Li insertion into SiOC. We take the energy of SiOC and the energy of a Li atom in its bulk form ( $E_{\text{Li}}$ ) as the reference energies, with  $E_{\text{nLi-SiOC}}$  being the total energy of the system containing  $n$  Li atoms in the cell. The formation energy per Li atom  $E_f(n)$  is calculated as  $E_f(n) = [E_{\text{nLi-SiOC}} - E_{\text{SiOC}} - nE_{\text{Li}}]/n$ .

The geometries of isolated Si-C-C-Si clusters before and after lithiation are studied by the molecular orbital analyses. The single point energy calculation of two configurations is performed to obtain the wave function of the particular arrangement of nuclei using Gaussian 09 package<sup>22</sup>. The hybrid functional B3LYP with the 3-21+G\* basis set is employed for the DFT calculations. The selected molecular orbitals of centered C atoms are plotted by Multiwfn software<sup>23</sup>. The blue and red iso-surfaces correspond to the positive and negative values of the wave function.

### 3.1.3 Results and Discussion

#### 3.1.3.1 Formation Energy during Lithiation Process

The polymer-derived SiOC has a heterogeneous molecular structure of amorphous nature, which contains silica domains, Si-O-C hybrid bonds, graphene-like carbon network, and nano-voids<sup>9</sup>. Figure 3.1(a) gives an overview of the carbon-rich SiOC supercell model with an applied period boundary condition. Figure 3.1 (b) shows the unit cell containing 28 Si atoms, 42 O atoms, and 68 C atoms. The lattice parameters of the amorphous unit cell are  $a = 1.4$  nm,  $b = 1.1$  nm, and  $c = 1.5$  nm, corresponding to the well accepted nano-domain size of SiOC (1~5 nm) in experimental measurement<sup>14</sup>. This size of the unit cell is consciously relatively small for the exploration of a large number of possible configurations of the glass ceramics with various Li concentrations. The choice of the model size affords our explorations at a reasonable computational cost without sacrificing the accuracy of the microscopic features of the heterogeneous structure. The gray atoms in Figure 3.1 (b) represent the segregated C phase which forms the stable backbone of the molecule structure. In the graphene-like C regime, topological defects such as five or seven-membered C rings exist. The vertex-sharing tetrahedra represent the randomly distributed Si-O-C units. After annealing, the excess C atoms are distorted to form short C-C chains<sup>24</sup>. Many of the C atoms are unsaturated with dangling bonds.

Different types of  $\text{SiO}_x\text{C}_{4-x}$  tetrahedral units including  $\text{SiO}_4$ ,  $\text{SiO}_3\text{C}$ ,  $\text{SiO}_2\text{C}_2$ , and  $\text{SiOC}_3$  are included in the network<sup>25</sup> which are highlighted in Figure 3.1 (b). The blue dotted circles mark the nano-void regimes percolated in the unit cell, which contribute to the low density of SiOC molecule ( $\sim 1.8 \text{ g/cm}^3$ )<sup>17</sup>.

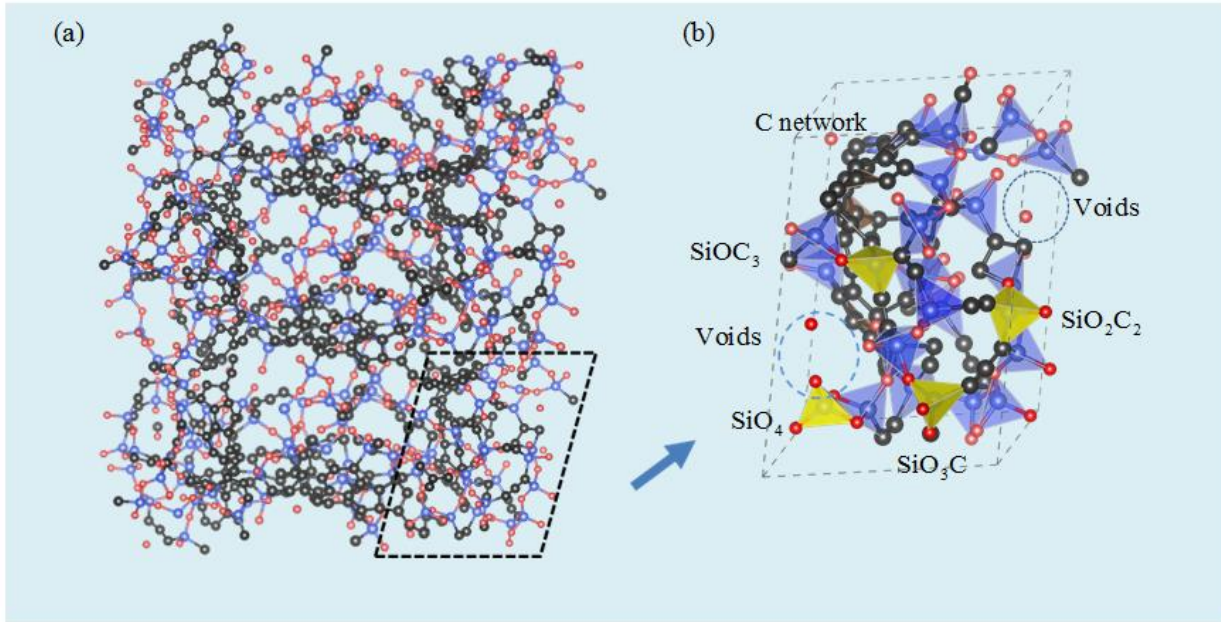


Figure 3.1. The atomic model of silicon oxycarbide (SiOC) consisting of the C phase,  $\text{SiO}_x\text{C}_{4-x}$  units, and nano-voids. (a) An overview of the supercell with an applied periodic boundary condition. (b) The unit cell shows a series of vertex-sharing tetrahedra including  $\text{SiO}_4$ ,  $\text{SiO}_3\text{C}$ ,  $\text{SiO}_2\text{C}_2$ , and  $\text{SiOC}_3$ . The gray atoms represent the segregated C phase which forms the backbone of the network. Excess C atoms are randomly distributed and topological defects of five and seven C-C rings exist. The blue dotted circles mark the nano-voids percolated in the lattice which contribute to the low density of SiOC molecule.

Figure 3.2 (a) shows the formation energy per Li in lithiated SiOC. The solid line represents the average values from five different configurations for each Li composition, and the error bars (the height of the shaded area at a given Li concentration) represent the standard deviation. The negative formation energy indicates that Li reaction is thermodynamically favorable. The lithiation process can be roughly divided into two stages, Li absorption at the nano-voids in I and Li alloying with SiOC units, excess C atoms, and the defect sites within the C network in II. The two-step lithiation is reflected in the variation of the slope of the formation energy with a transient composition of  $\text{Li}_{42}\text{Si}_{28}\text{O}_{42}\text{C}_{68}$ . The first stage is marked with the red line. The initial open structure provides a variety of spots and a large driving force for Li to insert. The formation energy per Li in a given composition shows a relatively large variation because of the different

local bonding environment in the nano-void regimes where Li gradually fill in. In the second stage (blue line) where Li composition is higher than  $\text{Li}_{42}\text{Si}_{28}\text{O}_{42}\text{C}_{68}$ , the nano-voids are nearly saturated. The thermodynamic driving force for Li insertion decreases. The variation of formation energy per Li in the five different configurations with the same Li concentration becomes small, which implies that the local chemical environments for Li reactions are roughly the same. Figure 3.2 (b) plots the volumetric strain of SiOC as a function of Li concentration which again delineates the two-step lithiation. When Li concentration is below  $\text{Li}_{42}\text{Si}_{28}\text{O}_{42}\text{C}_{68}$ , the volume of SiOC decreases because of the structural relaxation mediated by Li. Li fills the nano-voids and tightens the structure through the electrostatic interaction with the surrounding anionic O atoms and unsaturated C atoms. This behavior is consistent with a previous study on  $\text{Li}_{1/2}\text{SiC}_{1/4}\text{O}_{7/4}$ <sup>26</sup> as well as the experimental observation of Li intercalation in microporous Si-O-C composite materials<sup>14</sup>. When the transient composition  $\text{Li}_{42}\text{Si}_{28}\text{O}_{42}\text{C}_{68}$  is passed, the volumetric strain increases linearly with a partial molar volume of Li  $\Omega = 10.0 \text{ \AA}^3$  which is close to the partial molar volume of Li in pure silica<sup>21</sup>. SiOC expands by 22% in volumetric strain upon the full lithiation capacity 1230 mAh/g. It is worth noting that the volumetric strain of SiOC is much smaller than that of conversion- or insertion-type high-capacity anodes which are typically on the order of magnitude of 100%<sup>15</sup>. The small volumetric change retains the mechanical stability of SiOC in the course of lithiation and grants the glass ceramic an exceptional combination of high-capacity and high structural stability. The two-step lithiation is accompanied by continuous structural rearrangement of SiOC which will be closely examined as follows.

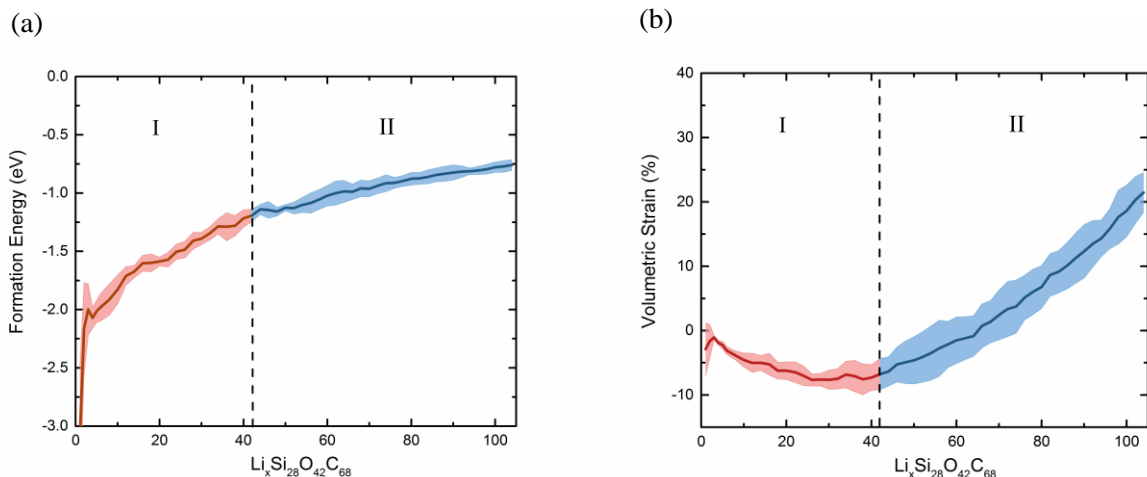


Figure 3.2. Two-step lithiation of SiOC shown in (a) the formation energy per Li in  $\text{Li}_x\text{SiOC}$  and (b) the volumetric strain as a function of Li concentration. The solid lines represent the average values of the formation energy per Li or the volumetric strain from the five configurations at a given Li concentration, and the error bars represent the standard deviation. The red lines indicate Li intercalation at the nano-voids. The formation energy per Li in this stage shows a large variation at a given Li concentration because of the large difference in the local bonding environment. The lattice volume decreases due to the structural relaxation mediated by Li insertion. The blue lines delineate Li reactions with the SiOC tetrahedron units and the C phase. Both the formation energy and volumetric strain reach a steady slop as Li inserts in stage II.

### 3.1.3.2 Structural Evolution upon Lithiation

To explore the structural evolution of SiOC upon lithiation, the statistics of the local bonding environment, including the coordination number, radial distribution function, and the number of SiOC tetrahedral units, are analyzed and plotted in Figure 3.3.

Figure 3.3 (a) shows the variation of the coordination number of Si-O, C-C, and Si-C in different  $\text{Li}_x\text{SiOC}$  compositions, respectively. The three solid lines represent the average values from the five different configurations for each composition, and error bars represent the standard deviation. To have a physical measure of the atomic coordination, we define Si-O, C-C, Si-C, Li-C, Li-O atoms to be bonded if their distances are within 110% of their original bond length in bulk lattice which are determined by X-ray and neutron diffraction<sup>27-30</sup>, corresponding to the values of 1.85 Å, 1.65 Å, 2.09 Å, 2.35 Å, and 2.16 Å, respectively. Overall, the coordination numbers of Si-C and C-C remain nearly constant through the entire lithiation process. In the first stage of lithiation (Li composition below  $\text{Li}_{42}\text{Si}_{28}\text{O}_{42}\text{C}_{68}$ ), the coordination number of Si-O decreases slowly showing that little change in chemical bonding is involved as Li gradually fills in the nano-voids. After saturation of the nano-voids (Li composition above  $\text{Li}_{42}\text{Si}_{28}\text{O}_{42}\text{C}_{68}$ ),

further Li insertion is accommodated by the breaking of Si-O bonds which results in the decrease of coordination number of Si-O at a constant rate.

Figure 3.3 (b) shows that Li is mainly attracted by O and C atoms as seen in the monotonic increase of the coordination number of Li-O and Li-C. The interaction of Li with anionic O tends to break the Si-O bonds and forms new bonds of Li-O during lithiation. Furthermore, the unsaturated C atoms provide additional site to accommodate Li insertion through geometry optimization and bonds switching, with more details discussed in Figure 3.4, instead of through the C-C or Si-C bond breaking mechanism.

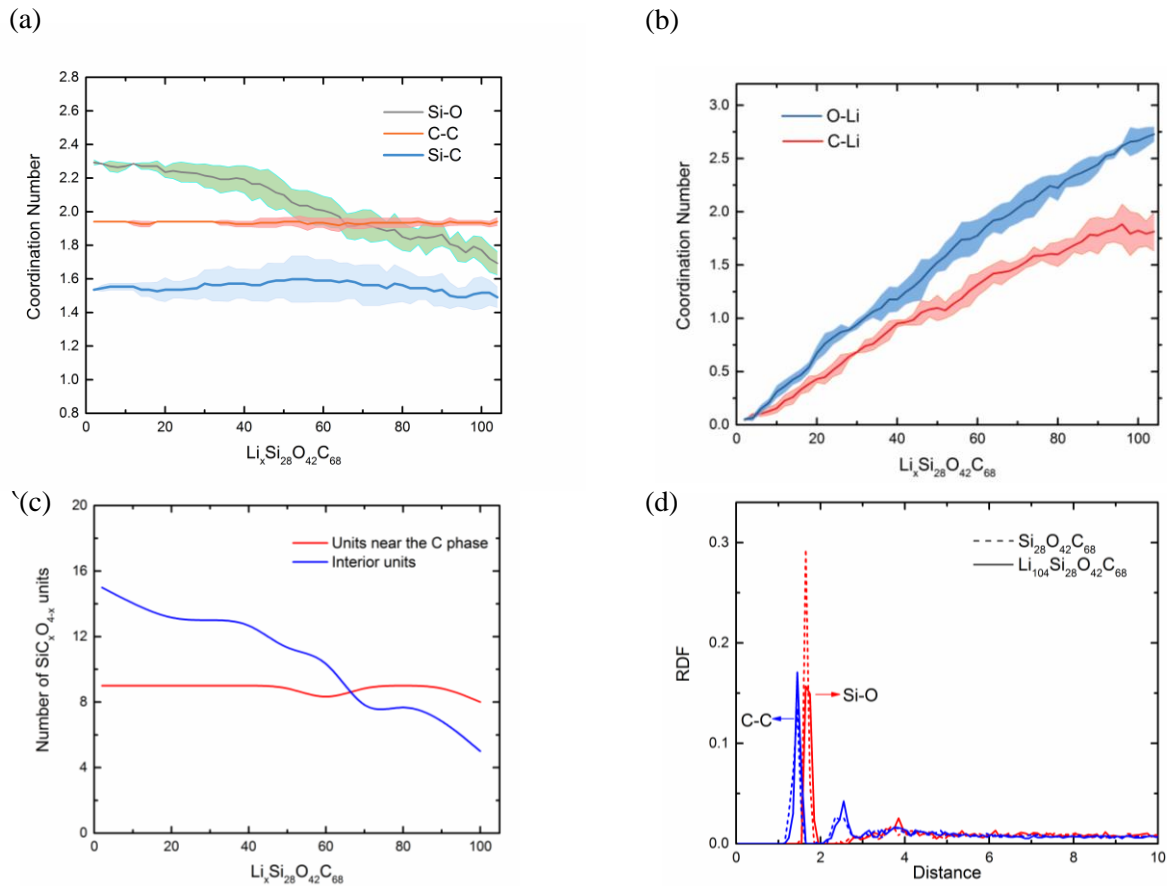


Figure 3.3. The structural feature of lithiated SiOC represented by (a) the coordination number of Si-O, C-C, and Si-C, (b) the coordination number of O-Li and C-Li, (c) the number of SiO<sub>x</sub>C<sub>4-x</sub> tetrahedral units, and (d) the radial distribution function (RDF) of Si-O and C-C before and after lithiation. The coordination number in (a) corroborates the two-step lithiation that little change of chemical bonding is involved when Li composition is below Li<sub>42</sub>Si<sub>28</sub>O<sub>42</sub>C<sub>68</sub>, while further lithiation is associated with the breaking of Si-O bonds. The increasing coordination number of O-Li and C-Li in (b) indicates that Li are attracted by the O and C atoms. The statistics of SiO<sub>x</sub>C<sub>4-x</sub> tetrahedral units in (c) shows that the number of the interior units caged in the network steadily decreases, while the units residing in the vicinity of the segregated C phase remain nearly unperturbed upon lithiation. The RDF of Si-O and C-C in (d) again shows the local stable bonding of C-C and severe breaking of Si-O when Li inserts.

The statistical evolution of the SiOC tetrahedral units provides more information on the structural transformation of the amorphous network. We plot the evolution of the number of the tetrahedral units as a function of Li concentration in

Figure 3.3 (c), in which the red line represents the variation of the Si-O-C units close to the segregated C network, and the blue line shows the number of tetrahedral units located inside the lattice and are caged by the C cellular network. It should be noted that there is no clear bounds between the two types of units. The statistics rather offers qualitative understanding on the Li reaction pathway. The number of the tetrahedral units caged in the network follows the same steady-decreasing trend of the coordination number of Si-O. On the contrary, the tetrahedral units residing nearby the C network remains almost unperturbed during lithiation. Li insertion mainly causes the structural rearrangement within the Si-O-C network while the segregated C phase with the surrounding tetrahedral units is mostly preserved. The  $sp^2$  graphene-like carbon network functions as the backbone to stabilize the entire molecule structure during lithiation. A similar finding was reported in a previous modeling of carbon-rich SiOC structures<sup>31</sup>.

Figure 3.3 (d) shows the comparison of radial distribution function (RDF) of Si-O and C-C bonds in pristine and fully lithiated SiOC. For the Si-O bond, the peak of RDF significantly decreases after lithiation, which originates from the Si-O bond breaking and dissociation of the tetrahedral units. The difference between the RDFs of C-C before and after lithiation is very small thanks to the stable bonding of C-C.

In summary, the local bonding statistics reveals the following facts: 1) little change of chemical bonding is involved when Li fills in the nano-voids from the pristine SiOC. 2) When the nano-voids are saturated, Li insertion is accommodated by the Si-O bond breaking and unsaturated C atoms in the interior SiOC tetrahedral units as well as the topological defects at the edge of or within the carbon network. 3) The segregated  $sp^2$  C interface remains inactive during lithiation and maintains the mechanical stability of the molecule structure.

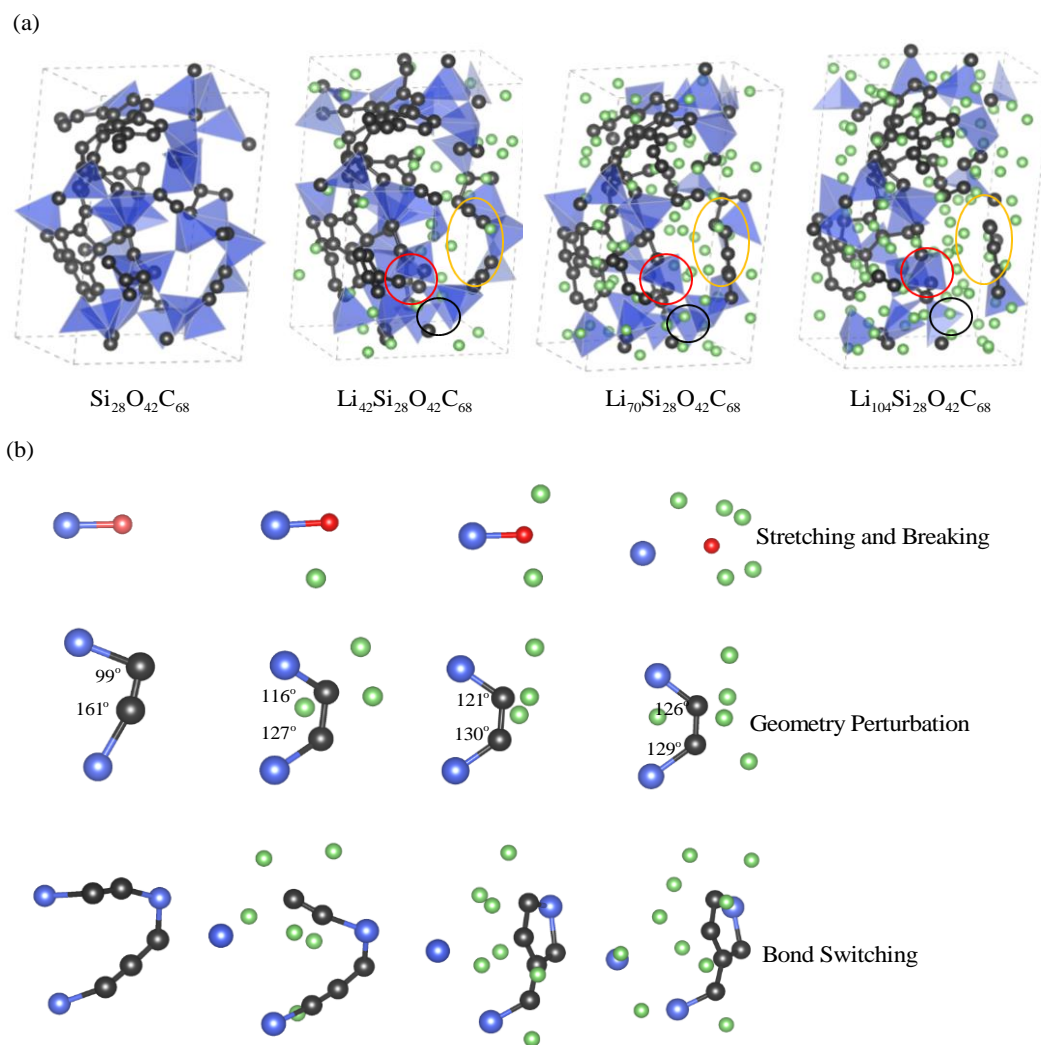


Figure 3.4. (a) The evolution of atomic configurations of SiOC during lithiation. The backbone of segregated C phase stabilizes the structure. The cell volume changes up to 22% after full lithiation. (b) Local structural rearrangement in the atomic configurations in (a) includes stretching and breaking of Si-O bonds, geometry perturbation of Si-C-C-Si clusters, and bond switching in C rings. The purple, red, gray, and green spheres represent the Si, O, C, and Li atoms, respectively.

We now focus on the second lithiation stage and examine the complex and concurrent microscopic events associated with Li reactions. Figure 3.4 (a) shows four representative configurations in the course of lithiation,  $\text{Si}_{28}\text{O}_{42}\text{C}_{68}$ ,  $\text{Li}_{42}\text{Si}_{28}\text{O}_{42}\text{C}_{68}$ ,  $\text{Li}_{70}\text{Si}_{28}\text{O}_{42}\text{C}_{68}$ , and  $\text{Li}_{104}\text{Si}_{28}\text{O}_{42}\text{C}_{68}$ , respectively. It is clearly seen that the segregated C interface remains intact in the lithiation process. The overall structure retains the integrity with little change in shape and a volumetric expansion of 22% after full lithiation. Meanwhile, the Si-O-C tetrahedral units gradually vanish which decreases the connectivity of the glass network and results in a possible

open structure to accommodate further Li. Figure 3.4 (b) shows the evolution of three local configurations representing the typical events in the respective configurations in Figure 3.4 (a). The Si-O bond is stretched and eventually broken with more Li attracted by O. For the C phase, Li is attracted by the unsaturated C atoms of dangling bonds in the Si-O-C network as well as by the topological defects at the edge of or within the graphene-like segregated network. The absorption of Li by C is mediated by the geometric perturbation and bond switching. In Figure 3.4 (b), we show that the Si-C-C-Si clusters with unsaturated C atoms alter their geometry due to the electrostatic interactions induced by the surrounding Li. Specifically, the bond angles of Si-C-C-Si changes from  $99^\circ$ ,  $161^\circ$  to  $126^\circ$ ,  $129^\circ$ , respectively, indicating that the centered unsaturated C optimize toward the  $sp^2$  type which has a planar symmetry of a characteristic angle of  $120^\circ$ . The molecular orbitals of the Si-C-C-Si cluster, to be discussed in Figure 3.6, will provide further understanding on the geometry changes. The third case in Figure 3.4 (b) shows the Si-C bond breaking and the C-C bond reforming which result in the formation of the five-membered ring including one Si and four C atoms.

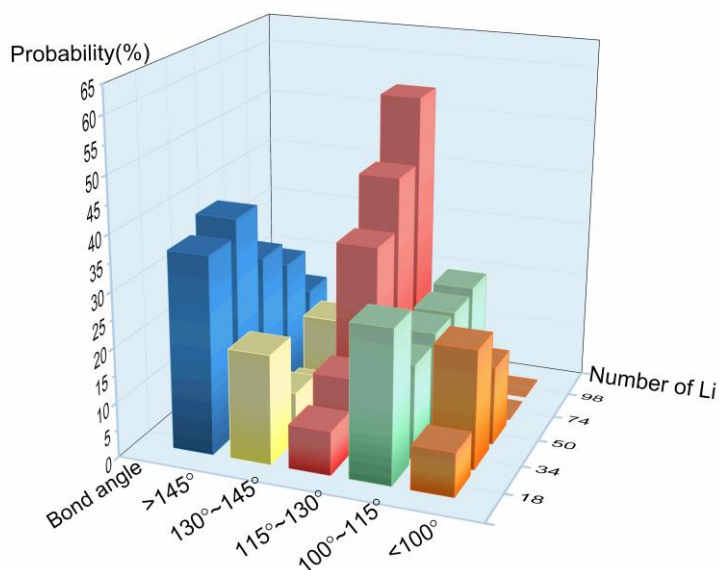


Figure 3.5. The bond angle distribution of C-C-C, Si-C-C, and Si-C-Si clusters in five representative  $\text{Li}_x\text{SiOC}$  compositions. The salient features are that the probability of bond angles larger than  $145^\circ$  steadily decreases while the distribution of bond angles between  $115^\circ$  and  $130^\circ$  increases significantly upon lithiation. This demonstrates the geometry optimization of C atoms toward the  $sp^2$  type coordinated by Li insertion.

In fact, the  $sp^2$  optimization of C through geometry relaxation is a common phenomenon facilitated by Li insertion. In pristine SiOC, many C atoms are unsaturated with one or more dangling bonds near the edge of the C network or in the Si-O-C network. We calculate the bond angle of C-C-C, Si-C-C, and Si-C-Si clusters in five different  $Li_xSiOC$  compositions. All the clusters share the feature that the centered C atoms coordinated to neighboring Si or C have one dangling bond compared with the stable  $sp^2$  configuration. The evolution of the bond angle distributions in the five representative configurations is shown in Figure 3.5. Two characteristics of the bond angle distribution are that the bond angles larger than  $145^\circ$  steadily decreases while the probability of bond angles between  $115^\circ$  and  $130^\circ$  significantly increases upon lithiation. This confirms the geometry optimization of C toward the  $sp^2$ -type configuration initiated by the imperfections of C atoms and coordinated by Li insertion. We may understand such a behavior from the hybridized molecular orbitals. At the ground state, a C atom containing six electrons has the electron configuration of  $1s^2 2s^2 2p^2$ . Two unpaired electrons occupy the outer shell, namely,  $p_y$  and  $p_z$ <sup>32, 33</sup>. Figure 3.6 shows the evolution of two molecular orbitals mostly contributed by two centered C atoms. Before lithiation, the  $p_y$  orbital of two C atoms with the same orientation overlap with each other to form one  $\pi$  type molecular orbital (MO)<sup>34</sup>,  $\pi_y$ , Figure 3.6 (a). Similarly, two  $p_z$  orbitals overlap to form the  $\pi_z$  MO (Figure 3.6 (b)). For C, one electron can be readily excited from  $2s$  into the  $2p$  state given a small energy difference between the two states<sup>35</sup>. In the presence of an external perturbation, such as a nearby hydrogen, the energy difference can be easily overcome and result in the hybrid state of  $sp$ -orbital<sup>36</sup>. As shown in Figure 3.6 (c), the overlapped  $\pi_y$  is perturbed by the virtual orbital of nearby Li atoms (not shown in the MO diagram) and is split into two atomic orbitals of different orientations, which drives the formation of a hybrid  $sp^2$  orbital. The  $sp^2$  hybridization has the planar symmetry with a characteristic angle of  $120^\circ$  between each hybrid orbital of C atoms which is consistent with the result of Figure 3.5. This helps to understand the geometry changes of the C centered Si-C clusters when Li inserts. Figure 3.6 (b) and (d) show the  $\pi_z$  MO of C atoms before and after lithiation. There is no clear difference between the molecular orbital shapes for  $\pi_z$  in the two figures. It shows that the  $p_z$  orbital of C atoms are unperturbed by the surrounding Li and remain perpendicular to the  $sp^2$ -hybrid planar orbitals.

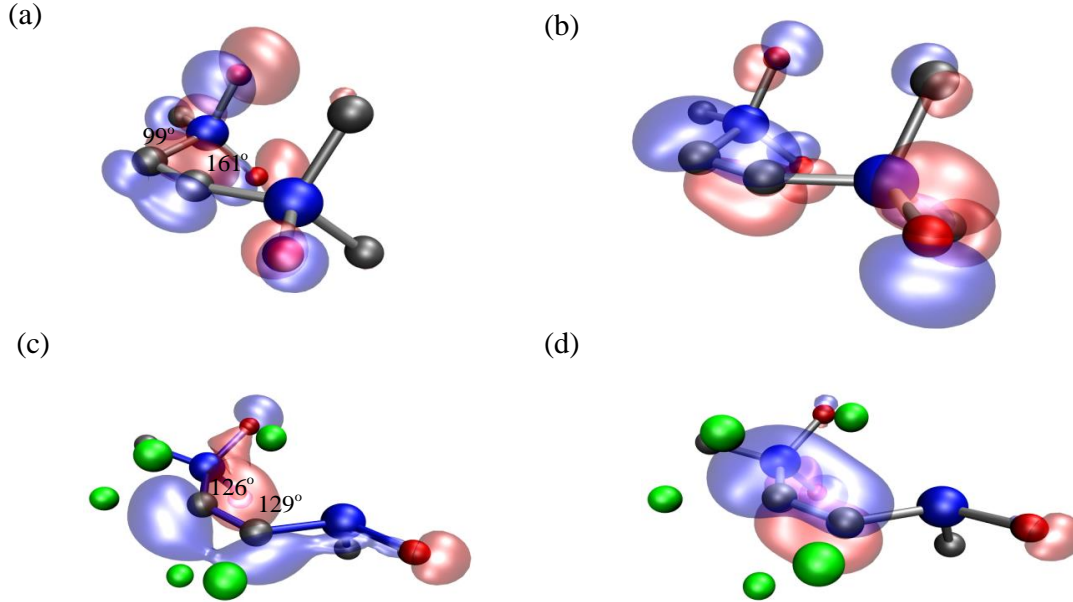


Figure 3.6. The evolution of two molecular orbitals contributed by two centered C atoms in a Si-C-C-Si cluster. (a) Before lithiation, the  $p_y$  orbitals of the two C atoms overlap to form one  $\pi$  type molecular orbital,  $\pi_y$ . (b) Similarly, two  $p_z$  atomic orbitals overlap to form the  $\pi_z$  orbital. (c) After lithiation, the original  $\pi_y$  orbital is perturbed by the virtual orbital of the nearby Li atoms (not shown in the diagram) and is split into two atomic orbitals in different orientations, which promotes the formation of the hybrid  $sp^2$  orbital. (d) In comparison, there is no obvious difference in  $\pi_z$  which remains perpendicular to the  $sp^2$ -hybrid planar orbital before and after lithiation.

### 3.1.3.3 Electron Transfer between Lithium and Si-based Glass Ceramics

We further examine in detail the charge transfer from Li to the host Si-O-C molecule. We analyze the map of electron density difference in various local regions. In Figure 3.7, from left to right, it shows the charge transfer in the segregated C interface, Si-O-C mixed regime, and amorphous silica domain before and after Li addition, respectively. The results are obtained by subtracting the charge density of pristine SiOC and pure Li from that of lithiated SiOC. All the atomic positions are assumed to remain unchanged upon lithiation. In the graphene-like C network, charge transfer mainly takes place at the imperfection sites such as the five or seven-membered C rings or at the edge of C atoms, which agrees with the previous experimental report<sup>14</sup>. Little chemical bonding of Li with the saturated  $sp^2$ -type C atoms is formed in the interior of the segregated C network. This again confirms the backbone function of the C interface and the resulting small deformation of the SiOC molecule in the lithiation process. In the mixed Si-O-C regime, the bonding environment is rather complicated. From the plot we learn that the charge transfer mainly occurs around the O atoms and the unsaturated C atoms. In the

SiO<sub>4</sub> tetrahedral units away from the C interface, a major fraction of electron density is accumulated at the O atoms possibly because of the local screening effect of O<sup>37</sup>. The distribution map of the electron density difference confirms that the major interaction occurs between Li with O and unsaturated C atoms in SiOC. These chemical interactions induce the breaking of Si-O bonds and geometry perturbation of Si-C clusters.

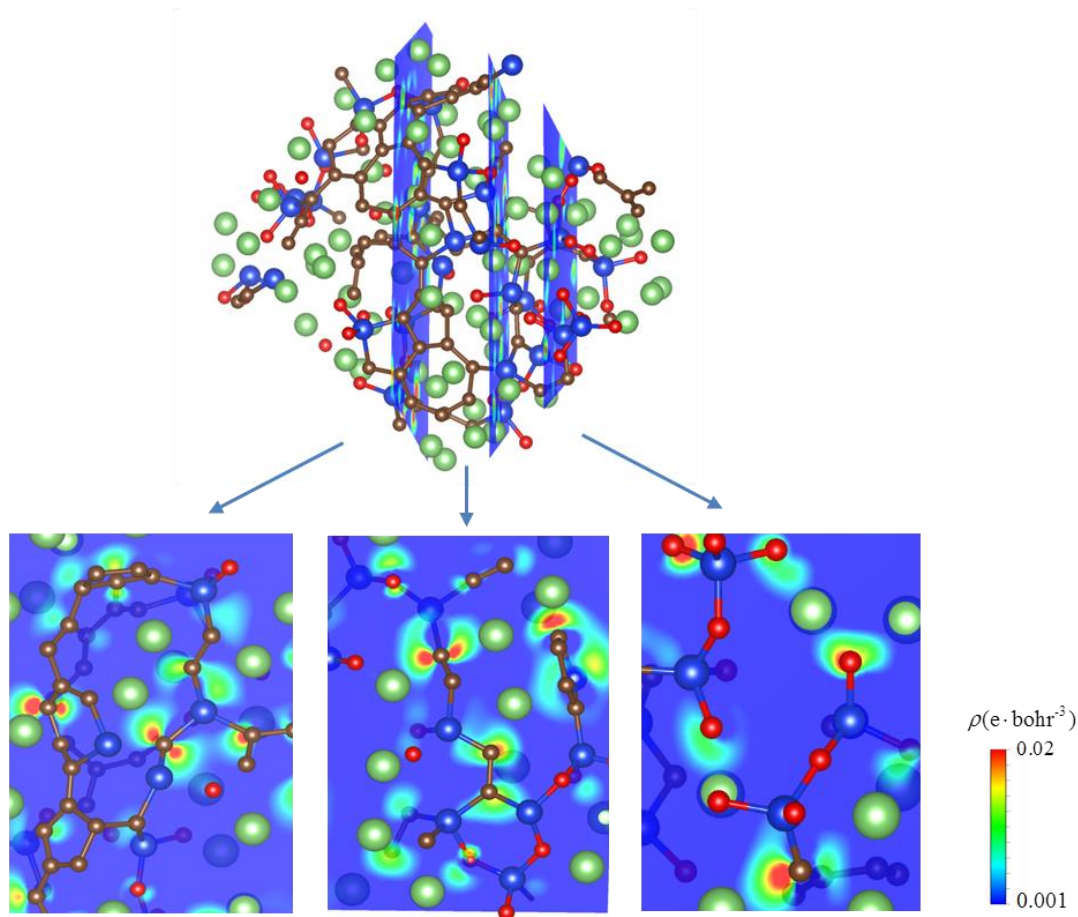


Figure 3.7. The map of charge density difference in different regions of Li<sub>66</sub>Si<sub>28</sub>O<sub>42</sub>C<sub>68</sub>. From left to right, it shows the charge density difference of the segregated C interface, the Si-O-C mixed regime, and the amorphous silica domain before and after Li insertion, respectively. In the graphene-like C phase, charge transfer takes place at the imperfection sites such as the five or seven C rings or the edge of C atoms. The saturated *sp*<sup>2</sup> C atoms remain inactive and serve as the stable backbone to maintain the structure. In the mixed Si-O-C regime, charge transfer mainly occurs around the O atoms and unsaturated C atoms. For the SiO<sub>4</sub> tetrahedral units in the silica domain, positive charge is accumulated around the O atoms.

The electron transfer also infers the electrical conductivity of the Si-based glass ceramics. One drawback of certain SiOC molecules is the electrically insulating nature which results in the poor charge transfer and voltage hysteresis in batteries. Doping and compositing with conductive agents are effective strategies to enhance the electrical conductivity of SiOC<sup>38-40</sup>. Here we plot

the electron density of states (DOS) of  $\text{Li}_x\text{SiOC}$  to show the remarkable improvement of electrical conductivity of SiOC induced by Li dopant. Figure 3.8 (a-d) show the DOS of pristine SiOC,  $\text{Li}_2\text{Si}_{28}\text{O}_{42}\text{C}_{68}$ ,  $\text{Li}_4\text{Si}_{28}\text{O}_{42}\text{C}_{68}$ , and  $\text{Li}_6\text{Si}_{28}\text{O}_{42}\text{C}_{68}$ , respectively. The Fermi energies have been shifted to zero of the energy scale. The DOS of pristine SiOC has a clear insulator character

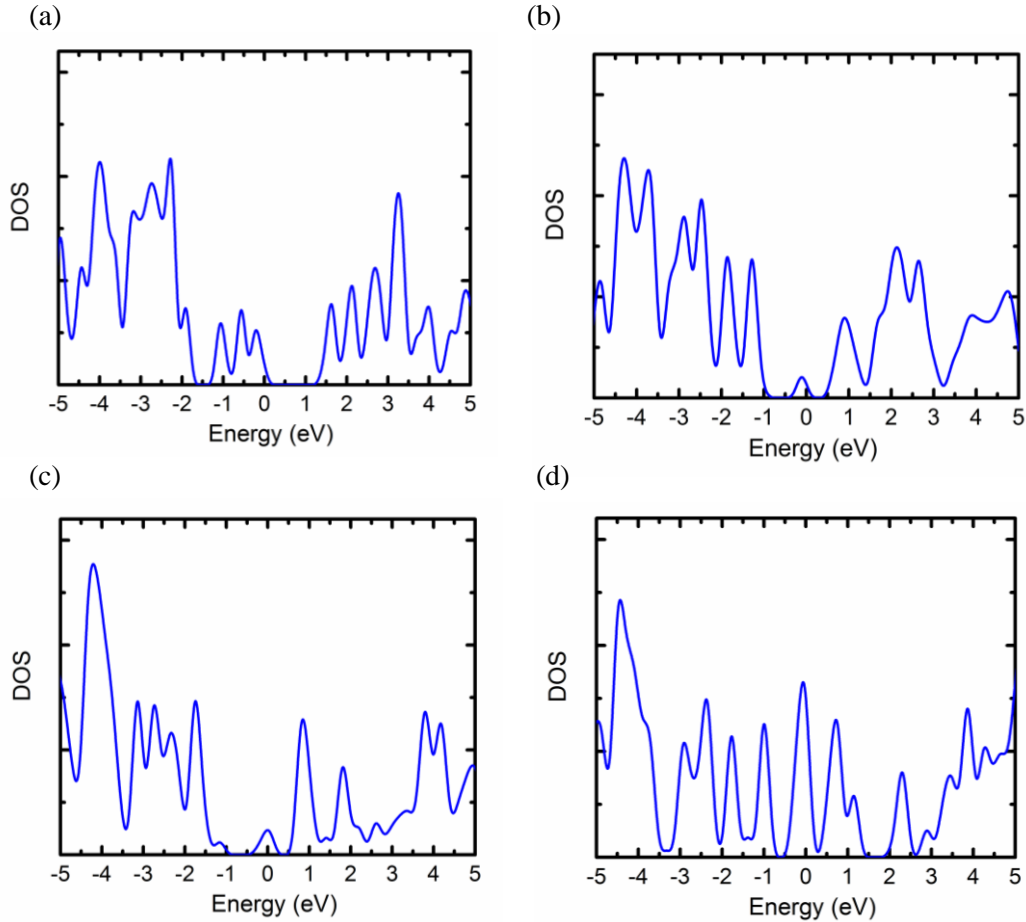


Figure 3.8. The density of states (DOS) of (a) pristine SiOC, (b)  $\text{Li}_2\text{Si}_{28}\text{O}_{42}\text{C}_{68}$ , (c)  $\text{Li}_4\text{Si}_{28}\text{O}_{42}\text{C}_{68}$ , and (d)  $\text{Li}_6\text{Si}_{28}\text{O}_{42}\text{C}_{68}$ , respectively. The DOS of pristine SiOC has an insulator character with a band gap of 1.3 eV. During initial lithiation, the electron transfer from Li to O and defective C atoms induces electron states near the Fermi level. The band gap is significantly reduced by the insertion of four Li atoms. Up to six Li, the band gap vanishes which indicates that the electronic conductivity of SiOC molecule can be enhanced by the dopant Li.

with a band gap of ca.1.3 eV. However, the gap between the valence and conduction bands is much smaller compared with pure silica glass<sup>21</sup> because of the electron states around the Fermi level induced by the excess C in  $\text{SiOC}^{41}$ . With the addition of Li, the electron states of Li are transferred to the low-energy unoccupied valence regimes brought by the chemical bonding of Li with unsaturated C atoms. The band gap is dramatically reduced by the insertion of four Li atoms. Up to six Li,  $\text{Li}_6\text{Si}_{28}\text{O}_{42}\text{C}_{68}$  shows the conductor character without the band gap. This confirms

that the electrical conductivity of SiOC can be largely enhanced by the doping elements such as Li and B<sup>38, 39</sup> partially because of the presence of the excess C atoms.

## 3.2 First-principles Studies on the Electrochemical and Mechanical Behaviors of $\alpha$ -MoO<sub>3</sub> in Li-ion Batteries

### 3.2.1 Background and Motivation

Li-ion batteries are the state-of-the-art choice in portable electronics, electric vehicles, and electric energy storage system<sup>42,43</sup>. Technological improvement in rechargeable batteries has been driven by the ever-increasing demand on electrodes of high energy density and superior electrochemical and mechanical stabilities<sup>44</sup>. As an alternative to graphite, metal oxides hold the great promise of high-capacity anodes given the wealth of compounds of various degrees of covalence and metal oxidation states that enable the tuning of equilibrium potential and charging kinetics for Li-ion batteries<sup>45,46</sup>.

Lithiation of metal oxides proceeds with the co-absorption of Li ions and electrons. The metal ions serve as the redox center for the electron injection. The Li storage in the host metal oxides is under two typical mechanisms: insertion and conversion. The respective lithiation mechanism shows a rough correlation with the atomic number of the 3*d* transition metal oxides<sup>47</sup>. This feature was understood based on the thermodynamic driving force of lithiation reaction and the kinetic factor of M-O bond dissociation. For the early transition metal oxides, the equilibrium potential vs. Li/Li<sup>+</sup> of conversion reaction is low. Meanwhile, the metal ions are more polarized and the dissociation energy of M-O bonds is stronger in the early transition metal oxides than that of the later compounds. Therefore, conversion reaction is generally more favorable for the later transition metal oxides. For the insertion-type oxides, such as TiO<sub>2</sub> and V<sub>2</sub>O<sub>5</sub><sup>47-50</sup>, Li is absorbed at well-defined interstitial sites in the form of one-dimensional channels and two-dimensional van der Waals layers in crystalline structures or at structural defects populated in amorphous lattice. The capacity of insertion-type metal oxides is limited by the available sites for Li occupation. Nevertheless, one noticeable merit is that Li insertion and extraction do not significantly distort the host structure and thus the mechanical stability can be retained in the long-term cycles. For the conversion-type materials, such as Co<sub>3</sub>O<sub>4</sub>, CuO, Fe-IO<sub>3</sub>, and NiO<sup>50-56</sup>, the injection of Li ions and electrons translates the metal oxides into the elemental metal and lithium oxides through the following reaction:  $M_aO_b + (b \cdot n)Li \leftrightarrow aM + bLi_nO$ . In general, the

conversion-type metal oxides preserve higher capacity (typical theoretical capacity  $\sim 1000 \text{ mAh g}^{-1}$ ) than the insertion-type materials. However, the long-term cyclability may be compromised by the mechanical instability and structural disintegration induced by repetitive large volumetric change during lithiation cycles. Among the binary metal oxides,  $\text{MoO}_3$  exhibits high theoretical capacity ( $1117 \text{ mAh g}^{-1}$ ) despite its relatively high formula weight. The capacity surpasses the values of most of transition metal oxides. The orthorhombic  $\text{MoO}_3$  ( $\alpha\text{-MoO}_3$ ), composed of layers of distorted  $\text{MoO}_6$  octahedra, is the thermodynamically stable phase among various polymorphs, and is of general interest in electrochemical applications given its intrinsic layered crystalline structure and the ease of multivalent-state ( $\text{Mo(VI)/Mo(V)}$ ) coupling. This work aims to illustrate the Li reaction mechanism of  $\alpha\text{-MoO}_3$  that is distinct from the typical insertion/conversion behaviors in binary metal oxides. Furthermore, in comparison to most metal oxides that the high capacity is largely offset by the mechanical degradation<sup>57-59</sup>,  $\text{MoO}_3$  remains defects free in the lithiation cycles in spite of 90% volumetric change associated with the electrochemical processes.

### 3.2.2 Simulation Methods

We perform first-principles theoretical studies to attain full understanding of the microscopic mechanism of lithiation in  $\alpha\text{-MoO}_3$ . Projector-augmented-wave (PAW) potentials in Vienna Ab-initio Simulation Package (VASP) are used to mimic the ionic cores, while the generalized gradient approximation (GGA) in the Perdew-Burke-Ernzerh (PBE) flavor is employed for the exchange and correlation functional<sup>18,19</sup>. The Hubbard U-J parameter 6.3 for Mo is adopted to model the large Coulombic repulsion between localized electrons<sup>60</sup>. The atomic structures and system energy are calculated with an energy cutoff of 520 eV. For Brillouin zone sampling, a  $5 \times 3 \times 5$  mesh of  $k$  points in the Monkhorst-Pack scheme is sufficient in the energetic relaxation of  $\text{Li}_x\text{MoO}_3$ . The energy optimization is considered complete when the magnitude of the force on each atom is smaller than  $0.02 \text{ eV \AA}^{-1}$ . In addition, the DFT-D2 method is used with a global scaling factor of 0.75 for correction of the van der Waals interaction between interlayers in  $\alpha\text{-MoO}_3$ <sup>61</sup>. The unit cell of  $\alpha\text{-MoO}_3$  has the space group of  $Pbnm$  and contains 16 atoms. The lattice parameters for the unit cell are  $a=3.83 \text{ \AA}$ ,  $b=13.89 \text{ \AA}$ , and  $c=3.73 \text{ \AA}$ , which are very close to the experimental values<sup>62</sup>.

We incrementally increase Li concentration to model the lithiation process. We consider five possible configurations of  $\text{Li}_x\text{MoO}_3$  at a given Li concentration with different Li distributions in each, to eliminate the large variations inherent to the small model size. At each Li concentration, we perform the Delaunay triangulation analysis to identify the possible favorable sites for Li insertion<sup>63</sup>. The formation energy per Li is defined as  $E_f(n) = [E_{n\text{Li-MoO}_3} - E_{\text{MoO}_3} - nE_{\text{Li}}]/n$ . Here the energy of  $\text{MoO}_3$  ( $E_{\text{MoO}_3}$ ) and the energy of a Li atom in its bulk form ( $E_{\text{Li}}$ ) are taken as the reference energies and  $E_{n\text{Li-MoO}_3}$  is the total energy of the system containing  $n$  Li atoms in the cell.

### 3.2.3 Results and Discussion

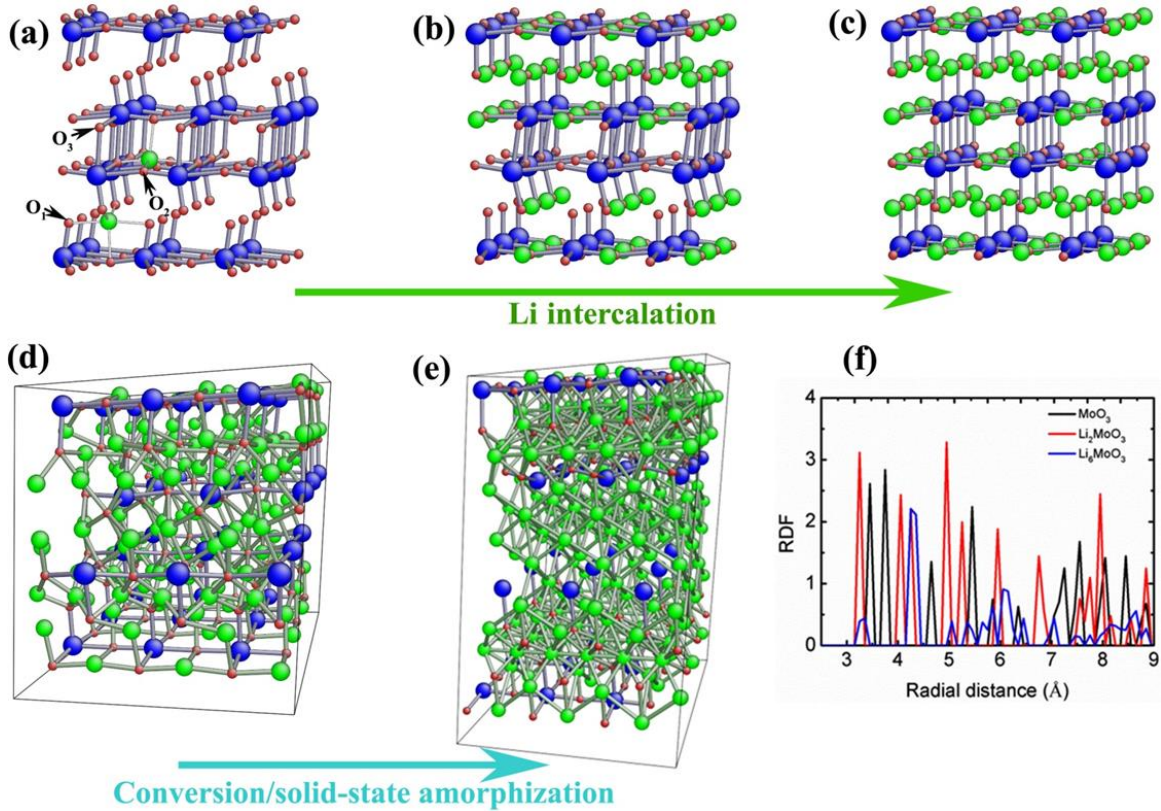


Figure 3.9. First-principles modeling on the two-step lithiation of  $\alpha\text{-MoO}_3$ . (a) The interlayer and intralayer sites are the two favorable interstitial positions for Li intercalation in  $\alpha\text{-MoO}_3$ . (b, c) Li occupies the favorable interstitial sites which induces the formation of crystalline  $\text{Li}_2\text{MoO}_3$ . (d, e) The conversion reaction causes solid-state amorphization of the structure. (f) RDF plot of the Mo-Mo pairs in  $\text{MoO}_3$ ,  $\text{Li}_2\text{MoO}_3$  and  $\text{Li}_6\text{MoO}_3$ . The compositions in (b)-(e) are  $\text{Li}_{1.5}\text{MoO}_3$ ,  $\text{Li}_2\text{MoO}_3$ ,  $\text{Li}_{3.75}\text{MoO}_3$ , and  $\text{Li}_6\text{MoO}_3$ , respectively. The atomic configurations are expanded views consisting of  $3 \times 1 \times 3$  unit cells. The blue, red, and green spheres represent Mo, O, and Li atoms.

We first examine the energetics and structural features during Li insertion into  $\alpha\text{-MoO}_3$ . We incrementally increase Li concentration to model the lithiation process. We consider five

possible configurations of  $\text{Li}_x\text{MoO}_3$  at a given Li concentration with different Li distributions in each, to eliminate the large variations inherent to the small model size. At each Li concentration, we perform the Delaunay triangulation analysis to identify the possible favorite sites for Li insertion<sup>64</sup>. The formation energy per Li is defined as  $E_f(n) = [E_{n\text{Li-MoO}_3} - E_{\text{MoO}_3} - nE_{\text{Li}}]/n$ . Here the energy of  $\text{MoO}_3$  ( $E_{\text{MoO}_3}$ ) and the energy of a Li atom in its bulk form ( $E_{\text{Li}}$ ) are taken as the reference energies and  $E_{n\text{Li-MoO}_3}$  is the total energy of the system containing  $n$  Li atoms in the cell. We identify two favorable interstitial positions (Figure 3.9 a) for Li intercalation – the interlayer and intralayer sites with formation energy of -3.57 eV and -3.68 eV, respectively. The interlayer site is surrounded by four terminal O1 atoms and one O2 atom in the adjacent layer, while the intralayer site is neighbored with two O2 atoms and two O3 atoms<sup>65</sup>. The energy barrier of Li diffusion along the interlayer-intralayer pathway is calculated as 0.55 eV (Figure 3.10) that is consistent with the previous study<sup>66</sup>. The unit cell contains a total number of 8 interlayer and intralayer sites for Li intercalation. Those interstitial spots are filled by Li at the early stage of lithiation. Additional Li are placed at the sites of largest Delaunay triangular volume which are regarded as generally favorable sites for Li insertion. In each step, 1 Li is added into the lattice to model the composition range  $0.25 \leq x \leq 6$  in  $\text{Li}_x\text{MoO}_3$ . Figure 3.9b-e show the geometry at four representative Li concentrations,  $\text{Li}_{1.5}\text{MoO}_3$ ,  $\text{Li}_2\text{MoO}_3$ ,  $\text{Li}_{3.75}\text{MoO}_3$ , and  $\text{Li}_6\text{MoO}_3$ , respectively. The layered structure is well maintained up to the composition  $\text{Li}_2\text{MoO}_3$ . Beyond this point, Li insertion breaks the Mo-O bonds and induces solid-state amorphization of the structure. The radial distribution function (RDF) is plotted (Figure 3.9f) for the pristine  $\text{MoO}_3$ ,  $\text{Li}_2\text{MoO}_3$ , and fully lithiated state  $\text{Li}_6\text{MoO}_3$  to show the transition from the layered crystalline structure to the eventual amorphous state.

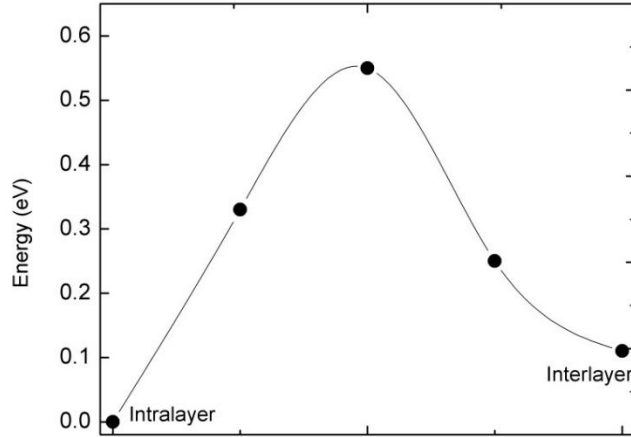


Figure 3.10. Diffusion barrier of a single Li from the interlayer to the intralayer site calculated by the nudged elastic band (NEB) method.

Figure 3.11a shows the evolution of the formation energy and strains as a function of the Li concentration. The solid symbols represent the average values from the five different configurations for each given composition, and error bars represent the standard deviation. The variation of formation energy clearly demonstrates the two-stage lithiation mechanism. Up to the composition  $\text{Li}_2\text{MoO}_3$ , the formation energy remains a nearly constant value of  $-3.6$  eV. Li intercalation at the interlayer and intralayer sites is highly favorable with a large thermodynamic driving force. In the next stage from  $\text{Li}_2\text{MoO}_3$  to  $\text{Li}_6\text{MoO}_3$ , the formation energy decreases rapidly (more positive) as the Li concentration increases due to the saturation of the intercalation sites and growing repulsion between the neighboring Li atoms. Such a behavior is also seen in the plot of evolution of volumetric strains in Figure 3.11b. As expected, the intercalation process is accompanied with minor volumetric deformation and the crystalline structure is well retained. The volumetric strain increases dramatically afterwards and reaches  $\sim 90\%$  upon complete lithiation. The large volumetric deformation is accommodated by the gradual rearrangement of the lattice structure through Mo-O bond breaking and Li-Mo-O cluster reforming as shown in Figure 3.10. It is also worth noting that the deformation of  $\text{MoO}_3$  during lithiation is anisotropic. The in-plane strain ( $\epsilon_x$ ) along the  $a$ -axis and out-of-plane strain along the  $b$ -axis ( $\epsilon_y$ ) are included in Figure 3.11b. The deformation in the in-plane directions is relatively small. The decrease of lattice length in the  $b$ -axis (negative  $\epsilon_y$ ) in the intercalation process is due to the attraction between the oxygen layers with Li. The evolution of the formation energy and strains in the

modeling agree well with the TEM experimental observations on the kinetics and deformation of  $\alpha$ - $\text{MoO}_3$  during lithiation.

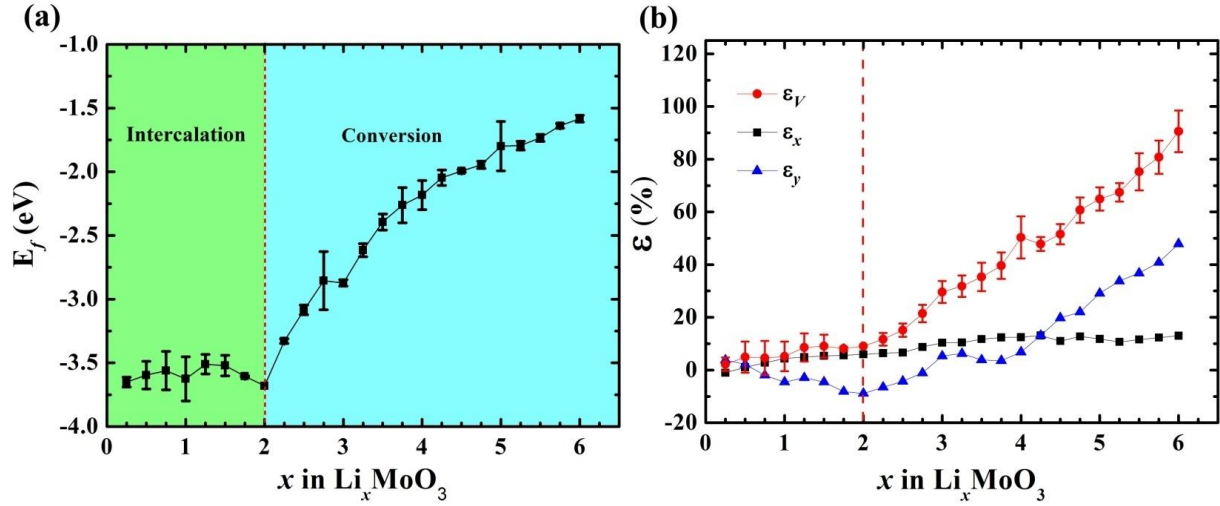


Figure 3.11. The two-step lithiation of  $\text{MoO}_3$  evident in (a) the formation energy per Li in  $\text{Li}_x\text{MoO}_3$  and (b) strains in the in-plan ( $\epsilon_x$ ) direction, out-of-plan ( $\epsilon_y$ ) direction, and the total volumetric strain ( $\epsilon_V$ ). The solid symbols represent the average values of the formation energy per Li or strains from five different configurations of  $\text{Li}_x\text{MoO}_3$ , and error bars represents the standard deviation.

### 3.3 Evolution of Mechanical Properties of $\text{LiNi}_x\text{Mn}_y\text{Co}_z\text{O}_2$ Cathode during Delithiation

#### 3.3.1 Background

$\text{LiNi}_x\text{Mn}_y\text{Co}_z\text{O}_2$  ( $x+y+z=1$ ) is among the best cathode materials for the electrification of automobile vehicles given its advantages in high capacity, electrochemical stability, and cost effectiveness.<sup>67-70</sup> NMC is formed by partially replacing Co in  $\text{LiCoO}_2$  by Ni and Mn to achieve the improved electrochemical performance while reducing the material cost. The composition of Ni, Mn, and Co can be largely tuned to optimize the capacity, rate performance, structural stability, and cost of Li-ion batteries.<sup>37,71</sup>

The structural stability is a key factor plaguing the cyclic performance of NMC materials.<sup>4,72-75</sup> Recent experiments have shown that the class of NMC, albeit of only  $\sim 5\%$  volumetric change upon lithiation, suffers from heavy structural disintegration and mechanical failure after a number of cycles which significantly increase the ionic and electric impedance of batteries.<sup>76-79</sup> The mechanical properties largely depend on the lithiation state, albeit the layered crystal lattice is maintained during Li insertion and extraction, and further degrade as the electrochemical cycles proceed. We conduct first-principles modeling to understand the variation of the elastic

property of NMC at different states of charge. The theoretical results are in good agreement with the experimental measurements. The quantitative results of the mechanical properties of NMC help understanding of the chemomechanical behavior of NMC materials and will aid the design of composite electrodes of enhanced mechanical and structural stability.

### 3.3.2 Simulation Methods

Vienna Ab-initio Simulation Package (VASP)<sup>18,19</sup> is adopted to build the supercell model and simulate the mechanical properties. The NMC supercell is constructed with the  $R3m$  space group, where Li, O and TM occupy the  $3b$ ,  $6c$ , and  $3a$  sites, respectively. 120 atoms are contained in fully lithiated NMC. The successive delithiated NMC models are constructed by randomly removing a certain number of Li from the  $\text{LiNi}_{0.5}\text{Mn}_{0.3}\text{Co}_{0.2}\text{O}_2$  lattice. All NMC models are fully relaxed to achieve the optimized configurations. Projector-augmented wave (PAW) potentials are used to mimic the ionic cores, while the generalized gradient approximation (GGA) in the Perdew–Burke–Ernzerhof (PBE) flavor is employed for the exchange and correlation functional. To model the Coulombic repulsion between localized electrons in transition metals (TMs), the DFT + U method is adopted. The Hubbard U – J values for Ni, Mn, and Co are set as 6.7, 4.2, and 4.91, respectively.<sup>80</sup> The plane-wave set is expanded within an energy cutoff of 520 eV. The  $2 \times 1 \times 1$  mesh of  $k$  points in the Monkhorst–Pack scheme is chosen for the Brillouin zone sampling. Energy optimization is considered complete when the magnitude of force per atom is smaller than 0.04 eV/Å. In the supercell model, we apply uniaxial tension in the  $x$ ,  $y$ , and  $z$  directions and take the average Young’s modulus from the three stress–strain curves.

### 3.3.3 Results and Discussion

We investigate the evolution of the elastic property of NMC using first-principles theoretical modeling. The electronic structure, Jahn-Teller (JT) structural stability, and atomic bond strength of NMC are analyzed.

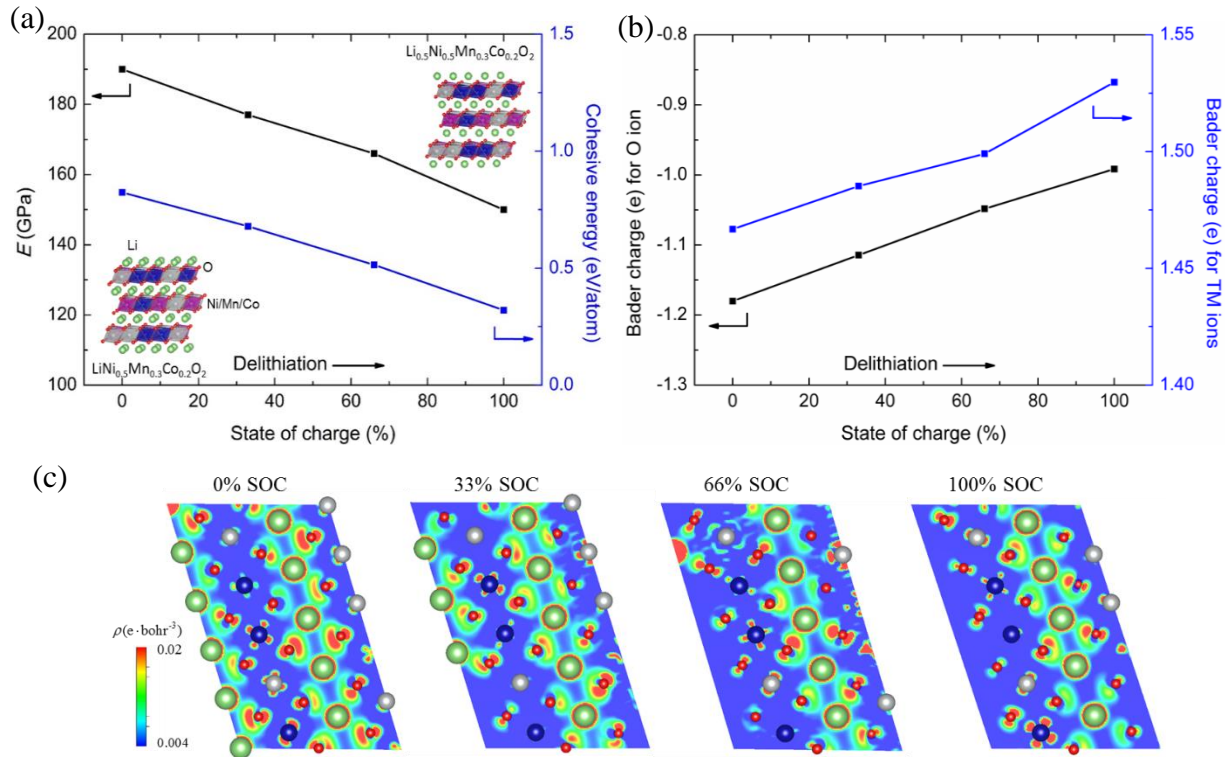


Figure 3.12. First-principles results on (a) the Young's modulus and cohesive energies, (b) the Bader charge of O and transition metal ions, and (c) the map of electron density difference in NMC at different states of charge.

Figure 3.12a shows the elastic modulus and the cohesive energy as a function of the state of charge, again 0% represents the pristine NMC, 100% represents  $\text{Li}_{0.5}\text{Ni}_x\text{Mn}_y\text{Co}_z\text{O}_2$ , and the inset figures show the layered atomic configurations. During delithiation, the Young's modulus of NMC linearly decreases which qualitatively agrees with the experimental result. The quantitative discrepancy originates from the interfacial structure of NMC particles as discussed earlier. Cohesive energy is defined as the energy to break the lattice into isolated free atoms, which represents the strength of atomic bonding and correlates with the elastic property of materials. The cohesive energy shows the similar linearly decreasing trend when Li is extracted. The reduction of the elastic strength of NMC during delithiation is attributed to (I) the Jahn-Teller distortion, (II) the decrease of electrostatic interaction between Li-O, and (III) the reduction of the TM-O polarization. We will discuss each aspect in detail as follows.

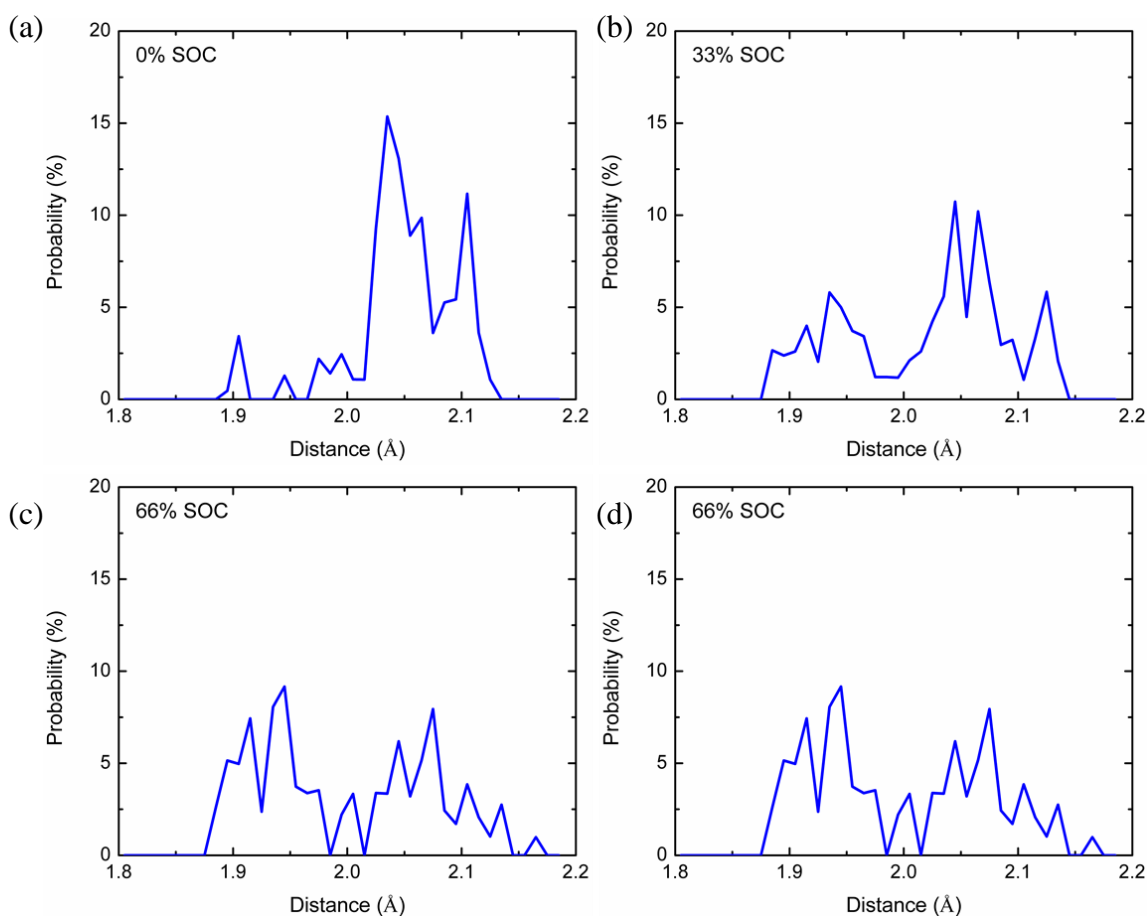


Figure 3.13. The Ni-O bond length distribution in NMC at different states of charge. During delithiation, the Ni-O bond length decreases implying the transition from  $\text{Ni}^{2+}$  into  $\text{Ni}^{3+}$ .

The Jahn-Teller distortion destabilizes the crystal lattice and reduces the mechanical strength. When Li is extracted, a fraction of Ni changes the valence state from the inactive JT species  $\text{Ni}^{2+}$  to the active JT ion  $\text{Ni}^{3+}$ , which distorts the octahedral TM-O complex. The probability distribution of Ni-O bond length in Figure 3.13 and the variation of Bader charge of Ni in Figure 3.14 both reveal the transition of the oxidation state of Ni. In addition, the increasing fraction of Li vacancy reduces the electrostatic interactions between the Li and the neighboring O layers, resulting in a larger and uneven Li slab distance. Figure 3.15 shows the increase of the average Li-O bond length and the  $c$ -axis lattice parameter during delithiation which indicates the weak electrostatic interactions of Li-O and enhanced repulsion between adjacent anionic O layers induced by Li vacancies. More importantly, the covalent TM-O bonds largely determine the elastic property of NMC. We discussed the detailed TM-O interactions in NMC in an earlier publication.<sup>37</sup> To help our understanding we quote the following brief description. According to

the ligand field theory, the interaction between TMs and the ligand (O) is mainly  $\sigma$ -bonding with small contribution of  $\pi$ -bonding in the TM–O octahedral complex. Figure 3.16 shows an example molecular orbital diagram of the TM complex with the 3d orbital electron population of

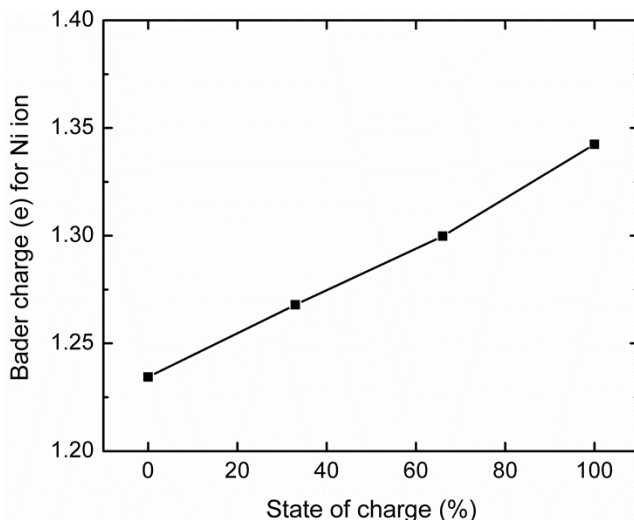


Figure 3.14. The gradual increase of Bader charge of Ni during delithiation.

$\text{Co}^{3+}$  and O 2p orbital. The three degenerated  $t2g$  orbitals of transition metals,  $d_{xy}$ ,  $d_{xz}$ , and  $d_{yz}$ , contribute to both the nonbonding and antibonding states. The  $eg$  level has a large overlap in the energy scale with the O 2p orbital and constitutes the covalent bonding orbital with a large coefficient for the ligand orbital. The  $eg^*$  level is mainly of transition metal  $d$  character resulting in the strong anti-bonding interactions. Figure 3.12b plots the Bader charges of O and TM ions as a function of SOC. When Li intercalates into the NMC lattice (smaller value of SOC), the O Bader charge linearly increases (more negative) while the average TMs Bader charge gradually decreases (less positive). Figure 3.12c shows the electron transfer between Li and the NMC host. The results are obtained by subtracting the charge density of pristine NMC from that of lithiated NMC. All the atomic positions are assumed to remain unchanged upon Li insertion. The red color represents more electron accumulation. It is clearly seen that Li is completely ionized and gives away nearly all of its valence electrons. The charge transfer mainly concentrates on the 2p orbitals of neighboring O ions, as the large red electron cloud is formed nearby the O ions. A small fraction of electrons from Li transfers toward the  $d$  orbital ( $t2g$  or  $eg^*$ ) of TM ions. The major charge accumulation around O is because of the local electron screening of O ions.<sup>81</sup> The large increase of electron density of O 2p orbital makes the  $\sigma$ -bonding of  $eg$  orbital in TMs with

the  $2p$  orbital of O more polarized and the NMC lattice more ionic in nature. When Li is extracted from the lattice, the TMs-O interactions reduce the polarity and decrease the ionic valence bonding and mechanical strength and NMC.

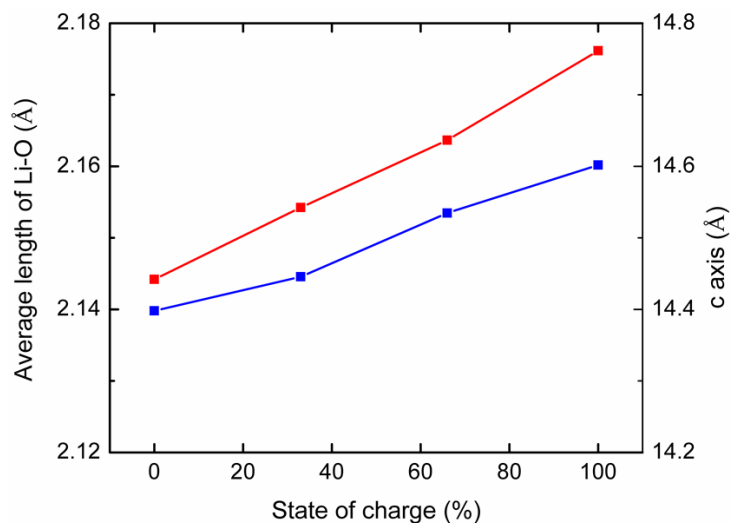


Figure 3.15. The gradual increase of Li-O bond length and  $c$ -axis lattice parameter during delithiation of NMC.

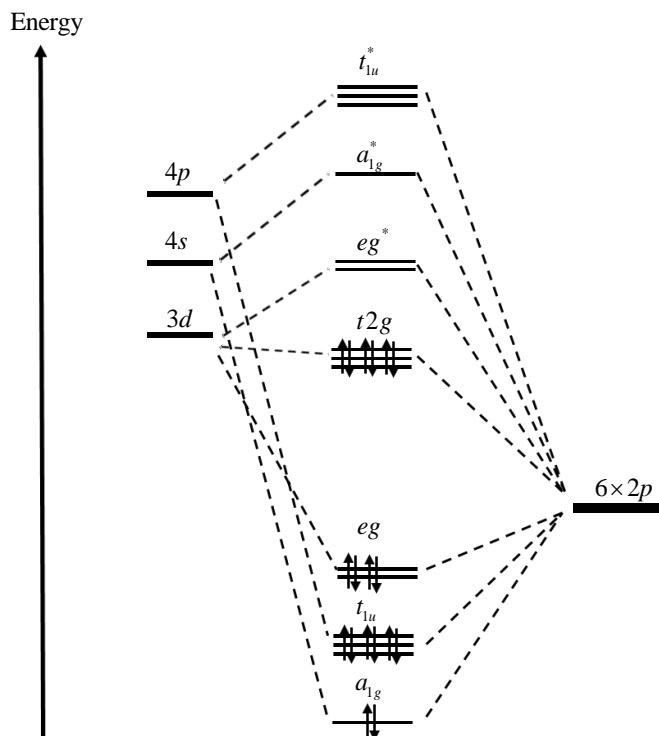


Figure 3.16. Molecular orbital diagram of the transition metal complex showing the  $d$  orbital electron population of  $\text{Co}^{3+}$  and O  $2p$  orbital.

### 3.4 References

1. Kasavajjula, U.; Wang, C.; Appleby, A. J., *J. Power Sources*, **2007**, *163*, 1003-1039.
2. Singh, V.; Joung, D.; Zhai, L.; Das, S.; Khondaker, S. I.; Seal, S., *Prog. Mater. Sci.*, **2011**, *56*, 1178-1271.
3. Zhang, S.; Zhao, K.; Zhu, T.; Li, J., *Prog. Mater. Sci.*, **2017**, *89*, 479-521.
4. Xu, R.; Zhao, K., *J. of Electrochem. Energy Convers. Storage*, **2016**, *13*, 030803.
5. Krishnan, R.; Lu, T.-M.; Koratkar, N., *Nano Lett.*, **2010**, *11*, 377-384.
6. Kim, H.; Cho, J., *Nano Lett.*, **2008**, *8*, 3688-3691.
7. Yao, Y.; McDowell, M. T.; Ryu, I.; Wu, H.; Liu, N.; Hu, L.; Nix, W. D.; Cui, Y., *Nano Lett.*, **2011**, *11*, 2949-2954.
8. Bhandavat, R.; Pei, Z.; Singh, G., *Nanomater. Energy*, **2012**, *1*, 324-337.
9. David, L.; Bhandavat, R.; Barrera, U.; Singh, G., *Nat. Commun.*, **2016**, *7*, 10998.
10. Ahn, D.; Raj, R., *J. Power Sources*, **2010**, *195*, 3900-3906.
11. Shen, J.; Ahn, D.; Raj, R., *J. of Power Sources*, **2011**, *196*, 2875-2878.
12. Fukui, H.; Nakata, N.; Dokko, K.; Takemura, B.; Ohsuka, H.; Hino, T.; Kanamura, K., *ACS Appl. Mater. Inter.*, **2011**, *3*, 2318-2322.
13. Shen, J.; Raj, R., *J. Power Sources*, **2011**, *196*, 5945-5950.
14. Fukui, H.; Ohsuka, H.; Hino, T.; Kanamura, K., *ACS Appl. Mater. Inter.*, **2010**, *2*, 998-1008.
15. Xu, R.; de Vasconcelos, L. S.; Zhao, K., *Mater. Res.*, **2016**, *31*, 2715-2727.
16. Oganov, A. R.; Glass, C. W., *J. Chem. Phys.*, **2006**, *124*, 244704.
17. Renlund, G. M.; Prochazka, S.; Doremus, R. H., *Mater. Res*, **1991**, *6*, 2716-2722.
18. Kresse, G.; Furthmüller, J., *Phys. Rev. B*, **1996**, *54*, 11169.
19. Kresse, G.; Joubert, D., *Phys. Rev. B*, **1999**, *59*, 1758.
20. Lee, D.; Vlassak, J. J.; Zhao, K., *Nano Lett.*, **2015**, *15*, 6553-6558.
21. Zhang, Y.; Li, Y.; Wang, Z.; Zhao, K., *Nano Lett.*, **2014**, *14*, 7161-7170.
22. Frisch, M.; Trucks, G.; Schlegel, H.; Scuseria, G.; Robb, M.; Cheeseman, J.; Scalmani, G.; Barone, V.; Mennucci, B.; Petersson, G., Gaussian 09 Package. Gaussian. Inc.: Wallingford, CT, USA **2009**.
23. Lu, T.; Chen, F., *J. Comput. Chem.*, **2012**, *33*, 580-592.
24. Ding, H.; Demkowicz, M. J., *Sci. Rep.*, **2015**, *5*, 13051.
25. Yu, L.; Raj, R., *Sci. Rep.*, **2015**, *5*, 14550.

26. Liao, N.; Zheng, B.; Zhou, H.; Xue, W., *Electrochim. Acta*, **2015**, *156*, 115-120.
27. Brequel, H.; Soraru, G.; Schiffrini, L.; Enzo, S., *J. Meta. Nanocryst. Mater.*, **2000**, *8*, 677-682.
28. Bréquel, H.; Parmentier, J.; Walter, S.; Badheka, R.; Trimmel, G.; Masse, S.; Latournerie, J.; Dempsey, P.; Turquat, C.; Desmartin-Chomel, A., *Chem. Mater.*, **2004**, *16*, 2585-2598.
29. Schiemenz, B.; Power, P. P., *Angew. Chem. Int. Ed. Engl.*, **1996**, *35*, 2150-2152.
30. Chen, H.; Jutzi, P.; Leffers, W.; Olmstead, M.; Power, P., *Organometallics*, **1991**, *10*, 1282-1286.
31. Liao, N.; Zheng, B.; Zhang, M.; Xue, W., *J. Mater. Chem. A*, **2016**, *4*, 12328-12333.
32. Bent, H. A., *Chem. Rev.*, **1961**, *61*, 275-311.
33. Pierson, H. O., *Handbook of carbon, graphite, diamonds and fullerenes: processing, properties and applications*. William Andrew: NJ, **2012**.
34. Albright, T. A.; Burdett, J. K.; Whangbo, M.-H., *Orbital interactions in chemistry*, 2<sup>nd</sup> ed; John Wiley & Sons: Hoboken, NJ, **2013**.
35. Mathur, R. B.; Singh, B. P.; Pande, S., *Carbon Nanomaterials: Synthesis, Structure, Properties and Applications*. CRC Press: FL, **2016**.
36. Peschel, G., Carbon-carbon bonds: hybridization. [http://www.physik.fu-berlin.de/einrichtungen/ag/ag-reich/lehre/Archiv/ss2011/docs/Gina\\_Peschel-Handout.pdf](http://www.physik.fu-berlin.de/einrichtungen/ag/ag-reich/lehre/Archiv/ss2011/docs/Gina_Peschel-Handout.pdf), **2011**, 5.
37. Sun, H.; Zhao, K., *J. Phys. Chem. C*, **2017**, *121*, 6002-6010.
38. Hermann, A. M.; Wang, Y. T.; Ramakrishnan, P. A.; Balzar, D.; An, L.; Haluschka, C.; Riedel, R., *J. Am. Ceram. Soc.*, **2001**, *84*, 2260-2264.
39. Riedel, R.; Bill, J.; Kienzle, A., *Appl. Organometallic Chem.*, **1996**, *10*, 241-256.
40. Tamayo, A.; Peña-Alonso, R.; Rubio, F.; Rubio, J.; Oteo, J., *J. Non-Crystalline Solids*, **2012**, *358*, 155-162.
41. Kroll, P., Tracing reversible and irreversible Li insertion in SiCO ceramics with modeling and ab-initio simulations *MRS Online Proceedings Library Archive*, **2011**, *1313*, 1-6
42. Service, R.F., *Science*, **2014**, *344*, 352-354.
43. Van Noorden, R., *Nature*, **2014**, *507*, 26-28.
44. Tarascon, J.M.; Armand, M., *Nature*, **2001**, *414*, 359-367.
45. Reddy, M.; Rao, G.S.; Chowdari, B., *Chem. Rev.*, **2013**, *113*, 5364-5457.
46. Cabana, J.; Monconduit, L.; Larcher, D.; Palacin, M.R., *Adv. Mater.*, **2010**, *22*, E170-E192.
47. Tang, Y.; Zhang, Y.; Deng, J.; Wei, J.; Tam, H.L.; Chandran, B.K.; Dong, Z.; Chen, Z.; Chen, X., *Adv. Mater.*, **2014**, *26*, 6111-6118.

48. Liu, S.; Wang, Z.; Yu, C.; Wu, H.B.; Wang, G.; Dong, Q.; Qiu, J.; Eychmüller, A.; Lou, X.W.; A. Eychmüller, A., *Adv. Mater.*, **2013**, *25*, 3462-3467.
49. Chernova, N.A.; Roppolo, M.; Dillon, A.C.; Whittingham, M.S., *J. Mater. Chem.*, **2009**, *19*, 2526-2552.
50. Mai, L.; Xu, L.; Han, C.; Xu, X.; Luo, Y.; Zhao, S. and Zhao, Y., *Nano Lett.*, **2010**, *10*, 4750-4755.
51. Li, Y.; Tan, B.; Wu, Y., *Nano Lett.*, **2008**, *8*, 265-270.
52. Lou, X.W.; Deng, D.; Lee, J.Y.; Feng, J.; Archer, L.A., *Adv. Mater.*, **2008**, *20*, 258-262.
53. Gao, X.P.; Bao, J.L.; Pan, G.L.; Zhu, H.Y.; Huang, P.X.; Wu, F.; Song, D.Y., **2004**, *J. Phys. Chem. B*, *108*, 5547-5551.
54. Zhu, X.; Zhu, Y.; Murali, S.; Stoller, M.D.; Ruoff, R.S., *ACS Nano*, **2011**, *5*, 3333-3338.
55. Varghese, B.; Reddy, M.V.; Yanwu, Z.; Lit, C.S.; Hoong, T.C.; Subba Rao, G.V.; Chowdari, B.V.R.; Wee, A.T.S.; Lim, C.T.; Sow, C.H., *Chem. Mater.*, **2008**, *20*, 3360-3367.
56. He, K.; Xin, H.L.; Zhao, K.; Yu, X.; Nordlund, D.; Weng, T.C.; Li, J.; Jiang, Y.; Cadigan, C.A.; Richards, R.M.; Doeff, M.M., *Nano Lett.*, **2015**, *15*, 1437-1444.
57. Kim, H.; Lee, J.T.; Magasinski, A.; Zhao, K.; Liu, Y.; Yushin, G., *Adv. Energy Mater.*, **2015**, *5*, 1501306.
58. McDowell, M.T.; Lee, S.W.; Ryu, I.; Wu, H.; Nix, W.D.; Choi, J.W.; Cui, Y., *Nano Lett.*, **2011**, *11*, 4018-4025.
59. Chan, C.K.; Zhang, X.F.; Cui, Y., *Nano Lett.*, **2008**, *8*, 307-309.
60. Coquet, R.; Willock, D.J., *Phys. Chem. Chem. Phys.*, **2005**, *7*, 3819-3828.
61. Ding, H.; Ray, K.G.; Ozolins, V.; Asta, M., *Phys. Rev. B*, **2012**, *85*, 012104.
62. Sitepu, H.; O'Connor, B.H.; Li, D.; *J. Appl. Crystallog.*, **2005**, *38*, 158-167.
63. Zhao, K.; Tritsarlis, G.A.; Pharr, M.; Wang, W.L.; Okeke, O.; Suo, Z.; Vlassak, J.J.; Kaxiras, E., *Nano Lett.*, **2012**, *12*, 4397-4403.
64. Baldoni, M.; Craco, I.; Seifert, G.; Leoni, S., *J. Mater. Chem. A*, **2013**, *1*, 1778-1784.
65. Li, F.; Cabrera, C.R.; Chen, Z., *J. Mater. Chem. A*, **2014**, *2*, 19180-19188.
66. Xia, W.; Zhang, Q.; Xu, F.; Sun, L., *ACS Appl. Mater. Interfaces*, **2016**, *8*, 9170-9177.
67. Whittingham, M.S., *Chem. Rev.*, **2004**, *104*, 4271.
68. He, P.; Yu, H.; Zhou, H., *J. Mater. Chem.*, **2012**, *22*, 3680.
69. Whittingham, M.S., *MRS Bull.*, **2008**, *33*, 411.
70. Andre, D.; Kim, S.J.; Lamp, P.; Lux, S.F.; Maglia, F.; Paschos, O.; Stiaszny, B., *J. Mater. Chem. A*, **2015**, *3*, 6709.

71. Koyama, Y.; Tanaka, I.; Adachi, H.; Makimura, Y.; Ohzuku, T., *J. Power Sources*, **2003**, *119*, 644.
72. Zhang, S.; Zhao, K.; Zhu, T.; Li, J., *Prog. Mater. Sci.*, **2017**, *89*, 479.
73. Zhao, K.; Cui, Y., *Extreme Mech. Lett.*, **2016**, *9*, 347.
74. Li, G.; Zhang, Z.; Huang, Z.; Yang, C.; Zuo, Z.; Zhou, H., *J. Solid State Electrochem.*, **2017**, *21*, 673.
75. Xu, R.; Zhao, K., *Extreme Mech. Lett.*, **2016**, *8*, 13.
76. Kim, N.Y.; Yim, T.; Song, J.H.; Yu, J.S.; Lee, Z., *J. Power Sources*, **2016**, *307*, 641.
77. Lang, M.; Darma, M.S.D.; Kleiner, K.; Riekehr, L.; Mereacre, L.; Pérez, M.Á.; Liebau, V.; Ehrenberg, H., *J. Power Sources*, **2016**, *326*, 397.
78. Sun, G.; Sui, T.; Song, B.; Zheng, H.; Lu, L.; Korsunsky, A.M.; *Extreme Mech. Lett.*, **2016**, *9*, 449.
79. Xu, R.; Vasconcelos, L.S.; Shi, J.; Li, J.; Zhao, K., *Exp. Mech.*, **2018**, *58*, 549-559.
80. Zhou, F.; Cococcioni, M.; Marianetti, C.A.; Morgan, D.; Ceder, G., *Phys. Rev. B*, **2004**, *70*, 235121.
81. Van der Ven, A.; Aydinol, M.K.; Ceder, G.; Kresse, G.; Hafner, J., *Phys. Rev. B*, **1998**, *58*, 2975.

## CHAPTER 4. THERMAL-INDUCED POLYMORPHIC TRANSITIONS IN ORGANIC SEMICONDUCTOR CRYSTALS

This chapter is based, in part, on the research described in the following publications

**Sun, H.**; Park, S. K.; Diao, Y.; Kvam, E. P.; Zhao, K., “Molecular Mechanisms of Superelasticity and Ferroelasticity in Organic Semiconductor Crystals” *submitted, 2020*.

Park, S. K. †; **Sun, H.** †; Chung, H.; Patel, B. B.; Zhang, F.; Davies, D. W.; Woods, T. J.; Zhao, K.; Diao, Y., *Angew. Chem. Int. Ed.*, **2020**, *59*, 13004. (†:denotes equal contribution)

### 4.1 Introduction

#### 4.1.1 Organic Crystals

Organic solids compromise molecules held together by weak intermolecular interactions such as Van der Waals forces or hydrogen bonding. Compared to covalently or ionically bonded atomic compounds, organic solids have unrivaled advantages in terms of lightweight, low cost, and versatility in chemical synthesis, which attract enormous interest in solid-state chemistry, crystal engineering, and pharmaceutical science<sup>1-5</sup>. The crystalline forms of molecular solids, famous for their high purity and excellent optoelectronic properties, warrant particular attention as they can serve as the perfect physical platforms to study the structure-property relationships of molecular systems.

Nevertheless, organic crystals usually possess poor mechanical properties. They were deemed brittle and would disintegrate within 2% strain, which impeded their application potential in the industry. Recently, several reports of highly bendable molecular crystals shed light on harvesting the flexibility in organic solids. The flexibility is generally manifested by elastic and plastic deformation. Materials subjected to elastic deformation can regain the original shape after releasing the stress while plasticity can disrupt the structure and result in irreversible deformation. Reddy et al reported remarkable elasticity in caffeine co-crystals, which was attributed to the rearrangement of the three-dimensional weak network formed by CH- $\pi$  interaction<sup>1</sup>. McMurtrie and coworkers demonstrated the copper acetylacetonate crystals are flexible enough to be reversibly tied into a knot which can withstand ~4% strain before breaking<sup>6</sup>. They attributed the high elastic flexibility to the reversible rotation of molecules under strain by

experimental investigation of micro-focused synchrotron radiation. Naumov et al. discovered the extraordinary plastic deformation in crystals of hexachlorobenzene that can be bent mechanically at multiple locations to  $360^\circ$  with retention of macroscopic integrity. They claimed that the plastic deformation requires the sliding of layers by breaking and re-formation of halogen-halogen interactions<sup>3</sup>. In a nutshell, the above studies have revealed that the mechanical properties of organic solids are dictated by the packing structures and dynamic intra- and intermolecular interactions. Hence, it's imperative to reach the mechanistic understanding of relations between structural dynamics and mechanical responses to promote the design principles of molecular design. Nevertheless, the intricate molecular dynamics and fast phase evolution in organic solids challenge a direct experimental observation. To this end, molecular simulation is desired to scrutinize the instantaneous changes of the molecular structure exposed to various environmental stimuli such as heat, pressure, and light. It was long believed that the mechanical load and thermal load play an equivalent role in triggering phase transitions<sup>7</sup>. The polymorphic transitions of organic solids are much easier to be achieved and examined in a thermal condition considering the brittleness of organic crystals and complex choices of mechanical loads. Herein, we will primarily focus on investigating the molecular mechanisms of thermal-induced polymorphic transitions in a model semiconductor crystal. Later, in *Chapter 5*, we will dive into the underlying mechanisms of versatile cooperative transitions induced by multiple mechanical loads.

Molecules and polymers with extended  $\pi$ -conjugation warrant intensive studies in the emerging field of organic semiconductors owing to their effective charge transferability and solution processability. They are now actively pursued in the development of flexible and printed devices, such as solar cells, light-emitting diodes, field-effect transistors, sensors, wearable devices, and electronic skins<sup>8,9</sup>. Among them, TIPS-pentacene (6,13-bis(triisopropylsilylethynyl)pentacene) molecules is recognized as one of the most popular semiconducting materials used in the organic field-effect transistors (OFETs). TIPS-pentacene crystals exhibit rich polymorphisms, wherein five distinct polymorph structures were discovered by in-situ annealing method<sup>10</sup>. Three of them can be thermodynamically stabilized at three different temperature regimes. Figure 4.1 shows the lattice parameters of thermal-induced three polymorphs determined by XRD experiments. We highlight the major differences between the

three polymorphs in terms of  $b$  and  $\gamma$ :  $b$  axis gradually increases from Form I to III while the angle  $\gamma$  decreases.

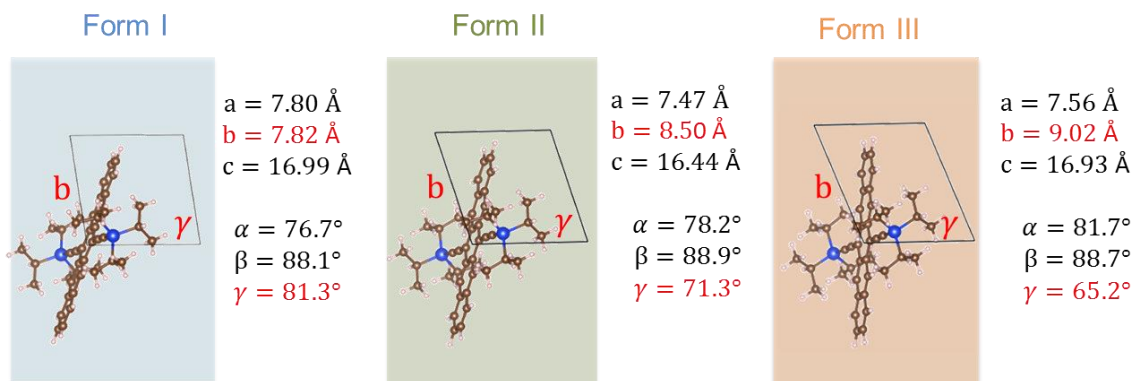


Figure 4.1. Molecular lattices of TIPS-pentacene polymorphs Form I, II, and III.

#### 4.1.2 Challenges in Atomistic Simulation

Compared to the extensive mechanistic studies of phase transition in atomic compounds, the atomistic investigation of the polymorphic transition in organic solids presents many challenges.<sup>1)</sup> **Intricate structural motions.** The polymorphic transition of atomic compounds usually involves the shuffling and gliding of atoms, accompanying the changes in atomic position and the numbers of coordination neighbors. While, the molecular motions in the polymorphic transition of molecule crystals are much more complicated since it's not only associated with the positions of molecules but also involving the motion of each atom within the molecules, such as the rotational movements of backbone and side groups in TIPS-pentacene system. Considering the massive degrees of freedom involved in the molecule system, it's a grand challenge to infer the governing structural mechanism which triggers the polymorphic transition. 2) **Ambiguous Intermolecular interactions.** To date, the pseudopotential with appropriate dispersion forces corrections adopted in ab-initio modeling performs well in describing the molecular interactions in organic crystals. However, the computation efficiency of ab-initio modeling reduces considerably when the size of a model system exceeds 200 atoms. Besides, the temperature fluctuations in a small molecular model could be drastic, which imposes great challenges on exploring the polymorphic transition induced by the thermal load. Thus, the density functional theory based pseudopotential would not be considered as an appropriate choice to simulate the semiconducting molecules with large conjugated cores.

Molecular dynamic (MD) simulation is commonly employed to conduct atomistic simulation on a relatively large scale (millions of atoms). However, MD simulation uses empirical force field parameters to describe the atomic interactions, which requires intensive training based on experiments or ab-initio simulation. The energetic descriptors of TIPS-pentacene molecules need to be carefully examined to obtain reliable simulation results. 3) **Rich polymorphic transitions.** TIPS-pentacene crystals exhibit rich polymorphisms under thermal or mechanical load. To unambiguously determine each phase in the dynamic process, the precise phase descriptor for this molecular system (i.e. order parameter) is demanded. Nevertheless, the knowledge space regarding the kinetics and thermodynamics of organic polymorphic transition is rather vacant, which motivates us to set forth new characterization methods and analysis frameworks in modeling.

## 4.2 Simulation Methods

To overcome the above challenges, a variety of calculation methods and simulation tools are adopted in this work. They can be generally described as three parts including structure searching algorithm, first principle simulation, and molecular dynamics simulation.

### 4.2.1 Ab-initio Modeling

Although XRD experiments could resolve the basic lattice information of polymorph crystal, there is no structural correspondence between any two polymorphs and no hints about the dynamic evolution during the phase transition. However, in order to pursue the transition kinetics by atomic modeling, it's vital to find out the initial configurations of three polymorphs with their lattice correspondence. That means, the positions of each atom in the lattices of Form II and Form III should be directly derived from the mother lattice Form I after the phase transition. Starting from the given initial configuration, it will be a great challenge to capture the lattice evolution of six degrees of freedom ( $a$ ,  $b$ ,  $c$ ,  $\alpha$ ,  $\beta$ , and  $\gamma$ ) merely by ab-initio modeling at a small scale. The automated, iterative algorithms as described below are proposed to investigate the single molecular kinetics in the unit cell during the polymorphic transition by heating or mechanical stimuli.

Traditional ways such as the minima hopping method and evolutionary algorithm by comparing the ground state free energies of a variety of possible structures require significant user input. These methods are simply not applicable in capturing the dynamic phase transition of six independent lattice parameters during continuous heating and mechanical load. We propose an automated algorithm to search for the stable polymorphs associated with phase transitions. Figure 4.2 shows the process from the transition of Form I to II. During heating (left panel in Figure 4.2), Form I is heated up to a temperature range of 400~550K under the NVT ensemble. The structure at elevated temperature is energetically relaxed to reach local energy minima. The first screening will be based on the change in  $\gamma$ , which indicates the major difference between the two polymorphs. The evolved structures with a  $\gamma$  change of  $10^\circ$  ( $15^\circ$ ) will be selected as the seed Form II (III). Next, other lattice parameters,  $\alpha$ ,  $\beta$ ,  $a$ , and  $b$ , will be carefully compared using the two inequities as the second screening criterion. The structural search succeeds if two screening criteria are satisfied. Any failure in convergence will lead to a change of setting in the parametric input of the heating modeling, such as the heating rate, time step, heating algorithm, etc. The mechanical load follows a similar manner (right panel in Figure 4.2). The mechanical load is applied by choosing a  $3 \times 3$  transformation matrix and an initial strain rate of 0.1%. The deformed lattice after each incremental strain will be subject to static relaxation to reach the local energy minimum. The successive screening criteria are the same as those in heating. Different from heating, the lattice will exhibit much more varieties in lattice parameters under different types and different degrees of mechanical load. The structural search during mechanical load usually requires multiple iterative refinements of parametric input to reach the desired final structure.

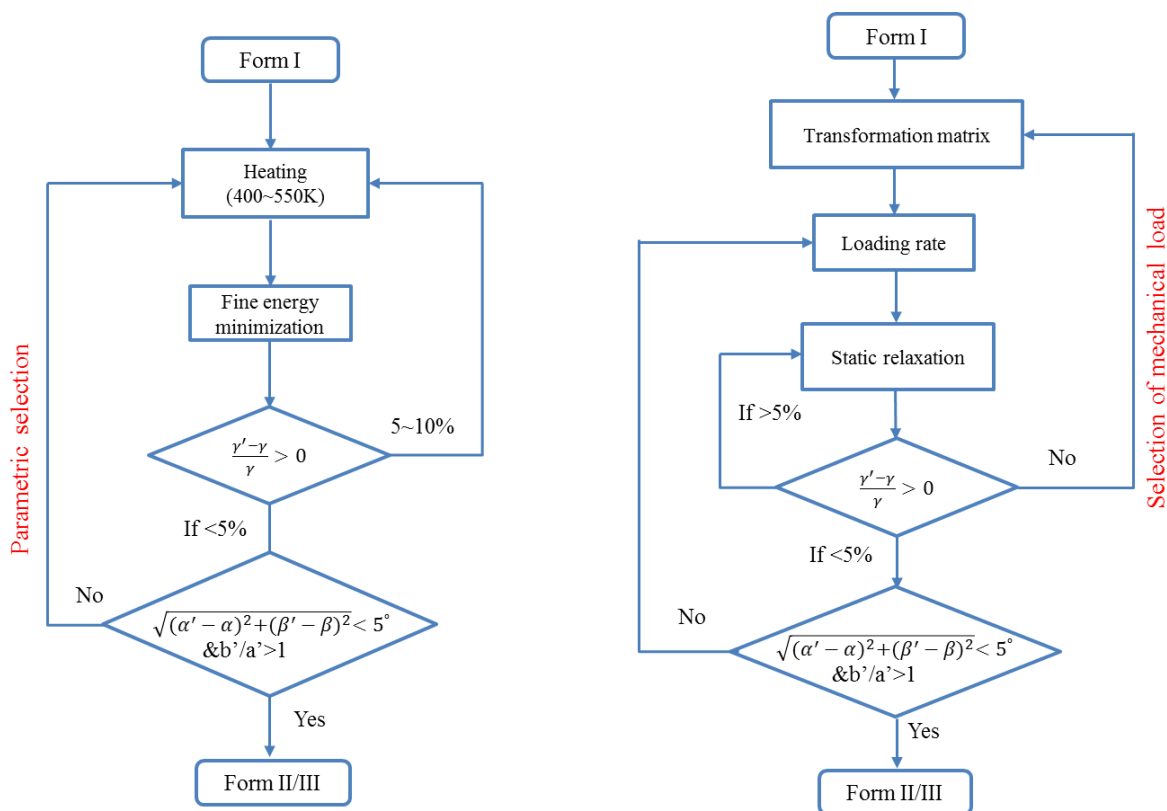


Figure 4.2. Structural search during heating and mechanical load in ab initio molecular modeling

Starting from the Form I lattice structure obtained from XRD experiments, the unit cell structure of Form II and Form III are determined by DFT simulation under specific heating and loading conditions. The details are already described in the above structural searching part. All the calculation in the *Structure Search* part is done by the Vienna Ab-initio Simulation Package (VASP)<sup>11</sup>, in which the projector-augmented wave pseudopotentials and the general gradient approximation for the exchange-correlation functional are used. The general dispersion correction (DFT-D3 method) for the GGA-PBE functional<sup>12</sup> is added to accurately mimic the intermolecular interactions in the molecular crystal. The ab-initio molecular dynamics with a time step of 1fs is used in the heating process.

#### 4.2.2 Force Field Parameterization

In the OPLS-AA force field set, the total energy of the molecular system is calculated as the sum of multiple energetic terms for the harmonic bond stretching, harmonic angle bending, a Fourier series of torsional (dihedral and improper)energetics, and Coulomb and 12-6 Lennard-

Jones potential for the nonbonded interactions, which are exhibited in the Equation 4.1-4.4 accordingly<sup>13</sup>.

$$E_r = K_r(r - r_{eq})^2 \quad (4.1)$$

$$E_\theta = K_\theta(\theta - \theta_{eq})^2 \quad (4.2)$$

$$E_\phi = \frac{1}{2}V_1[1 + \cos(\phi)] + \frac{1}{2}V_2[1 - \cos(2\phi)] + \frac{1}{2}V_3[1 + \cos(3\phi)] + \frac{1}{2}V_4[1 - \cos(4\phi)] \quad (4.3)$$

$$E_{nb} = 4\epsilon \left[ \left( \frac{\sigma}{r} \right)^{12} - \left( \frac{\sigma}{r} \right)^6 \right] + \frac{q_i q_j e^2}{r} \quad (4.4)$$

The required parameters are the bonding force constants  $K_r$ , the bending force constant  $K_\theta$ , the equilibrium values for the bond length and bending angle  $r_{eq}$  and  $\theta_{eq}$ , the Fourier coefficients  $V$ , the partial atomic charges,  $q$ , the Lennard-Jones radii  $\sigma$  where the inter-particle potential is zero, and the depth of the potential well  $\epsilon$ . The symbols and atom types used in OPLS-AA force field are listed in

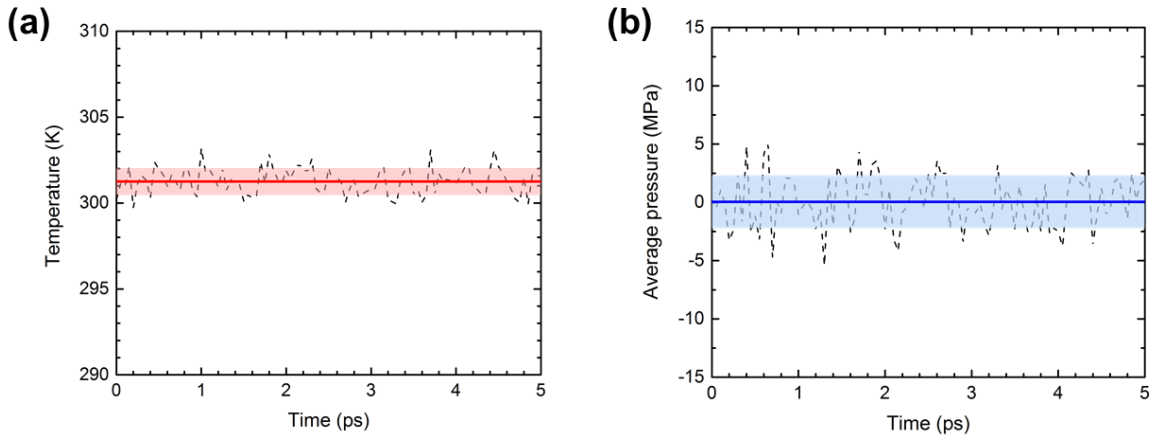


Figure 4.5. **a** The temperature fluctuations and **b** the average pressure fluctuations of the  $24 \times 48 \times 1$  supercell model of Form I for the equilibrium 5 ps after running the MD simulation under NPT ensemble at 27°C and zero pressure for 200 ps.

Table 4.1 and also demonstrated in the molecular structure (Figure 4.3). The atomic charges are calculated using the electrostatic potential (ESP) fitting method and assigned to each atom type shown in

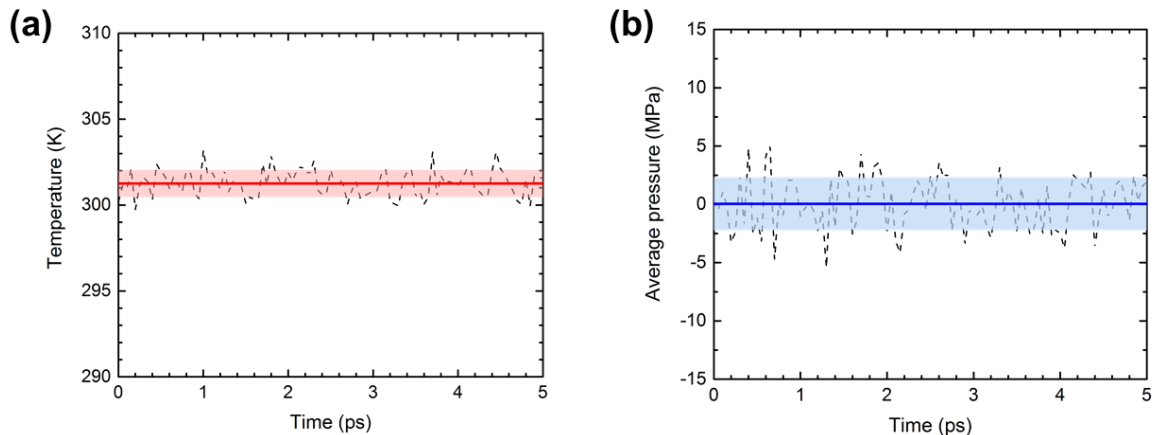


Figure 4.5. **a** The temperature fluctuations and **b** the average pressure fluctuations of the  $24 \times 48 \times 1$  supercell model of Form I for the equilibrium 5 ps after running the MD simulation under NPT ensemble at  $27^\circ\text{C}$  and zero pressure for 200 ps.

Table 4.1 as well. The Lennard-Jones parameters for each atom type and most of the energetic parameters for the bond length, angles, dihedrals, and impropers are adopted from the original OPLS-AA database<sup>13</sup>.

However, several force field parameters associated with the *sp* carbon and silicon in TIPS-P molecule are missing. Specifically, they are, bond stretching parameters for the CZ<sup>I</sup>-Si bond, the angle bending parameters for the CZ<sup>I</sup>-Si-CT<sup>II</sup> bond angle, and CZ<sup>II</sup>-CZ<sup>I</sup>-Si bond angle, torsion energetic parameters for the CZ<sup>I</sup>-Si-CT<sup>II</sup>-CT<sup>I</sup> dihedral and CZ<sup>I</sup>-Si-CT<sup>II</sup>-HC<sup>II</sup> dihedral. The parameterization process is described as follows. We first examine the equilibrium values for the above bond length, bond angles and dihedral angles by applying the quantum mechanics calculations. The geometric optimization of TIPS-P molecule, the single-point energy calculations and also the partial charges calculations are all conducted using the GAUSSIAN09 program<sup>14</sup> under the density functional theory level with the B3LYP hybrid functional and the 6-311++G(d,p) basis set. The equilibrium bond length  $r_{eq}$ , angles  $\theta_{eq}$  obtained from the optimized configuration are listed in Table 4.2 and Table 4.3. Next, to get the bonding/bending force constants and torsion Fourier coefficients, the energy scan of the specific bond, angle and dihedral are conducted by performing single-point energy calculations on varying bond length, bending angle, and dihedral angle around their equilibrium values, respectively. The resulting changes in their conformational energy are fitted into the corresponding OPLS-AA bond stretching, bending angle, and torsion energetics formula (Equation 4.1-4.3). The good comparison between the ab-initio data and the fitted curves is demonstrated in Figure 4.4. The fitted parameters including the bonding/bending force constants and torsion Fourier coefficients are also shown in Table 4.2 and Table 4.3. The complete force field parameter set and the associated topological data of TIPS-P crystal are incorporated into the LAMMPS software<sup>15</sup> by home-built codes. A cutoff distance of 6Å is chosen for both the Lenard-Jones potential and long coulombic interactions, which most stabilizes the lattice structure in the NPT ensemble (27°C and zero pressure) and gives the closest agreements with the experimental lattice data, based on current force field parameter set. Figure 4.5 demonstrates the temperature and pressure profile of Form I for the equilibrium 5 ps after running the NPT simulation at 27°C and zero pressure for 200 ps. The thermal fluctuations at the equilibrium states are well controlled with a standard temperature deviation of 1K and the average pressure is also well stabilized within a range of -

2~2 MPa. Thus, we can believe that the new force field parameters would be suitable for the molecular dynamics simulation at ambient conditions.

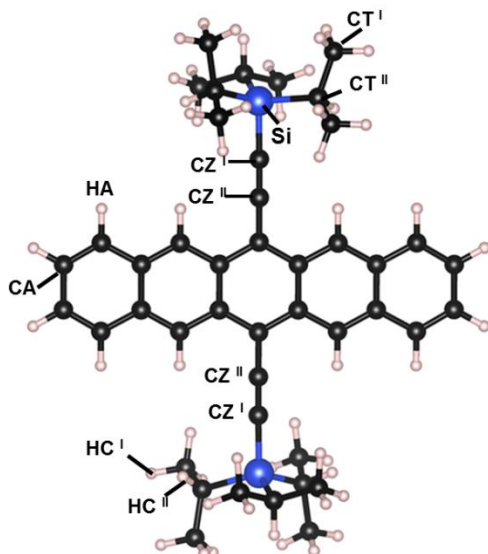


Figure 4.3. The atom symbol of OPLS-AA force field assigned to each atom in TIPS-P molecule. **CA** and **HA** are for carbon atom and hydrogen atom of pentacene backbone, respectively. **CT<sup>I</sup>** and **HC<sup>I</sup>** are for carbon atom and hydrogen atom of the methyl group in the TIPS unit, respectively. **CT<sup>II</sup>** is for carbon atom connecting Si atom and two methyl groups in the TIPS unit. **HC<sup>II</sup>** is for hydrogen atom bounded to **CT<sup>II</sup>** atom. **CZ<sup>I</sup>** and **CZ<sup>II</sup>** are for the *sp* carbon atoms.

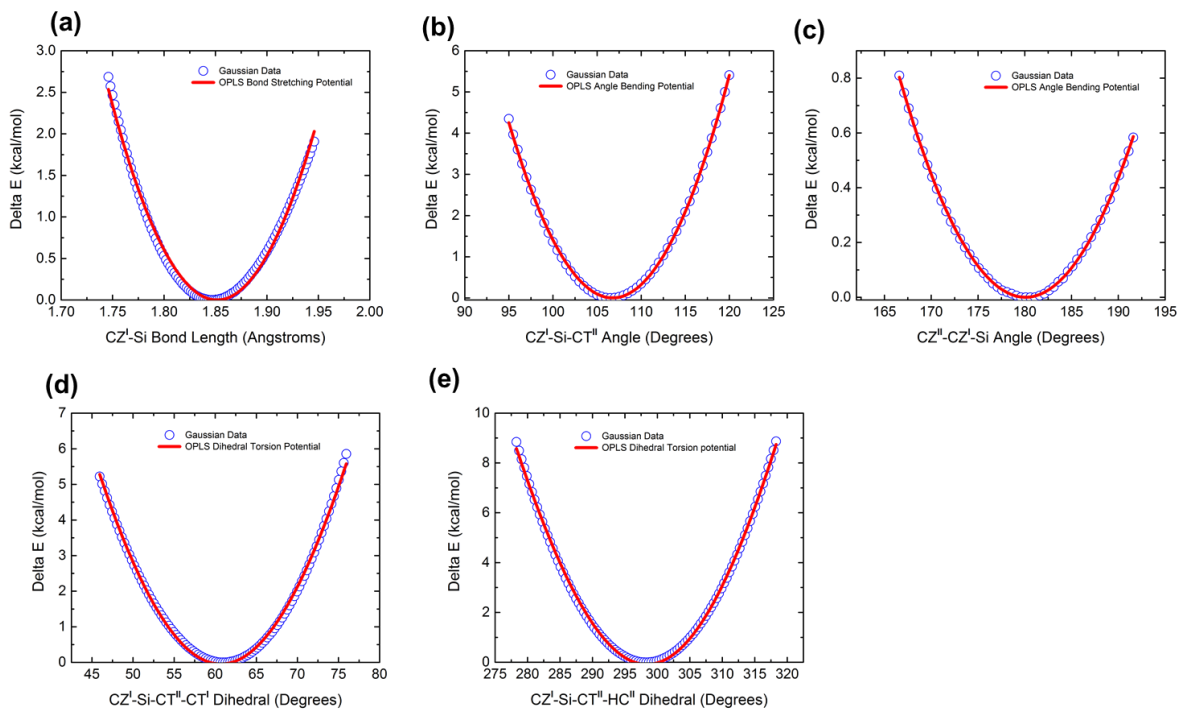


Figure 4.4. The comparison between DFT single point energies (blue dots) and the fitted curve (red lines) using the OPLS force field equations for the specific bond length, angle and dihedral angles.

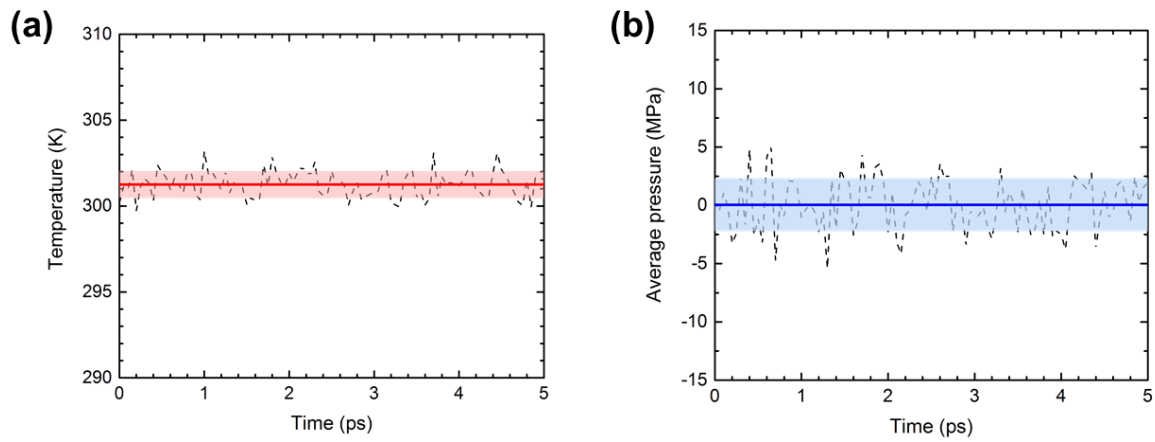


Figure 4.5. **a** The temperature fluctuations and **b** the average pressure fluctuations of the  $24 \times 48 \times 1$  supercell model of Form I for the equilibrium 5 ps after running the MD simulation under NPT ensemble at  $27^\circ\text{C}$  and zero pressure for 200 ps.

Table 4.1. The atom symbol, atomic charges and atom type used in OPLS-AA force field.

Atom symbol	Atomic charge (e)	Atom type in OPLS-AA
CT <sup>I</sup>	-0.40	Alkane CH3-
CT <sup>II</sup>	0.35	Alkyl Silane R2CH-Si
CZ <sup>I</sup>	-0.68	Alkyne RCCR
CZ <sup>II</sup>	0.38	
CA	-0.09	Aromatic C
HA	0.16	Aromatic H-C
HC <sup>I</sup>	0.08	Alkane H-C
HC <sup>II</sup>	-0.06	
Si	0.42	Alkyl Silane R4Si

Table 4.2. Re-parameterized force field parameters for the bond lengths and angles associated with *sp* carbon atom and silicon atom in TIPS-P molecule.

Bond	$K_r$ (kcal/(mol · Å <sup>2</sup> ))	$l_0$ (Å)
CZ <sup>I</sup> -Si	227.5168	1.8516
Angle	$K_\theta$ (kcal/(mol · rad <sup>2</sup> ))	$\theta_0$ (°)
CZ <sup>I</sup> -Si-CT <sup>II</sup>	101.1104	106.7551
CZ <sup>II</sup> -CZ <sup>I</sup> -Si	14.4443	180.0790

Table 4.3. Re-parameterized force field parameters for the dihedral angles associated with *sp* carbon atom and silicon atom in TIPS-P molecule.

Dihedral	$V_1$ (kcal/mol)	$V_2$ (kcal/mol)	$V_3$ (kcal/mol)
CZ <sup>I</sup> -Si-CT <sup>II</sup> -CT <sup>I</sup>	1.5198	-1.5644	37.1337
CZ <sup>I</sup> -Si-CT <sup>II</sup> -HC <sup>II</sup>	3.3464	-3.3793	34.4374

### 4.2.3 Genetic-Algorithm Refined Molecular Dynamics

The simulation is carried out using the molecular dynamics software LAMMPS package<sup>15</sup>. The OPLS-AA force field<sup>13</sup> is adopted to describe molecular interactions. The supercell of Form I is built by expanding the unit cell obtained from the XRD experiments, containing 51200 atoms (512 molecules) with a size of 12.8 nm × 12.3 nm × 3.3 nm (along the X, Y and Z directions). The structure is energetically relaxed under NPT at 300K and zero pressure for 0.5 ns. Heating is conducted in the range of 300K~550K with a heating rate of 0.625 K/ps.

In the OPLS-AA force field, the energetic parameters for intramolecular interactions (bond, angle, torsional, improper) were carefully calibrated in our previous work<sup>16</sup>. This study focuses on the parametric training of the intermolecular potential including the coulombic and van der Waals interactions (Figure 4.6), which is crucial for simulating the structural changes in organic

solids. Since the electrostatic potential usually acts more strongly than van der Waals interactions<sup>16</sup>, we first calibrate the coulombic partial charges to obtain Form II at 400K. Next, van der Waals parameters are refined to capture the phase evolution. Then, Form II-to-III transition is examined at 500K to determine whether the training succeeds. To perform the optimization in a space of high dimensionality, we adopt the genetic algorithm, which is an evolutionary algorithm that mimics the natural selection process. In coulombic parametric training, we start with the seed parameters obtained by the electrostatic potential (ESP) fitting and generate the first generation by randomly populating a set of parameters that lie within physically allowable limit ( $\pm 1.5$  times) of the seed while retaining the charge neutrality. The objective function is defined as  $F_I = \frac{1}{2} \sqrt{\left(\frac{b'-b}{b}\right)^2 + \left(\frac{\gamma'-\gamma}{\gamma}\right)^2}$ , where the lattice length  $b$  and angle  $\gamma$  are the experimental values for Form II and  $b'$  and  $\gamma'$  denote the simulated values. The sets of parameters are then ranked in ascending order of the evaluation values of the objective function. 60% of parameters with the lowest values are selected to perform the genetic operations of mutation with a rate of 5% and crossover with a rate of 10%. The optimization succeeds if the objective function converges ( $< 5\%$ ). Any failure in convergence will lead to the next offspring generation. At this stage, van der Waals parameters from the OPLS database are preserved and a cutoff distance of 8 Å is chosen for all intermolecular interactions. 105 sets of best partial charges selected from 50 generations (100 populations for each generation) are further examined by the screening criteria of  $\frac{1}{4} \sqrt{\sum \left(\frac{p_i' - p_i}{p_i}\right)^2} < 10\%$ , where  $p_i'$  and  $p_i$  refer to the simulated and experimental values for other lattice parameters except for  $b$  and  $\gamma$ . Next, in the training of van der Waals parameter, to capture the characteristics of the first-order transition, a fine criterion is chosen as  $F_{II} = \frac{|\varepsilon_h - \varepsilon_l - \delta|}{\delta}$ , whereas  $\varepsilon_l$  and  $\varepsilon_h$  are the low and high bound values of  $b$  length change at the transition point, and  $\delta$  denotes the change measured by experiments. Lastly, the cutoff radii for the two potentials are slightly tuned within  $\pm 1.2$  times of 8 Å to achieve the best fitting performance. The trained intermolecular parameters are listed in Table 4.4 and Table 4.5.

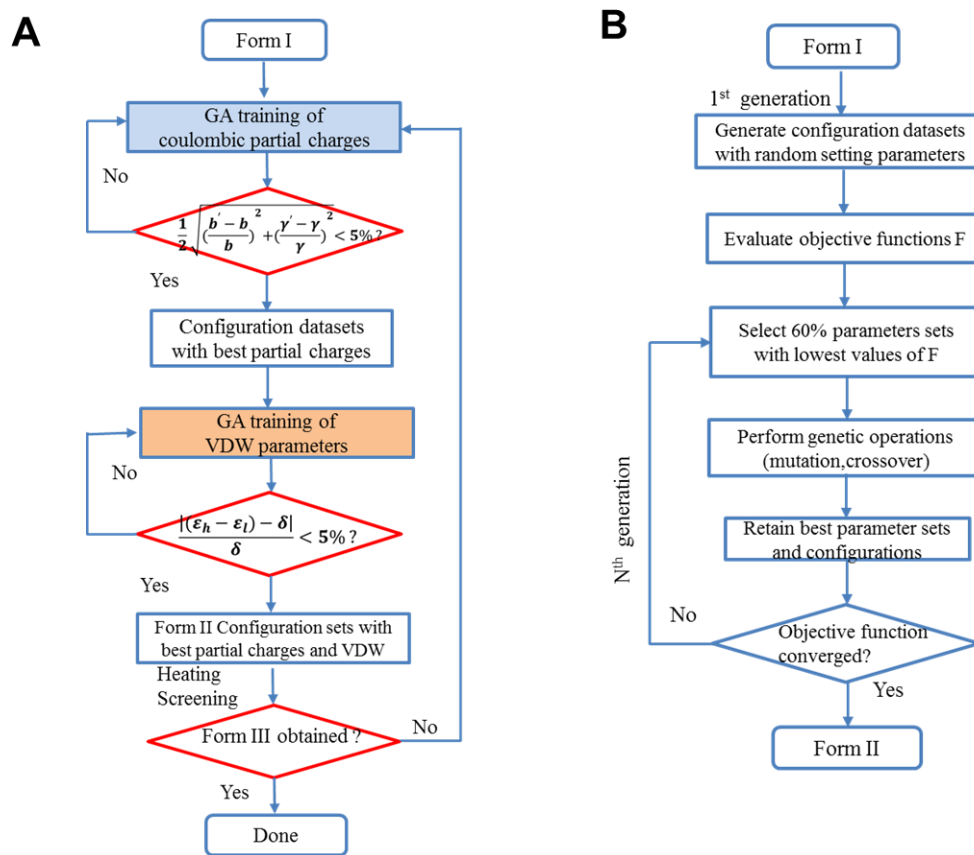


Figure 4.6. (A) Flowchart of parametric training for coulombic and Van der Waals parameters. (B) The workflow of the Genetic-Algorithm training module.

Table 4.4. Coulombic partial charges for TIPS-pentacene molecules.

Atomic symbol	Atomic charge (e)	Atomic type in OPLS-AA
CT <sup>I</sup>	0.0448	Alkane CH3-
CT <sup>II</sup>	0.1611	Alkyl Silane R2CH-Si
CZ <sup>I</sup>	0.1659	Alkyne RCCR
CZ <sup>II</sup>	-0.0194	
CA	0.0754	Aromatic C
HA	-0.1685	Aromatic H-C
HC <sup>I</sup>	-0.055	Alkane H-C
HC <sup>II</sup>	0.0595	
Si	0.0938	Alkyl Silane R4Si

Table 4.5. Van der Waals parameters for TIPS-pentacene molecules.

Atomic symbol	Depth of potential well (Kcal/mol)	Lennard-Jones radii (Å)	Atomic type in OPLS-AA
CT	0.05957	3.5	Alkane CH3-
CZ	0.2005	3.3	Alkyne RCCR
CA	0.06383	3.55	Aromatic C
HA	0.03066	2.42	Aromatic H-C
HC	0.03580	2.5	Alkane H-C
Si	0.09025	4.0	Alkyl Silane R4Si

## 4.3 Results and Discussion

### 4.3.1 Structure Search

Our initial study on the phase transition from Form I to Form II in TIPS-pentacene triggered by both heating and mechanical load, Figure 4.7, provides encouraging results in support of our hypothesis. The Form I is constructed based on the crystal structure information collected from XRD experiments<sup>10</sup>. The chemical building blocks contain 100 atoms. The optimized lattice parameters ( $a$ ,  $b$ ,  $c$ ,  $\alpha$ ,  $\beta$ , and  $\gamma$ ) of two polymorphs are in great agreement with the experimental data with an error of less than 2%. The phase transition is modeled by both heating (400K-550K) and mechanical load (uniaxial tension, pure shear, and tri-axial tension). The structure starts from Form I, and incremental heating or mechanical deformation (through lattice transformation matrix) is applied by ab-initio molecular dynamics (AIMD) modeling. To capture the structural evolution during the dynamic load, we develop an automated structural searching algorithm (*Simulation Methods*) to reduce the uncertainty in the small-scale modeling. During heating, the thermal energy causes both rotational and displacive motions of the backbone in Form I. The side group accommodates the deformation and experience an order-to-disorder transition as seen in the initial structure (left snapshot) and the saddle configuration (middle snapshot) in Figure 4.7. In the further energetic optimization of the molecule configuration at the saddle point, Form II emerges with the characteristics of  $\gamma$  being reduced by  $10^\circ$  and  $b$  axis being increased by  $0.7 \text{ \AA}$ . To mimic the uniaxial load, pure shear, and tri-axial tension, we apply three different strain matrixes to Form I. The values listed in Figure 4.7 indicate the critical strains that cause the transition from Form I to Form II. The pure shear requires the lowest threshold strain to transform the lattice. More interestingly, upon cooling or applying an opposite mechanical load,

the generated Form II can completely transfer back the original structure Form I. Besides, Form III is also generated by applying appropriate shear strain onto Form I. Table 4.6 demonstrates the lattice parameters of three polymorphs obtained from structural searching under heating or different types of mechanical loads, which match well with the experimental data. The generated Form II and Form III from the mother lattice of Form I will be adopted as the initial structure input for the following large scale atomic simulation. Moreover, we are also able to explore the free energies of the intermediate configurations, the energy barrier of the saddle point, and the thermal and mechanical driving forces that transform the lattice. Such energetic analyses will be illustrated in the thermodynamics part.

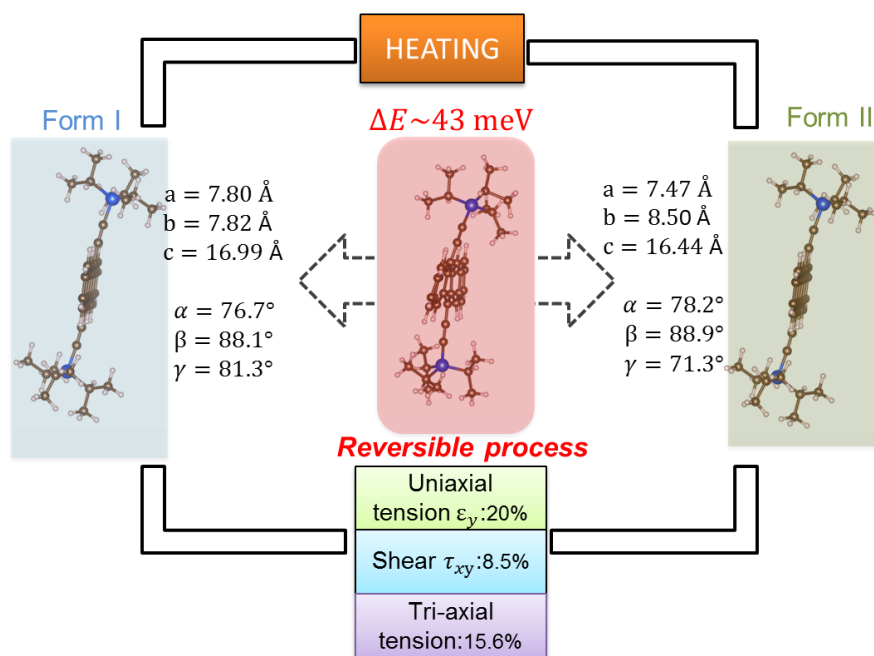


Figure 4.7. Preliminary modeling results of phase transition (Form I – Form II) in TIPS-pentacene induced by heating and mechanical load. The transition is reversible, with a energy barrier of 43 meV.

Table 4.6. The six lattice parameters (a, b, c,  $\alpha$ ,  $\beta$ ,  $\gamma$ ) of optimized polymorphs obtained from the structural searching algorithms agree well with the experimental data. The percentage differences between simulation and experimental data are shown in the parentheses.

Form I						Form II					
a	b	c	$\alpha$	$\beta$	$\gamma$	a	b	c	$\alpha$	$\beta$	$\gamma$
7.99	7.77	17.12	73.65	88.5	82.03	7.58	8.49	17.84	75.9	88.7	70.8
(+3.0%)	(+0.4%)	(+1.0%)	(-5.4%)	0.00%	(-0.2%)	(-0.3%)	(-1.0%)	(+3.5%)	(-2.9%)	(+2.3%)	(-1.8%)

Form II						Form II					
a	b	c	$\alpha$	$\beta$	$\gamma$	a	b	c	$\alpha$	$\beta$	$\gamma$
8.04	8.42	17.11	75.9	86.6	72.4	8.20	9.76	16.91	75.8	85.6	73.8
(+5.8%)	(-1.9%)	(-0.7%)	(-2.9%)	(-0.1%)	(+0.4%)	(+7.9%)	(+13.8%)	(-1.8%)	(-3.1%)	(-1.3%)	(+2.3%)
9.70	9.80	19.64	78.6	87.0	71.2	-	-	-	(+0.5%)	(+0.3%)	(-1.2%)
-	-	-	(+0.5%)	(+0.3%)	(-1.2%)	-	-	-	(+0.5%)	(+0.3%)	(-1.2%)

Form III					
a	b	c	$\alpha$	$\beta$	$\gamma$
7.74	9.01	17.14	81.3	86.0	67.6
(+1.8%)	(+0.2%)	(-0.8%)	(-1.2%)	(-4.3%)	(+3.7%)

Form I					
a	b	c	$\alpha$	$\beta$	$\gamma$
7.99	7.77	17.12	73.65	88.5	82.03
(+3.0%)	(+0.4%)	(+1.0%)	(-5.4%)	0.00%	(-0.2%)

Form II					
a	b	c	$\alpha$	$\beta$	$\gamma$
8.04	8.42	17.11	75.9	86.6	72.4
(+5.8%)	(-1.9%)	(-0.7%)	(-2.9%)	(-0.1%)	(+0.4%)
8.20	9.76	16.91	75.8	85.6	73.8
(+7.9%)	(+13.8%)	(-1.8%)	(-3.1%)	(-1.3%)	(+2.3%)
9.70	9.80	19.64	78.6	87.0	71.2
-	-	-	(+0.5%)	(+0.3%)	(-1.2%)

Form III					
a	b	c	$\alpha$	$\beta$	$\gamma$
7.74	9.01	17.14	81.3	86.0	67.6
(+1.8%)	(+0.2%)	(-0.8%)	(-1.2%)	(-4.3%)	(+3.7%)

8.5% shear strain  $\epsilon_{xy}$

20% tensile strain  $\epsilon_y$

16% tri-axial tension

A combination of 12%  $\epsilon_{xy}$  and 3%  $\epsilon_{zy}$

### 4.3.2 Molecular Rotations Dominated Polymorphic Transition

Thermoelasticity underlies the reversible polymorphic transition of materials upon heating and cooling. Phase transitions in molecular crystals involve changes not only in the intermolecular packing but also in intramolecular conformations. To illustrate the complex structural transformation in molecular crystals, we construct a coordinate scheme shown in Figure 4.8A, where  $\vec{a}$ ,  $\vec{b}$ , and  $\vec{c}$  represent the lattice of the primitive cell, and  $\vec{u}$ ,  $\vec{v}$ ,  $\vec{w}$  dictate the molecular orientations. Specifically, the vector  $\vec{v}$  aligns with the molecular backbone direction,  $\vec{w}$  connects the molecular mass center with the Si atom in the side group, and  $\vec{u}$  is determined by the cross product of  $\vec{v}$  and  $\vec{w}$ .  $\omega$ ,  $\varphi$ , and  $\theta$  are three Euler angles characterizing the rotation of the molecule about the three orientation axes ( $\vec{u}$ ,  $\vec{v}$ , and  $\vec{w}$ ) with respect to its original orientations.

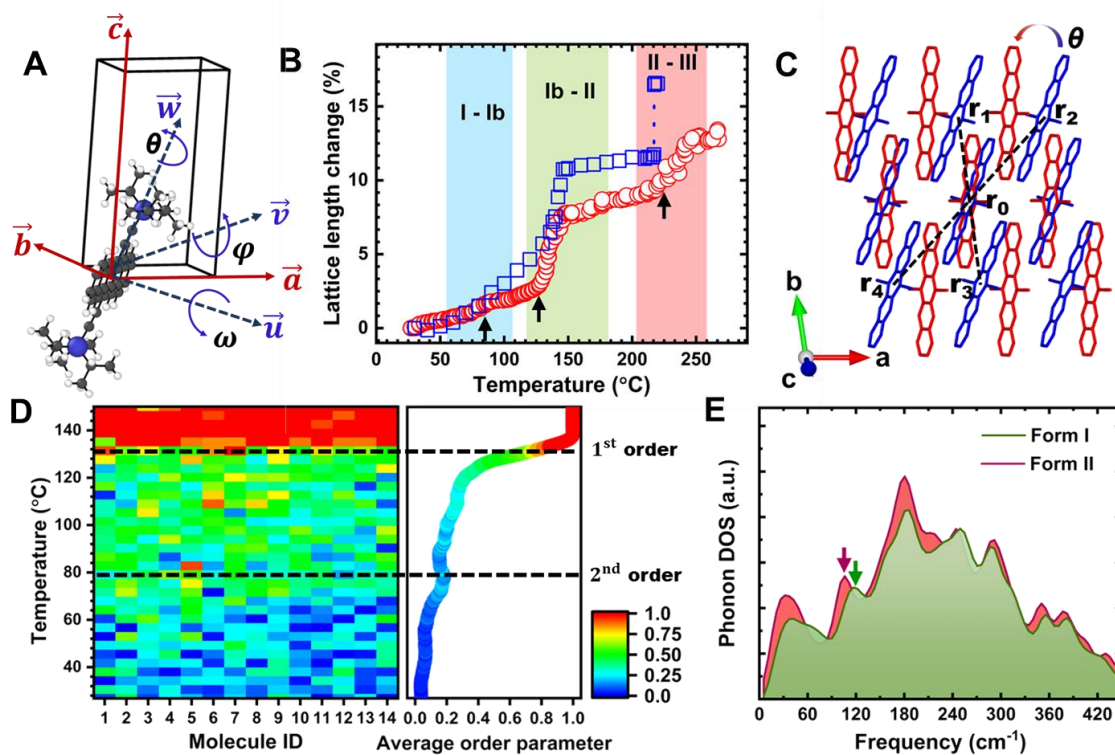


Figure 4.8. (A) A unit cell of the TIPS-pentacene molecular crystal. (B) The experimental (blue squares) and simulation (red circles) results of the change in the  $b$ -lattice parameter during heating. (C) Molecular crystal structures of Form I (blue) and Form II (red) show the angular rotation  $\theta$  of the molecular orientation in the  $ab$  plane. (D) Contour map of the order parameter of 14 molecules when temperature increases. The average order parameter demonstrates the 2<sup>nd</sup> order and 1<sup>st</sup> order phase transitions upon heating. (E) Phonon density of states show the phonon softening when the structure morphs from Form I (green curve) to Form II (red curve).

Our prior experiments of differential scanning calorimetry showed two first-order polymorphic transitions of TIPS-pentacene (i.e. Form I/Ib-to-Form II and Form II-to-Form III)<sup>19</sup> associated with the major changes in the lattice parameter  $b$  and the angle  $\gamma$ . To examine the underlying molecular mechanism, we adopt an evolutionary genetic algorithm to refine the molecular force field (*Simulation Methods*), which enables us to model the phase transitions of TIPS-pentacene under various thermal and mechanical loads. Figure 4.8B shows the experimental (blue squares) and simulation (red circles) results of the change in the  $b$ -lattice parameter during heating. The discrepancy of  $\sim 2\%$  in experiments and modeling for Forms II and III is not significant considering the limited model size ( $\sim 12$  nm in  $b$ ) used in the force field training. The abrupt increase of the  $b$ -lattice at 400K and 493K indicates the first-order phase transition of Form I/Ib-to-II and of Form II-to-III, respectively. Furthermore, a second-order transition of Form I-to-Ib is observed with a continuous change of the lattice parameter but a

discontinuity in the slope of the lattice parameter at  $\sim 353$ <sup>19</sup>. Since the two first-order transitions are similar, we focus on the phase transition of Form I-to-II within the temperature range of 300K~423K. An order parameter is desired to represent individual phases. We determine the order parameter based on the symmetry of the base-centered plane in the monoclinic lattice, consisting of a center molecule and four first nearest neighbor molecules (Figure 4.8C). The order parameter is defined as  $\xi_i = \frac{1}{2}(1 - \cos(\delta_i))$ , with  $\delta_i = \frac{\pi(\rho_i - \rho_l)}{\rho_h - \rho_l}$ ,  $\rho_i = (d_2 + d_4) - (d_1 + d_3)$ , where  $d_j$  refers to the distance between the center molecule ( $r_0$ ) and each neighbor molecule ( $r_j$ ), and  $\rho_l, \rho_h$  are calculated for the initial and final structures, respectively. Using the lattice structures obtained from XRD experiments, the  $\rho$  values for Forms I, II, and III are approximately 5.0, 2.0, and 0.0, respectively<sup>16</sup>. A smaller value of  $\rho$  denotes a more symmetric coordination environment around the center molecule. Therefore, the decreasing value of  $\rho$  from Form I to Form III indicates the increase of symmetry during the heating induced polymorphic transition. The order parameter  $\xi_i$  varies from 0 (blue) to 1 (red), corresponding to a polymorphic transition from the parent phase to the daughter phase (e.g. Form I-to- Form II transition). The lattice deformation is quantified by the deformation gradient matrix  $F$  transforming the original lattice coordinates ( $\vec{a}$ ,  $\vec{b}$ , and  $\vec{c}$ ) to the new coordinates ( $\vec{a}'$ ,  $\vec{b}'$ , and  $\vec{c}'$ ) in the deformed unit cell, which is calculated as  $F = \begin{bmatrix} 0.99 & -0.21 & 0.11 \\ -0.04 & 0.94 & -0.12 \\ 0.02 & 0.03 & 1.04 \end{bmatrix}$ . The deformation matrix shows that the lattice cell undergoes a shear deformation of -0.21 in the  $ab$  plane and a tilt of the  $c$  axis in the 3-dimensional space. The shear strain results in a reduction of  $9.6^\circ$  in  $\gamma$  between the vectors  $\vec{a}$  and  $\vec{b}$ , which is close to the experimental value of  $\gamma$  changing from  $82.2^\circ$  in Form I to  $72.1^\circ$  in Form II (Table 4.7). Meanwhile, the change in molecular orientation can be described by the Euler rotational angles. The Euler angles  $[\theta, \varphi, \omega]$  are calculated as  $[9.5^\circ, -1.6^\circ, 2.1^\circ]$ , where the major change of  $9.5^\circ$  in angle  $\theta$  arises from the counterclockwise molecular rotation about the  $\vec{w}$  axis. The result demonstrates that molecular rotation dominates the thermal induced phase transition from Form I to Form II.

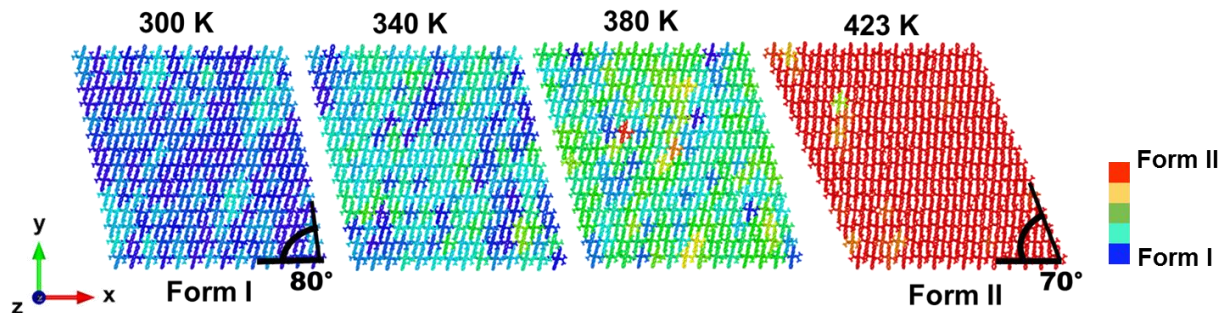


Figure 4.9. Molecular trajectories of Form I-to-II transition upon heating.

The polymorphic transition of Form I-to-II is accompanied by the homogeneous nucleation and growth of the daughter phase where the nuclei of Form II are randomly distributed within the parent Form I (Figure 4.9). Here we plot the evolution of the order parameter for 14 adjacent molecules in a row and the average order parameter of the whole supercell in Figure 4.8D. Within the temperature range of 300K~353K, most molecules are retained in Form I. Bypassing 353K, the green domain gradually dominates with a small bump in the average order parameter indicating the second-order phase transition. The abrupt jump of the average order parameter is observed at ~400K. A sharp green-to-red transition is observed in the contour map signifying the first-order transition of Form Ib to Form II.

Table 4.7. The simulated lattice parameters (red) agree well with the experimental data (blue). Their percentage differences are shown in the parentheses.

	<i>a</i>	<i>b</i>	<i>c</i>	$\alpha$	$\beta$	$\gamma$
<b>Form I</b>	7.76	7.74	16.95	77.8	88.5	82.2
	7.64	7.87	17.13	74.5	86.6	80.2
	(-1.5%)	(+1.7%)	(+1.0%)	(-4.3%)	(-2.2%)	(-2.4%)
<b>Form II</b>	7.60	8.58	17.23	78.2	86.7	72.1
	7.76	8.54	17.69	71.0	82.0	70.6
	(+2%)	(-0.4%)	(+2%)	(-9%)	(-5%)	(-2%)
<b>Form III</b>	7.60	8.99	17.27	82.2	89.9	65.2
	8.00	8.98	17.88	81.0	88.3	65.5
	(+5%)	(-0.1%)	(+3.5%)	(-1.4%)	(-1.8%)	(+0.5%)

### 4.3.3 Thermodynamics Analysis

Temperature-induced reversible martensitic transition involves the directional rotational motion of molecules. We try to understand this phenomenon from the point of view of thermodynamics and lattice dynamics.

**Transition energy barrier.** We explored the detailed energy landscape and energy barrier along the pathway of the phase transformation. For clarity, the thermodynamic quantities are derived from the Kohn-Sham energy functional<sup>20</sup>:

$$E[\{\phi(\vec{r})\},\{\vec{R}\}] = \sum_n \langle \phi_n^* \left| -\frac{\hbar^2 \nabla^2}{2m} + V(\vec{r}, \vec{R}) \right| \phi_n \rangle + E^H[\phi(\vec{r})] + E^{xc}[\phi(\vec{r})], \quad (4.5)$$

which includes the kinetic energy of electrons, the Hartree energy  $E^H$  for the electron-electron interaction, exchange-correlation functional  $E^{xc}$  between electrons, and external potential energy  $V$  of the ion-electron and ion-ion electrostatic interactions. At ground state (0K and no pressure), the system free energy is the total Kohn-Sham energy and is also regarded as the chemical potential energy of the molecule. At finite temperature in ab-initio molecular dynamics modeling, the system free energy includes the kinetic energy of ions:

$$U = E[\{\phi(\vec{r})\},\{\vec{R}\}] + \sum_i \frac{mv_i^2}{2}. \quad (4.6)$$

In the following description of the thermodynamic driving force and energy barrier of phase transition, we will exclude the temperature-induced kinetic energy from the system free energy to represent the intrinsic chemical potential energy of the molecule. Our preliminary results indicate that, in ab-initio molecule dynamics, the increase of the potential energy as temperature evolves is very close to the increase of the system kinetic energy, which might be resulted from the complex rotation, translation, and local vibration of atoms within the molecule. This finding is different from the modeling of closely-packed systems and should be carefully examined in future studies.

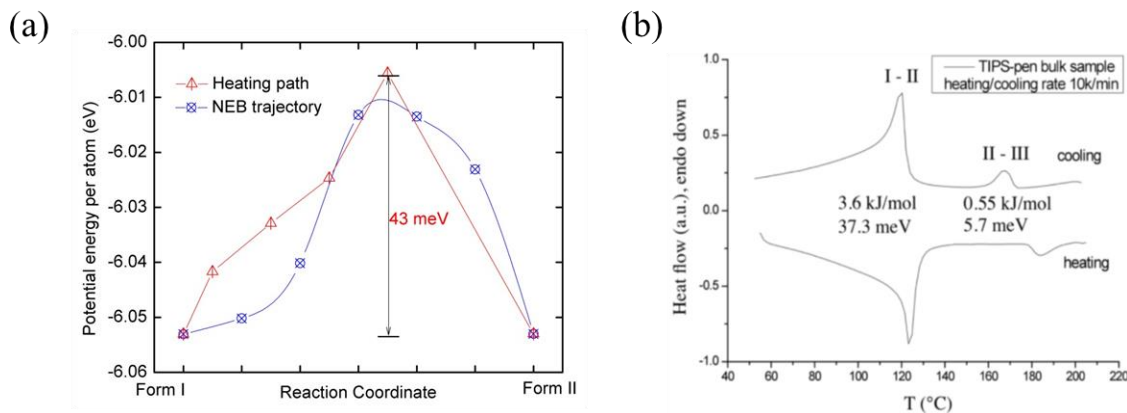


Figure 4.10. Energy barrier of Form I – II phase transition determined by AIMD and NEB calculations (a), and measured by differential scanning calorimetry experiments (b).

The structure search algorithm (*Simulation Methods*) allows us to capture the detailed structural evolution along the path of phase transitions. Figure 4.10(a) shows the chemical potential energies of intermediate configurations in the transformation from Form I to Form II during heating. The results are obtained using Vienna Ab-initio Simulation Package (VASP). Each reaction coordinate represents a molecular state of different degrees of rotational deformation of the  $\pi$ -backbone and relative displacive motion of side groups. In the AIMD modeling of the heating process (red curve), the most unfavorable configuration appears at the largest rotational angle of the backbone ( $\sim 11^\circ$ ) and the displacive motion of side group ( $\sim 0.7 \text{ \AA}$ ). The saddle point corresponds to a potential energy barrier of  $\sim 43 \text{ meV}$  per atom. We further employ the Nudged Elastic Band (NEB) calculations at the ground state (blue curve) to verify the AIMD modeling results. The intermediate configurations are constructed by linearly interpolating the lattice parameters  $b$  and  $\gamma$ , and the corresponding free energies are obtained by static relaxation. The energy barriers of the AIMD and NEB modeling are in great agreement. Figure 4.10(b) is a plot of the DSC results of the instant heat flow associated with the phase transitions of Forms I to II, and then II to III. The integrated areas of the heat flow with respect to the temperature give the energy barriers. The results indicate that the activation energies are  $\sim 37 \text{ meV}$  and  $\sim 5.6 \text{ meV}$  for Form I to Form II, and II to III transitions, respectively. The preliminary simulation results agree well with the DSC measurements.

**Lattice dynamics.** From a thermodynamics standpoint, a reduction of Gibbs free energy is necessary for the spontaneity of any type of phase transition. A polymorph is stabilized at a

certain temperature to minimize its total Gibbs free energy. We believe that the thermal-induced polymorphic transition in TIPS-pentacene is attributed to the trade-off relationships between the enthalpy and the vibrational entropy of Gibbs free energy. The three thermodynamic potential quantities are related via

$$G = H - TS. \quad (4.7)$$

wherein  $G$  is Gibbs free energy,  $H$  represents enthalpy,  $T$  is temperature, and  $S$  denotes entropy. We will demonstrate some preliminary simulation results. The enthalpy term can be fixed as the total potential energy obtained from the AIMD simulation at a given temperature and pressure. From previous AIMD simulation, we found the ground state free energy (not including any kinetics and entropy) of three polymorphs shows the incremental trend from Form I to Form III. Specifically, the ground state energy of Form I is 8 meV per atom lower than that of Form II while the energy of Form II is lower than that of Form III by 6meV per atom. That means, the Form I would be more thermodynamically stable than Form II and Form III at the ground state without considering any thermal effects. However, the contribution of the entropy term can't be ignored at an elevated temperature since high temperature will alter the zero-point energy and bring the kinetic energy and lattice vibrational energy. The entropy is relatively complicated to be calculated since it can't be directly extracted from DFT results. The entropy of a system mainly consists of two parts, configurational entropy, and vibrational entropy. The polymorphic transition has rare configurational entropy since the composition and atomic species don't change during the transition process. Thus the vibrational entropy contributes most, including both electronic vibrational entropy and phonon vibrational entropy. From DFT calculation, we learned that the electronic vibration entropy is negligible for the organic crystal. Then we will focus on the calculation of phonon vibrational entropy. The vibrational entropy can be deduced from harmonic phonon frequencies calculated at the optimized structure states. According to the lattice dynamics theory, the harmonic phonons are regarded as non-interacting quantum harmonic oscillators with angular frequencies  $\omega$ . Its partition function  $Z$  is derived as<sup>22</sup>:

$$Z = \frac{1}{1 - \exp(-\beta h \omega)} \quad (4.8)$$

where  $h$  is the reduced Planck constant and  $\beta$  equals to  $k_B T$ ,  $k_B$  is Boltzmann's constant.

The vibrational free energy is related to  $Z$  via

$$F = -k_B T \ln Z \quad (4.9)$$

From that, we can obtain

$$F = k_B T \sum_{k,\lambda} \ln[2 \sinh(\hbar\omega_{k,\lambda} / 2k_B T)] \quad (4.10)$$

In the above equation, the summation is over all vibrational modes, and all k-points in the reciprocal space,  $k$ . The vibrational entropy is taken as the first derivative of free energy with respect to the temperature. To make it computational accessible, instead of performing the summation operation over all vibrational modes and k-points, we introduce the phonon density of states and do the integrals in terms of angular frequency. The expression for the vibrational free energy can be replaced as<sup>23</sup>,

$$F = 3nNk_B T \int_0^{\omega_{\max}} \ln[2 \sinh(\hbar\omega_{k,\lambda} / 2k_B T)] g(\omega) d\omega \quad (4.11)$$

Accordingly, the vibrational entropy will be,

$$S = 3nNk_B T \int_0^{\omega_{\max}} \left[ \frac{\hbar\omega}{2k_B T} \coth\left(\frac{\hbar\omega}{2k_B T}\right) - \ln \left\{ 2 \sinh\left(\frac{\hbar\omega}{2k_B T}\right) \right\} \right] g(\omega) d\omega \quad (4.12)$$

The velocity autocorrelation function (VACF) method<sup>18</sup> is used to calculate PDOS. The supercells of Form I and Form II are firstly relaxed under NVT at 300K and then their VACF are calculated and spatially averaged over a 2 ps period under NVE for 10 times.

$$VACF(t) = \frac{\langle v(t) \cdot v(0) \rangle}{\langle v(0)^2 \rangle}. \quad (4.13)$$

PDOS  $g(\omega)$  is obtained by performing the Fourier transformation onto VACF with a frequency interval of  $5 \text{ cm}^{-1}$ . Figure 4.8E shows the comparison of the vibrational phonon density of states (PDOS) for Form I and Form II at the frequency region of 0~450  $\text{cm}^{-1}$ . A clear phonon softening is observed, where the PDOS of Form II is enhanced and shifted to the lower frequency regime. This result is consistent with the Raman spectrum experiment (Figure 4.11), which identifies the Form I-to-II transition by detecting the peak shift to the lower frequency regime. The phonon softening leads to an increase of 8.7 kcal/mol in the vibrational entropy (*Simulation Methods*), which is comparable to the value of 10 kcal/mol in our previous calorimetry measurements<sup>19</sup>. PDOS is contributed by both the intra- and intermolecular vibrations. The phonon softening usually correlates with the increase of the collective atomic

motions<sup>24,25</sup>, which may be attributed to the symmetry enhancement in the Form I-to-II transition that is promoted by the cooperative rotations of the conjugated backbone and side groups. Similar observation was reported in the martensitic transition of NiTi alloy, where the lower symmetry B19' is thermally transformed into the higher symmetry B2 phase accompanied by the phonon softening and entropy increase<sup>26</sup>.

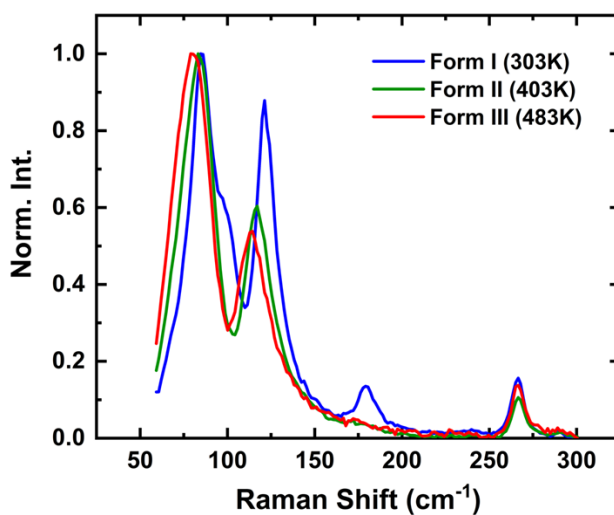


Figure 4.11. Raman spectrum for different polymorphs under their equilibrium temperatures.

#### 4.4 References

1. Ghosh, S.S.; Reddy C.M., *Angew. Chem., Int. Ed.*, **2012**, *51*, 10319– 10323.
2. Worthy, A.; Grosjean, A.; Pfrunder, M.C.; Xu, Y.; Yan, C.; Edwards, G.; Clegg, J.K.; McMurtrie, J.C., *Nat. Chem.*, **2018**, *10*, 65– 69.
3. Panda, M.K.; Ghosh, S.; Yasuda, N.; Moriwaki, T.; Mukherjee, G.D.; Reddy, C.M.; Naumov, P., *Nat. Chem.*, **2015**, *7*, 65-72.
4. Ahmed, E.; Karothu, D.P.; Warren, M.; Naumov, P., *Nat. Commun.*, **2019**, *10*, 1-9.
5. Liu, H.; Lu, Z.; Tang, B.; Qu, C.; Zhang, Z.; Zhang, H., *Angew. Chem. Int. Ed.*, **2020**, *59*, 12944.
6. Worthy, A., Grosjean, A., Pfrunder, M.C., Xu, Y., Yan, C., Edwards, G., Clegg, J.K., McMurtrie, J.C., *Nat. Chem.*, **2018**, *10*, 65.
7. Wollants, P.; De Bonte, M.; Roos, J., *Z. Metallkd.* **1979**, *70*, 113-117.
8. Mei, J.; Diao, Y.; Appleton, A.L.; Fang, L.; Bao, Z., *J. Am. Chem. Soc.*, **2013**, *135*, 6724-6746.
9. Diao, Y.; Tee, B.C.; Giri, G.; Xu, J.; Kim, D. H.; Becerril, H.A.; Stoltenberg, R.M.; Lee, T.H.; Xue, G.; Mannsfeld, S.C., *Nat. Mater.*, **2013**, *12*, 665-671.
10. Diao, Y.; Lenn, K.M.; Lee, W.Y.; Blood-Forsythe, M.A.; Xu, J.; Mao, Y.; Kim, Y.; Reinspach, J.A.; Park, S.; Aspuru-Guzik, A. and Xue, G.; Clancy, P.; Bao, Z.; Mannsfeld, S.C., *J. Am. Chem. Soc.*, **2014**, *136*, 17046-17057.
11. Kresse, G.; Furthmüller, J., *Phys. Rev. B*, **1996**, *54*, 11169.
12. Kresse, G.; Joubert, D., *Phys. Rev. B*, **1999**, *59*, 1758.
13. Jorgensen, W.L., Maxwell, D.S., Tirado-Rives, J., *J. Am. Chem. Soc.*, **1996**, *118*, 11225-11236.
14. Frisch, M.; Trucks, G.; Schlegel, H.; Scuseria, G.; Robb, M.; Cheeseman, J.; Scalmani, G.; Barone, V.; Mennucci, B.; Petersson, G., Gaussian 09 Package. Gaussian, Inc.: Wallingford, CT, USA **2009**.
15. Plimpton, S.; Crozier, P.; Thompson, A., *Sandia National Laboratorie* , **2007**, *18*, 43-43.
16. Park, S. K.; Sun, H.; Chung, H.; Patel, B. B.; Zhang, F.; Davies, D. W.; Woods, T. J.; Zhao, K.; Diao, Y., *Angew. Chem. Int. Ed.*, **2020**, *59*, 13004.
17. Li, Y.; Li, H.; Pickard IV, F.C.; Narayanan, B.; Sen, F.G.; Chan, M.K.; Sankaranarayanan, S.K.; Brooks, B.R.; Roux, B., *J. Chem. Theory. Comput.*, **2017**, *13*, 4492-4503.
18. Li, J.; Tomkinson, J., *Theoretical and Computational Chemistry*, Elsevier, Amsterdam, **1999**, 471-532.
19. Chung, H., Dudenko, D., Zhang, F., D'Avino, G., Ruzié, C., Richard, A., Schweicher, G., Cornil, J., Beljonne, D., Geerts, Y., *Nat. Commun.*, **2018**, *9*, 278.

20. Kresse, G., Furthmüller, J., *Comput. Mater. Sci.*, **1996**,*6*, 15-50.
21. Purdum, G.E., Yao, N., Woll, A., Gessner, T., Weitz, R.T., Loo, Y.L., *Adv. Func. Mater.*, **2016**, *26*, 2357-2364.
22. Dove, M., *École thématique de la Société Française de la Neutronique*, **2011**,*12*, 123-159.
23. Hua, G.; Li, D., *Rsc Adv.*, **2015**, *5*, 103686-103694.
24. Nyman, J.; Day, G.M., *CrystEngComm*, **2015**, *17*, 5154-5165.
25. Zhang, F.; Wang, H.W.; Tominaga, K.; Hayashi, M., *J. Phys. Chem. B*, **2016**, *120*, 1698-1710.
26. Bogdanoff, P.D.; Fultz, B.; *Philos. Mag. B*, **2007**, *81*, 299-311.

## CHAPTER 5. SUPER- AND FERROELASTIC TRANSITION IN ORGANIC SEMICONDUCTOR CRYSTALS

This chapter is based, in part, on the research described in the following publications

**Sun, H.;** Park, S. K.; Diao, Y.; Kvam, E. P.; Zhao, K., “Molecular Mechanisms of Superelasticity and Ferroelasticity in Organic Semiconductor Crystals” *submitted, 2020.*

Park, S. K. †; **Sun, H.** †; Chung, H.; Patel, B. B.; Zhang, F.; Davies, D. W.; Woods, T. J.; Zhao, K.; Diao, Y., *Angew. Chem. Int. Ed.*, **2020**, *59*, 13004. (†: denotes equal contribution)

### 5.1 Introduction

Organic crystals were deemed still and brittle. Such perception has been defied by the recent reports of flexible and bendable organic crystals<sup>1-5</sup>. The emergence of the unconventional phenomena in organic solids, such as rapid shape reconfiguration induced by heat, pressure, or light, attracts enormous interest from solid state chemists to produce light, biocompatible, and environmentally benign devices<sup>5-9</sup>. The flexibility of organic crystals has been presented by the several studies, wherein researchers demonstrated highly bendable organic crystals through either elastic or plastic deformation<sup>1,3</sup>. More intriguingly, Takamizawa et al. demonstrated terephthalamide crystal<sup>10</sup> and 4,4'-dicarboxydiphenyl ether crystals<sup>11</sup> which can withstand large deformation while retaining structural integrity through either polymorphic transitions or lattice reorientations. Such characteristics are reminiscent of superelasticity and ferroelasticity in shape-memory alloys – in superelasticity, the daughter phase becomes unstable and the initial mother phase reemerges upon releasing the stress<sup>12,13</sup>, while ferroelasticity is typically facilitated by lattice reorientation and the structure recovers the original shape upon loaded in an opposite direction<sup>14</sup>. Deformable organic crystals have recently incurred vast attention in crystal engineering and pharmaceutical engineering<sup>15-17</sup>. Nevertheless, most of those organic solids comprising simple hydrocarbon groups, albeit intriguing, are limited by their functionalities.

Molecules and polymers with extended  $\pi$ -conjugation warrant intensive studies in the emerging field of organic semiconductors owing to their effective charge transferability and solution processability. They are now actively pursued in the development of flexible and printed devices, such as solar cells, light-emitting diodes, field-effect transistors, sensors, wearable

devices, and electronic skins<sup>18,19</sup>. Chung et al. reported thermoelasticity and shape memory in two molecular organic semiconductors, ditBu-BTBT and TIPS-pentacene<sup>20</sup>. Thermally triggered rapid cooperative phase transition and associated shape and function memories were observed for both molecules within seconds. Lately, we unveiled super- and ferroelasticity in TIPS-pentacene crystal which can tolerate a tensile strain of over 13 % while maintaining the high charge carrier mobility<sup>21</sup>. This finding provides a pathway to achieve the ultraflexible high-performance single-crystal organic electronics. To harvest the superelastic deformability in organic crystals, especially in the semiconducting organic crystals, profound mechanistic understanding of cooperative transitions is imperative to develop principles of molecular design. In experiments, X-ray characterization and Raman spectroscopy can help examine the static crystallographic relations of different polymorphs. However, the intricate dynamics of the molecular structure during the polymorphic transitions challenges a direct experimental observation as such events occur in an extremely short time scale (usually within seconds). To this end, molecular level understanding is desired to scrutinize the dynamic changes of the packing structure upon the cooperative transitions. By employing molecular dynamics simulations, Cuppen et al. pointed out that the local fluctuation in the conformation of the aliphatic chains gave rise to the temperature induced polymorphic transition of DL-norleucine crystals<sup>15</sup>. Complementing Chuang's experimental work, Geerts et al. provided the simulation evidence of rotating side chains in the thermoelastic transition of semiconducting ditBu-BTBT materials<sup>20</sup>. In our recent work, we revealed that the cooperative rotational and displacive molecular motions facilitated the super- and ferroelasticity in TIPS-pentacene crystals using ab-initio modeling and molecular simulation<sup>21</sup>. However, the concepts of "local fluctuation" and "cooperative rotational and displacive motions" are not sufficient to populate the vacant knowledge space regarding the kinetics and energetics of the thermo-, super-, and ferroelastic transitions in conjugated molecules.

Superelasticity and ferroelasticity are well documented in metallic alloys and materials theories have been well developed to guide the design of shape memory alloys<sup>12-14</sup>. Although the cooperative transitions of organic solids involve complicated conformational changes due to the intricate intra- and intermolecular interactions, they share a few common features of homogenous lattice deformation in the martensitic transitions in metals and ceramics. Here we transfer the prior knowledge about the phase descriptor and phenomenological theories of

martensitic transition in metallurgy<sup>13</sup> to the organic system. With the aid of genetic algorithm refined atomistic modeling (*Simulation Methods in Chapter 4*), we systematically investigate the thermo-mechanically induced cooperative transitions in TIPS-pentacene semiconductors. Figure 5.1 sketches a phase diagram in the space of thermal (T-axis) and mechanical ( $\sigma$ - $\epsilon$  plane) load. The reversible polymorphic transition can be regulated by the change of temperature through thermoelasticity. The high-temperature (HT) phase transforms to the low-temperature (LT) phase via superelasticity under a shear load ( $\sigma$ - $\epsilon$  plane). The LT phase deforms through ferroelasticity and deformation twinning. Different types of superelasticity and ferroelasticity can be triggered by prescribing load in different directions. The twinned domains can also revert to their original orientation by reverse mechanical load or thermal treatment. The thermal induced polymorphic transitions (i.e. thermoelastic transitions) manifested by molecular rotations have been intensively discussed in *Chapter 4*. Herein, we will particularly focus on investigating the mechanically induced superelastic and ferroelastic transitions in the space of stress and strain loads. We demonstrate the cooperative molecular motions in superelastic and ferroelastic transitions, the interconvertible behavior of super- and ferroelasticity, diffusive interface in superelastic transition, and molecular defects of disclination dipoles and stacking faults in the twinning process. The theoretical framework integrating both lattice crystallography and molecular motions can find use in analyzing the mechanisms of homogeneous cooperative transitions in a variety of organic solids, especially in the conjugated semiconducting materials. The comprehensive molecular understanding will help open new avenues for rapid, reversible modulation of electronic and optical properties in organic crystals by means of molecular selection and design.

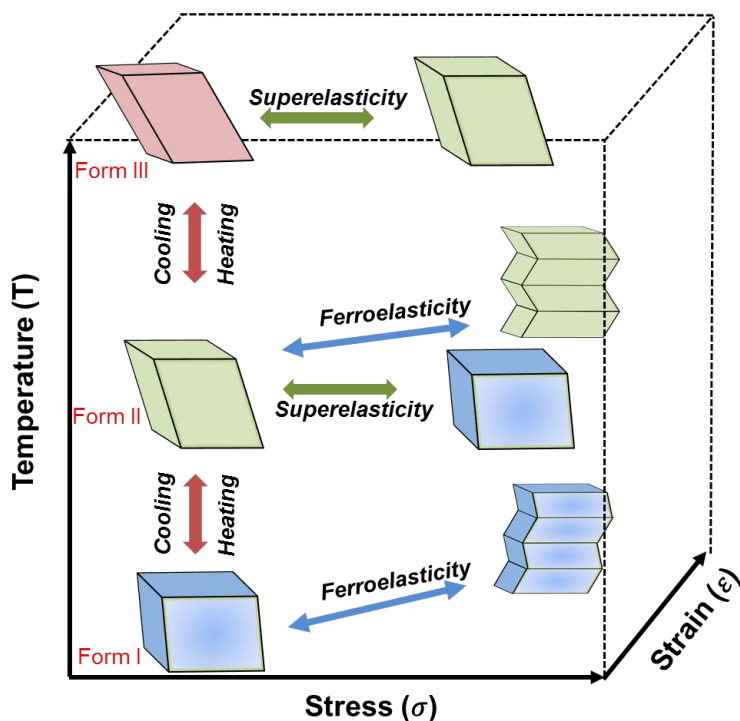


Figure 5.1. A sketch of the phase diagram of the TIPS-pentacene semiconductor crystal in the space of temperature-stress-strain exhibiting thermoelasticity (TE), superelasticity (SE), and ferroelasticity (FE).

## 5.2 Simulation Methods

### 5.2.1 Ab-initio Molecular Dynamics

The superelastic transition is investigated by applying the DFT simulation onto the  $2 \times 2 \times 1$  supercell. The supercell model, containing 400 atoms (four molecules), is built by expanding the optimized unit cell obtained from the *Structure Searching* part (*Chapter 4*). The calculations are carried out based on the hybrid Gaussian and plane waves scheme implemented in the CP2K package<sup>22</sup>. The DZVP molecularly optimized basis sets<sup>23</sup> and a 400 Ry cutoff auxiliary plane-wave basis set<sup>24</sup> are employed, with accompanying Goedecker–Teter–Hutter pseudopotentials<sup>25</sup>. The exchange and correlation term is treated by the PBE functional with the DFT-D3 correction<sup>26</sup>. The shear-induced superelastic transition I from Form II to Form I at  $127^\circ\text{C}$  (SE-I) and superelastic transition II from Form III to Form II at  $227^\circ\text{C}$  (SE-II) are accomplished by the ab-initio Molecular Dynamics (AIMD) simulation with the aid of the quasi-static loading algorithm. Basically, we apply incremental 1% shear strain  $\epsilon_{xy}$  onto the supercell model at each step, and afterward, the model undergoes the ab-initio molecular dynamics in the canonical ensemble NVT for 2 ps at each strained state. After that, the lattice structure of a new phase obtained from

the dynamic transition will be fully relaxed and optimized until the atomic displacements are lower than  $1.6 \times 10^{-4}$  nm and forces on the atoms are smaller than 0.23 eV/nm. The recovery process of the superelastic transition is conducted by applying the reverse shear strain of -1% at each step followed by the successive ab-initio molecular dynamics in a similar manner as that of the loading process. The lattice parameters of all polymorphs calculated in the cyclic shear loading have an excellent comparison with the experimental measurements shown in Table 5.1. The temperature is controlled using the generalized Langevin thermostat with the time step of 0.5 fs and all periodic boundary conditions are adopted in the DFT simulation.

Table 5.1. The six lattice parameters of three polymorphs in the shear stress-induced SE-I (left panel) and SE-II (right panel) agree well with the experimental data. The percentage differences between simulation and experimental data are shown in the parentheses.

	a	b	c	$\alpha$	$\beta$	$\gamma$		a	b	c	$\alpha$	$\beta$	$\gamma$	
<b>Form II</b>	7.58	8.49	17.84	75.9	88.7	70.8		<b>Form III</b>	7.74	9.01	17.14	81.3	86.0	67.6
	(-0.3%)	(-1.0%)	(+3.5%)	(-2.9%)	(+2.3%)	(-1.8%)			(+1.8%)	(+0.2%)	(-0.8%)	(-1.2%)	(-4.3%)	(+3.7%)
↓	Shear loading							↓	Shear loading					
<b>Form I</b>	7.53	7.90	16.84	74.1	87.0	79.6		<b>Form II</b>	7.51	8.63	17.21	79.5	86.3	72.0
	(-3.0%)	(+2.1%)	(-0.6%)	(-4.9%)	(-1.7%)	(-3.2%)			(-1.2%)	(+0.6%)	(-0.1%)	(+1.7%)	(-0.5%)	(-0.1%)
↓	Unloading							↓	Unloading					
<b>Form II</b>	7.58	8.44	17.92	75.8	87.2	71.3		<b>Form III</b>	7.74	9.06	17.54	81.2	85.8	66.6
	(-0.3%)	(-1.6%)	(-4.0%)	(-3.1%)	(+0.6%)	(-1.1%)			(+1.8%)	(+0.8%)	(+1.5%)	(-1.3%)	(-4.5%)	(+2.2%)

## 5.2.2 Molecular Dynamics

The large scale molecular dynamics is employed to investigate the ferroelasticity. The simulation is carried out using the molecular dynamics software LAMMPS package<sup>27</sup>. The OPLS-AA force field<sup>28</sup> is adopted to describe the potential environment in the TIPS-P crystal. The process of re-parameterized OPLS-AA force field has been detailed in the *Simulation Methods* in Chapter 4. Two types of ferroelasticity are examined by applying different loading conditions at 27°C. The model used in MD simulation for the ferroelasticity is built by expanding the lattice structure obtained from DFT calculation. The triclinic supercell has a size of 19.2 nm × 49.2 nm × 1.6 nm (along the X,Y and Z directions) and three tilt factor of  $xy = -7.33$  nm,  $xz = 0.06$  nm,  $yz = -0.48$  nm, containing 140800 atoms. The lattice structure is energetically minimized and then fully relaxed under the NPT ensemble at 27°C and zero pressure for 0.5 ns. For FE-I, a constant shear engineering strain rate of 0.02% per picosecond

along the  $x$ -direction is applied to the supercell model by changing the tilt factor of  $xy$  under NVT ensemble. For FE-II, the  $y$ -direction tensile load is employed under NPT ensemble with a tensile engineering strain rate of 0.02% per picosecond, while the  $x$  length is allowed to shrink to preserve the product of  $x$  and  $y$  length as constant. The shear stress and shear strain along the  $[\bar{1}20]$  direction in FE-II are calculated by performing the resolved plane stress/strain analysis<sup>29</sup> illustrated in Figure 5.2. The recovery process is conducted by applying the reverse shear/tensile strain with an engineering strain rate of -0.02% until the resultant strain is reduced to zero. The periodic boundary conditions are applied to all three directions. The temperature and pressure are controlled using the Nosé–Hoover thermostat and barostat with a time step of 0.1 fs.

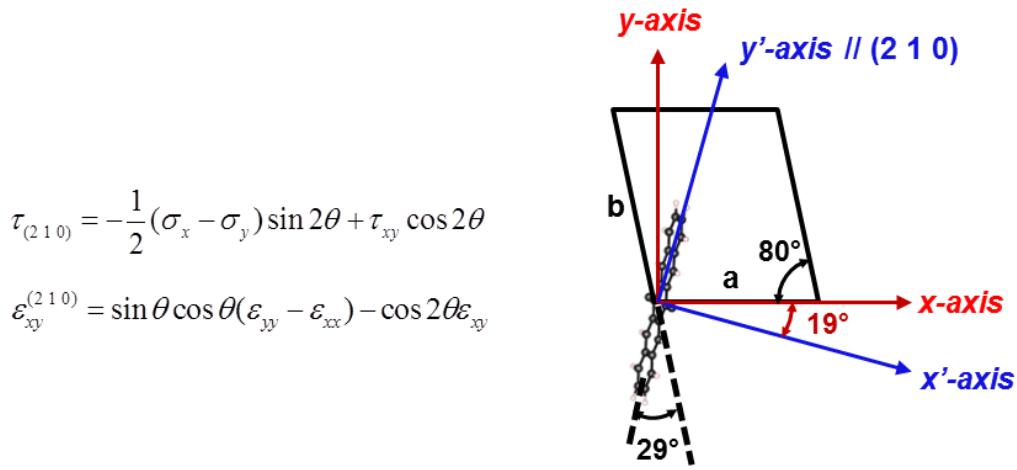


Figure 5.2. The resolved shear stress and shear strain at (210) plane in FE-II are calculated based on the above equations (left). Here the value of  $\theta = 19^\circ$  is deduced from the analysis of geometric relations (right), where  $\theta = 90^\circ - (180^\circ - 80^\circ - 29^\circ)$ . The lattice angle  $\gamma$  is  $80^\circ$  for Form I and the angle between the  $b$  axis and (210) plane (along backbone direction) is  $29^\circ$ . The stress and strain components  $\sigma_x$ ,  $\sigma_y$ ,  $\tau_{xy}$ ,  $\varepsilon_{xx}$ ,  $\varepsilon_{yy}$ ,  $\varepsilon_{xy}$ , are all obtained from MD simulation of FE-II.

### 5.2.3 Structural Descriptor and Order Parameter

To investigate the molecular evolution of deformation twinning in ferroelasticity, it's vital to have the appropriate structural descriptor to identify different polymorphs. The determination of the structural descriptor for TIPS-P molecular crystal is illustrated as below. Firstly, the “point molecule” scheme is used to extract the basic geometric information of one isolated TIPS-P molecule. As shown in Figure 5.3a, the center of mass position of the molecule is regarded as the origin and is labeled as  $r$ . The vector from the origin to the Si atom in the side group defines the  $z'$ -axis and the vector from the origin to the center of an adjacent aromatic ring is the  $y'$ -axis. The cross-product of the two vectors gives the direction of the  $x'$ -axis, which is perpendicular to the

pentacene backbone plane. Next, we need to find the appropriate parameter to characterize the coordination environment of one molecule. From Figure 4.1, we have learned that the major differences in the lattice structures of three polymorphs are the lattice length along  $b$ -axis and the lattice angle of  $\gamma$ . Those two lattice parameters are mainly associated with the molecular arrangements in the  $ab$  plane. Thus the structural descriptor is defined based on the molecular neighbor symmetry in one  $ab$  plane layer as depicted in Figure 5.3b. Each molecule has four nearest-neighbor molecules with the center of mass  $r_i$ . The four center-of-mass distances can be defined as

$$d_i = |r_i - r_0|, i=1,2,3,4 \quad (5.1)$$

According to the molecular symmetry, the center-of-mass distances are related as:  $d_1 = d_3$ ,  $d_2 = d_4$ . At equilibrium states, the  $(d_2 - d_1)$  (or  $d_4 - d_3$ ) for Form I, Form II and Form III are 2.5, 1.0 and 0.0, respectively. Considering the center-of-mass position always fluctuates due to the thermal effects, the quantity of  $\rho = (d_2 + d_4) - (d_1 + d_3)$  is used as the structural descriptor for one TIPS-P molecule. During MD simulation of twinning deformation, the  $(d_2 + d_4) - (d_1 + d_3)$  is reducing from the average value of 5 to 0, corresponding to the phase transition from Form I to Form III. After that, the structural descriptor  $\rho$  turns to be negative up to the average value of -5 which is identified as twinned Form I. In the twinned Form I, the  $[\bar{1}10]$  axis (along  $d_2$  direction) and  $[010]$  axis (along  $d_1$  direction) swap so that the structural descriptor  $\rho$  is reduced to the value of -5. The switching of these two lattice vectors is also confirmed by the experimental measurements.

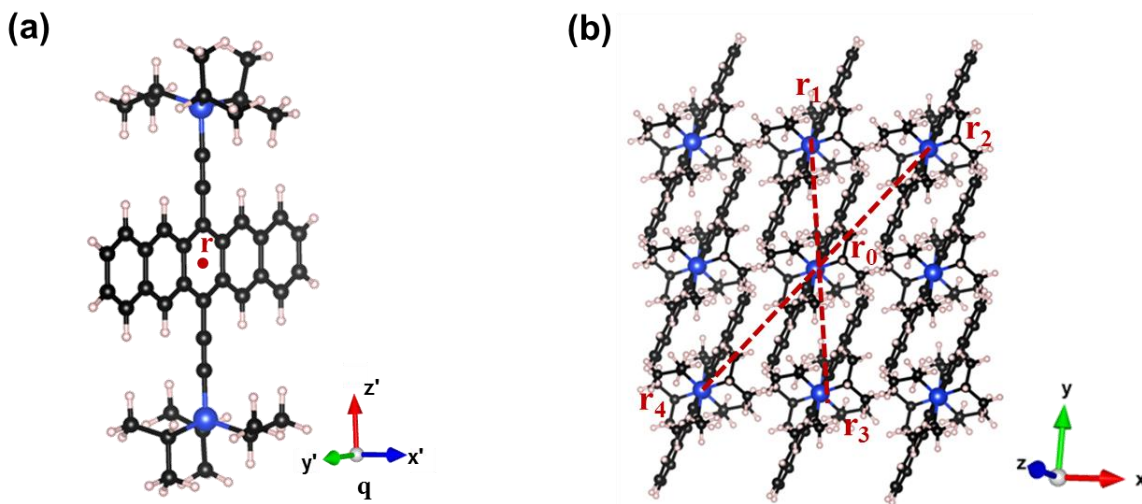


Figure 5.3. **a** The point molecule scheme of TIPS-P. **b** The center-of-mass distances between the center molecule and its four nearest neighbor molecules used to define the structural descriptor.

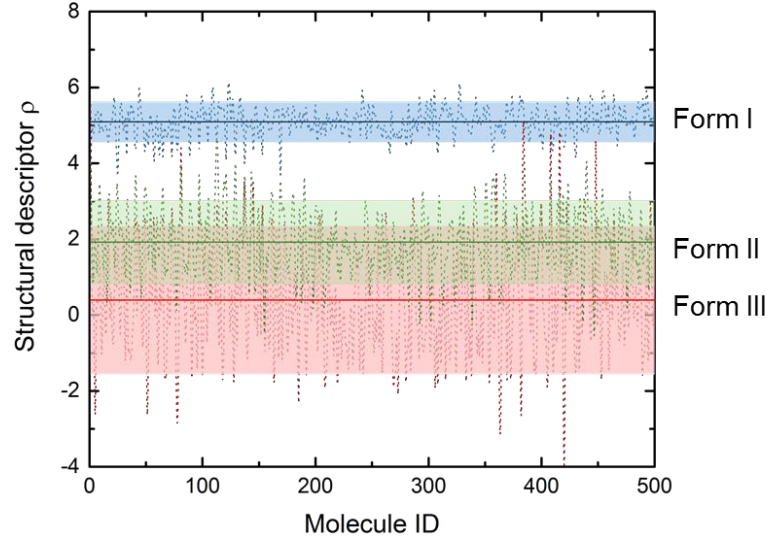


Figure 5.4. The value of structural descriptor  $\rho$  of each molecule in the  $24 \times 24 \times 1$  superlattice of three polymorphs at the equilibrium states of MD simulation in the canonical NVT ensemble at  $27^\circ\text{C}$ . Each solid line represents the mean value of all calculated structural descriptors (black dots) with the standard deviation shown in the shaded area for each polymorph.

To characterize the smooth transition of twinning deformation in MD simulation, the order parameter is proposed as below with the structural descriptor as inputs.

$$\xi_\rho = \begin{cases} 0 & \rho_i \geq \rho_h \\ \frac{1}{4}(1 - \cos(w_i)) & \rho_l < \rho_i < \rho_h \\ 0.5 & -\rho_l \leq \rho_i \leq \rho_l \\ 1 - \frac{1}{4}(1 - \cos(w_i)) & -\rho_h < \rho_i < -\rho_l \\ 1 & \rho_i \leq -\rho_h \end{cases}, \text{ with } w_i = \frac{\pi(|\rho_i| - \rho_h)}{\rho_l - \rho_h} \quad (5.2)$$

In the above equation,  $\xi_\rho$  is the order parameter for a given structural descriptor  $\rho_i$ . The  $\cos(w_i)$  function is chosen so that its derivative is zero at  $\pm\rho_l$  and  $\pm\rho_h$  shows a smooth transition between those values. The value of  $\rho_h$  is selected as 4.5 which is slightly smaller than the equilibrium value of 5.0 of Form I while the value of  $\rho_l$  is determined as 2.0 to indicate the formation of the intermediate phase (Form III). Those values are chosen to reduce the effects of normal thermal vibrations of molecules around their equilibrium states. Figure 5.4 illustrates the

variation of the structural descriptor  $\rho$  of each molecule in three polymorphs resulting from the thermal vibrations at 27°C. Specifically, for Form I, the number of  $\rho$  vibrates around 5.0 with a small deviation value of 0.5. Thus the molecules with the structural descriptor higher than 4.5 will be regarded as Form I. Form II has the mean value of 2.0 with a standard deviation of 1.0 while the average  $\rho$  value of Form III is around 0.0 with a large deviation of 2. The thermal vibrations of the structural descriptors indicate that the thermodynamic stability of Form I is much better than that of Form II and Form III at 27°C. Besides, the range of the structural descriptors of Form II and Form III overlap so that the transition from Form II to Form III can easily happen. Thus the intermediate phase appearing in the twinning transition is simply identified as Form III phase which may override the possibility of mixed Form II and Form III phases. The color coding of MD simulation scenarios is done by calculating the order parameter for each molecule, ranging from 0 (green) to 1 (blue). The green represents the original Form I, red stands for the intermediate Form III, and blue represents the twinned Form I.

## 5.3 Results and Discussion

### 5.3.1 Superelasticity, Ferroelasticity and Cooperative Molecular Motions

#### 5.3.1.1 Superelasticity

On a small scale, the stress-induced superelastic transitions among three polymorphs are captured by the AIMD modeling with the aid of the quasi-static loading algorithm (described in the *Simulation Method*). Figure 5.5(a) demonstrates the molecular motion (from the z-axis view) of the complete superelastic transition induced by temperature and shear loading. The rotational changes in molecular orientation along the z-axis can be easily observed. Figure 5.5(b) interprets the molecular motion for SE-I transition in detail. The upper panel shows the relative displacive motion of the backbone in the b-axis. Upon applying the shear strain 6%, the relative displacement of the front and the back molecules becomes obvious. The displacive mismatch between the center of the backbone and side groups increases with shear strain. Bypassing a critical molecular shear displacement, the mismatch strain decreases, and eventually an ordered Form I emerges as shown in the last snapshot in the upper panel. The lower panel in Figure 5.5(b) shows the rotational deformation of the backbone and side groups about the c-axis in the

clockwise (CW) direction, which complements the displacive motion and accommodates the phase transition.

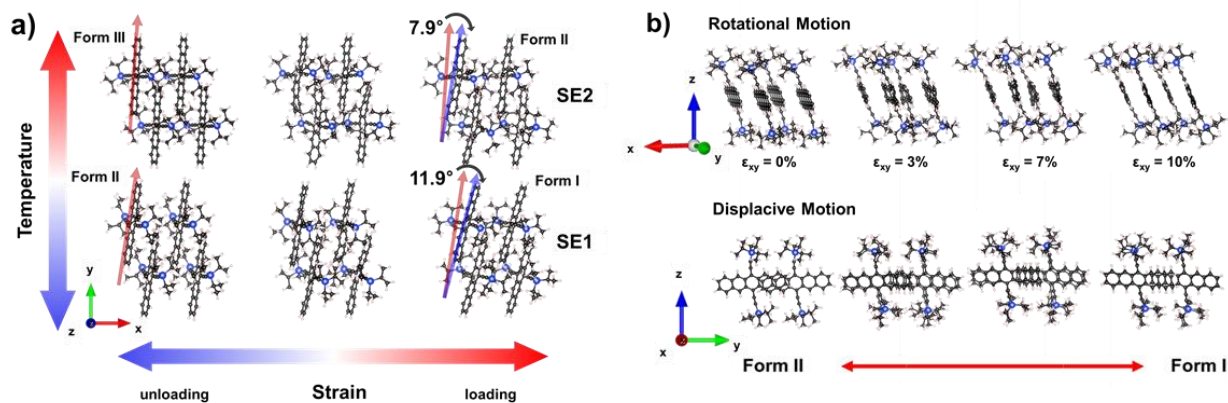


Figure 5.5. (a) AIMD modeling of superelastic transition induced by temperature or shear strain. (b) molecular motions of superelastic transition at 400K

We can compare the rotational angles in different polymorphs with experimental measurements by Polarized Raman Spectroscopy. The molecular rotations can be described by the point-molecule-representation as discussed earlier. For example, the relative rotational angle between Form I and Form II is determined as follows,

$$\phi_{I,II} = \phi_{y,b}^I - \phi_{y,b}^{II} + \gamma_2 - \gamma_1, \quad \phi_{y,b}^{I,II} = \cos^{-1}(\vec{y} \cdot \vec{b}) \quad (5.3)$$

where  $\phi$  stands for the angular difference between the y-axis (backbone direction) in the (210) lattice plane and the b-axis of the lattice in the (100) plane.  $\gamma$  for different polymorphs are shown in Figure 4.1.

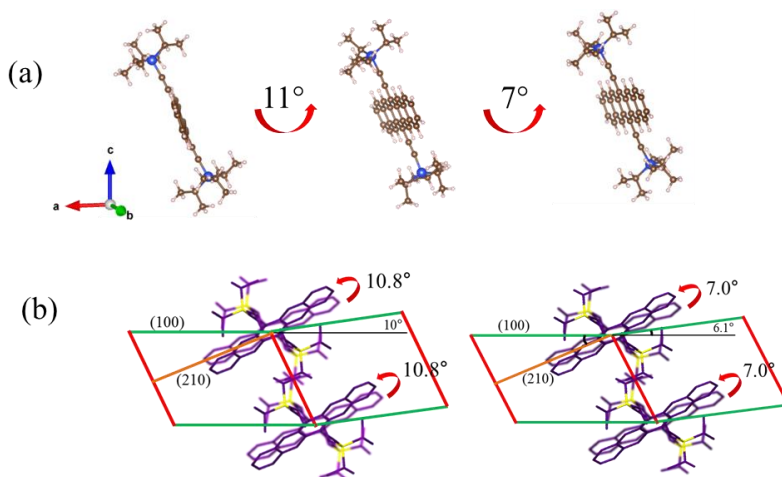


Figure 5.6. (a) The rotational angle of the backbone when the polymorphs evolve from Form I to Form II, and then to Form III. (b) The experimental determination of the relative orientation between the polymorphs.

Figure 5.6(a) shows the relative orientation of three polymorphs in Tips-pentacene. The backbone rotates CCW by  $11^\circ$  to form Form II (middle) and further rotates CCW by  $7^\circ$  to generate Form III (right). Figure 5.6(b) illustrates the experimental results of the molecular orientations at the phase boundaries of Forms I-II (left) and Forms II-III (right). The angular differences are in great agreement with the simulations. Figure 5.7 plots the stress-strain curves of SE-I and SE-II with the small hysteresis. The calculations are done by applying the 0.2% incremental shear strain onto the  $2 \times 2 \times 1$  supercell model at each step followed by the static geometric optimization. The unloading recovery is conducted by applying the reverse shear strain of -0.2% at each step up to the corresponding stress is reduced to zero.

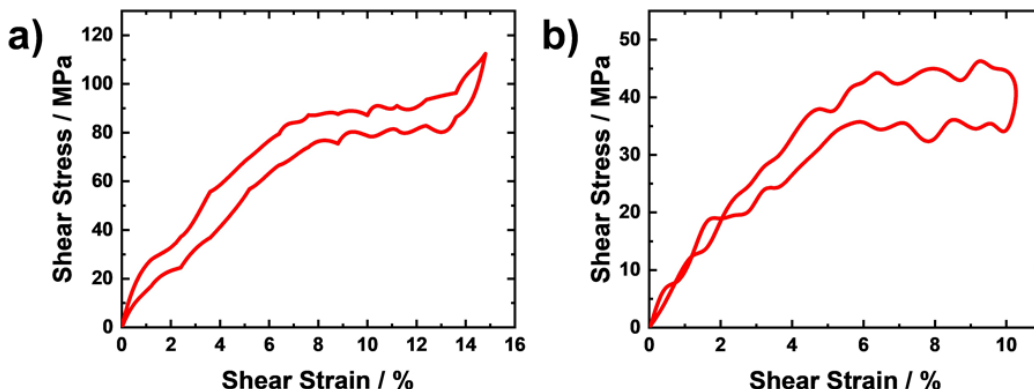


Figure 5.7. The DFT calculated strain-stress curves for **a** SE-I and **b** SE-II transitions by the static shear loading.

### 5.3.1.2 Ferroelasticity

The underlying mechanisms of the ferroelastic transitions and their atomic-level dynamics are revealed by molecular dynamics. The details about the simulation settings have been described in the *Simulation Method*. Figure 5.8 shows six representative structural configurations during molecular dynamics simulation of FE-I transition by  $[100]$  shearing (x-axis) at 300K (Figure 5.8(a)), and their corresponding stress-strain loop (Figure 5.8(b)). From configuration **i** to **ii**, Form-I structure firstly undergoes linear elastic deformation while the intermediate phase gradually appears in several regions. After the onset (**ii**), the twinned phase appears and grows (up to configuration **v**) resulting in a significant stress release indicated by a large drop in the stress-strain curve. The twining transition involves two stages. The first stage is characterized by

the rapid growth of the twinning zone, causing the stress decays linearly in the stress-strain loop. Figure **iii** is one of the representative configurations in the first stage. After that, the twinning phase grows very slowly so that the associated stress reaches the steady plateau as shown in the stress-strain curve. Then, by applying the opposite shear loading, the twinned phase gradually recovers back to the original structure as depicted in the configuration **v-vii**. A large stress hysteresis observed in the total stress-strain curve indicates the stress releasing mechanism of the martensitic transition. Different from the stress-strain curve for the traditional shape memory alloy or ceramics, the stress will have a substantial drop by achieving the twinning transition instead of going through a transition plateau. It may result from the rotational molecular motion which is parallel to the shear stress direction. During the shear loading, the molecules will firstly glide systematically along the shear direction with little changes in the molecular orientation to accommodate the elastic shear strain. In some red regions, the molecules rotate CCW to certain degrees, and also the molecule neighbor distance alters resulting in the intermediate phase (typically Form III). When the twinning happens, the molecules in the twinning zone rotates a lot (about  $138^\circ$ ) and the two lattice vectors ( $[1\ 1\ 0]$  and  $[0\ 1\ 0]$ ) swap to form a mirror structure against the original Form I. The reversing process is associated with the recovery of molecular rotation and also the switching of those two lattice vectors. Figure 5.8(c) illustrates the magnified twinning interface characterized by a rotational change in molecular orientation. The upper Form-I (green) and lower twinned Form-I (blue) are packed in a mirror pattern, bridged by the interface layer (red) at the interfacial (010) plane. The interface configuration brings us a new perception of the molecular twinning. *In the molecule crystal, the twinning is not merely about the symmetric arrangements of each atomic site. Their internal molecular orientation also participates in the twinning transition.* Figure 5.8(d) demonstrates the optical image of the FE-I transition observed in experiments. The lattice correspondence of the mother and daughter phase agrees well with the experimental measurements. What's more, the angle-dependent polarized Raman intensity ratio also confirmed the molecular orientation rotation of  $138^\circ$ , which validates our hypothesis on the rotational motion-governed twinning mechanism. The color coding is determined by our defined order parameter ranging from 0 to 1 (as described in the *Simulation Method*). The green regimes represent the original Form I, red regions stand for the intermediate Form III and blue regions stand for the twinned Form I.

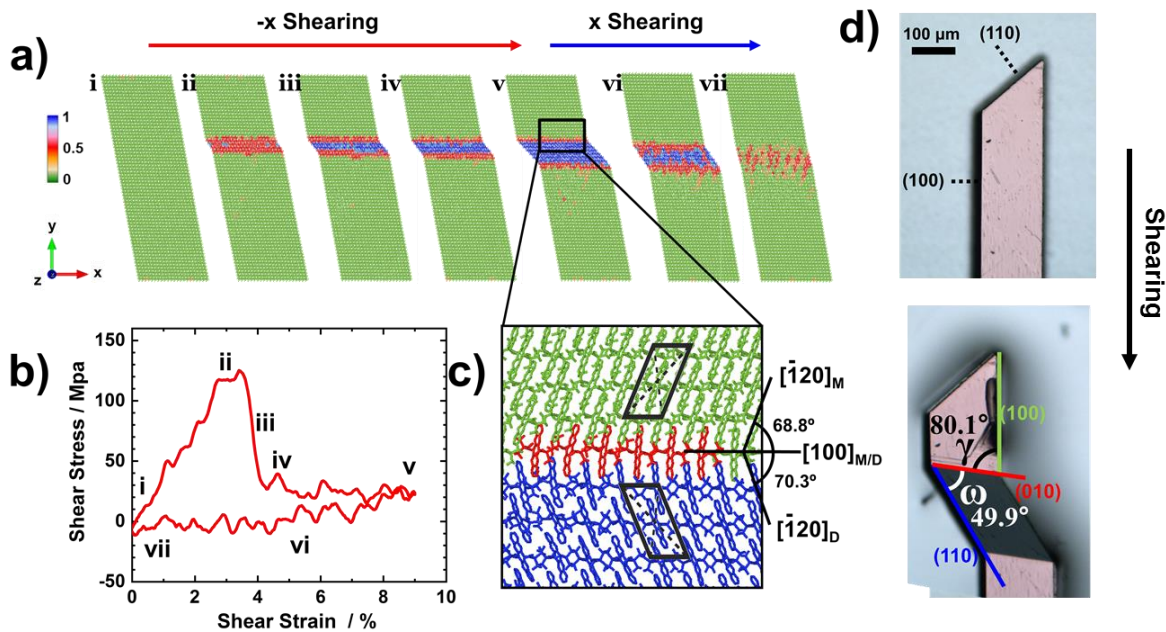


Figure 5.8. (a) six representative simulation snapshots of FE-I. The corresponding stress-strain curve is plotted in (b). (c) depicts the twinning interface. (d) Experimental observation of FE-I before and after the transition.

We are surprised to learn there is not only one type of ferroelasticity in the Tips-pentacene system. By applying the  $[0\ 1\ 0]$  stretching, the twinning Form I with the interface plane of  $(2\ 1\ 0)$  appears, which is regarded as the shape memory elasticity type II (FE-II). Similar analyses are conducted for the FE-II phenomena. Figure 5.9(a) shows six representative structural configurations during molecular dynamics simulation of FE-II transition by  $[0\ 1\ 0]$  stretching (y-axis) at 300K, and their corresponding stress-strain loop (Figure 5.9(b)). From configuration **i** to **ii**, Form-I structure undergoes the elastic deformation, while the intermediate phase gradually appears along the inclined direction which may cause the non-linear behavior around 3~7% strain in the stress-strain curve. After the onset (**ii**), the twinned phase appears and grows (up to configuration **v**) along  $(2\ 1\ 0)$  plane resulting in a significant stress release indicated by a large drop in the stress-strain curve. The twinning transition in FE-II also consists of two stages: the fast-growing stage I and the steady growing stage II. The associated stress-strain behavior is almost the same as what we found in the twinning transition in FE-I, which involves the linear stress reduction and the following steady plateau. After applying the compression strain along the y-direction, the twinning zone starts to recover back as shown in the configuration **v-vii**. The

martensitic transition of FE-II is also related to the stress-releasing mechanisms because of the obvious stress hysteresis.

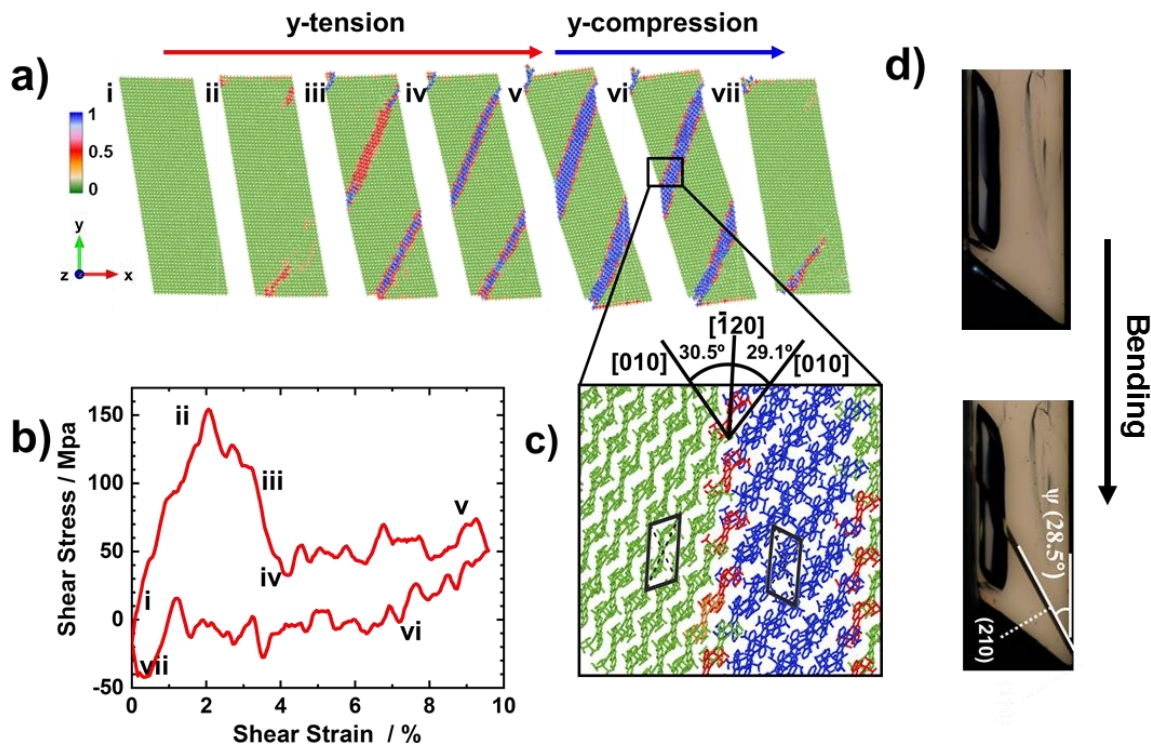


Figure 5.9. (a) six representative simulation snapshots of FE-II. The corresponding stress-strain curve is plotted in (b). (c) depicts the twinning interface. (d) Experimental observation of FE-II before and after the transition.

Distinct from the FE-I transition, the molecular orientation doesn't alter during the FE-II transformation. That is, *this twinning structure is formed merely by the displacive motion of molecules without any rotational motion*. Specifically, in the loading cycle, the inter-molecule distances along y-direction are firstly enlarged and the neighbor distances along x-direction shrink to accommodate the elastic deformation by stretching (as shown in configuration ii). Some molecules start to glide along the backbone direction ( $(2\ 1\ 0)$  plane) caused by the shear stress component of applied tensile  $\sigma_y$ . After the onset configuration ii, the shear stress component is large enough so that it exceeds the critical shear stress required to achieve the gliding motion of molecules along the  $(2\ 1\ 0)$  plane which can be regarded as the most favorable slip plane in this molecule system. The tensile stress is dramatically reduced by the formation of those “shear band”. It's interesting to find that the molecules within the “shear band” form the stable twinned structure with a mirror symmetry against the original Form I at the  $(2\ 1\ 0)$

interfacial plane. Also, the expansion of the twinning zone involves the step(kink) motion toward  $[0\ 1\ 0]$  direction which is different from the previous study on the motion of the twinning interface for traditional atomic compounds. The related analyses are omitted from this proposal. Figure 5.9(c) illustrates the magnified twinning interface characterized by displacive motion along with the  $[1\ \bar{2}\ 0]$  direction. The left Form-I (green) and right twinned Form-I (blue) are packed in a mirror pattern, bridged by the interface layer (red) at the interfacial  $(210)$  plane. Such lattice correspondence obtained from simulation matches well with the experimental observation depicted in Figure 5.9(d).

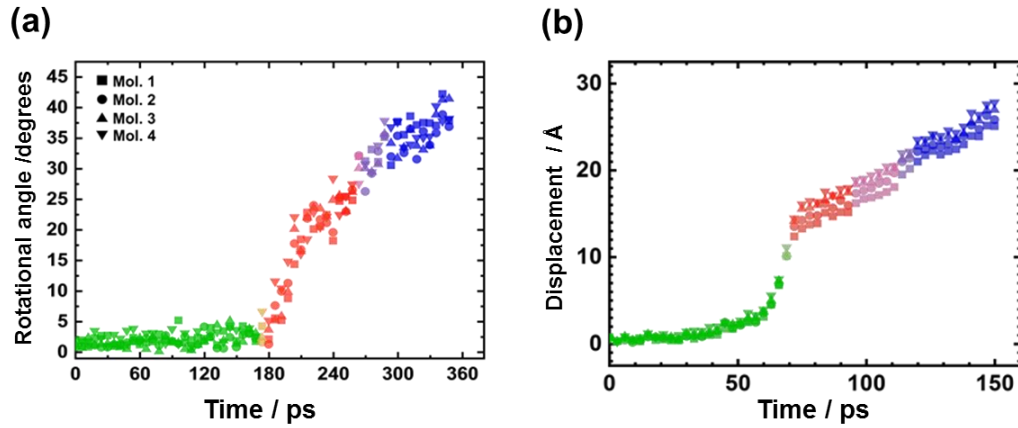


Figure 5.10. (a) The evolution of rotational angles of four molecules in a  $(0\ 1\ 0)$  layer in FE-I. (b) the evolution of displacement of four molecules in a  $(2\ 1\ 0)$  layer in FE-II.

We also elucidate molecular cooperativity during ferroelastic transitions by quantitatively evaluate the instantaneous changes in the molecular rotational and positional states. Based on the “point molecule scheme” (Figure 4.1), the rotational angle of one molecule  $\varphi_t$  at time  $t$  is calculated as below,

$$\varphi_t = \cos^{-1}(\vec{y}_o \cdot \vec{y}_t') \quad (5.4)$$

Here,  $\vec{y}_o$  is the unit vectors of the molecular  $y$ -axis (backbone direction) at the original state.  $\vec{y}_t'$  is the unit vector of molecular  $y$ -axis at time  $t$  projected onto the plane determined by  $\vec{y}_o$  and  $\vec{r}_o\vec{r}_t'$  (vector connecting the center of mass of molecules at two states). Figure 5.10(a) shows the temporal evolution of rotational angles for four neighbor molecules in one  $(010)$  layer, in accordance with the lattice transition from Form I (green) to intermediate (red) and eventually twinned Form I (blue) in FE-I. Such concerted intralayer molecular rotation further promotes

interlayer cooperativity (Figure 5.11). It is revealed in Figure 5.11 that the first layer starts the Form III–twinned I conversion as the second layer accomplishes the Form I–III transition. Such an interlayer domino effect signifies the molecular origin for the layer-by-layer process of the FE-I transition. Figure 5.10(b) demonstrates the concurrent displacive motions of four molecules in one (210) layer in FE-II. The displacement is calculated as the traveling distance of the center of mass of one molecule at time  $t$ .

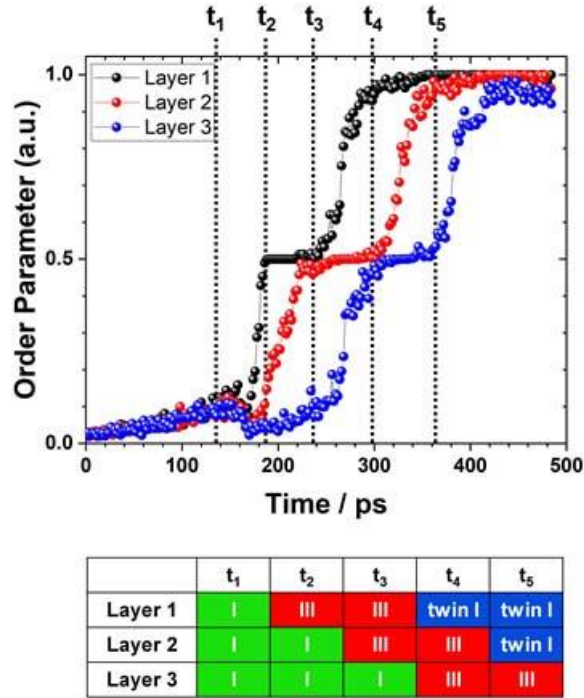


Figure 5.11. Time-dependent order parameter evolution of three adjacent molecular layers, upon FE-I transformation. Characteristic times  $t_1 - t_5$  are indicated by the dotted line. The plot clarifies layer-by-layer molecular cooperativity by showing a well-established transformation sequence, as summarized in the table below.

### 5.3.2 Interconvertible Behavior of Superelasticity and Ferroelasticity

Superelasticity is generally achieved by a reversible martensitic transition. The austenitic (mother) phase spontaneously reforms when the external load is released. As a comparison, ferroelasticity is often accomplished by deformation twinning and the structure recovers its original shape when loaded in an opposite direction. Figure 5.12 shows the snapshots of the molecular structure in the ferroelasticity and superelasticity of TIPS-pentacene at 400K. The molecules of different phases are color-coded by the order parameter. It demonstrates that SE and FE are interconvertible in Form II under  $\langle 1\ 0\ 0 \rangle$  shear. The interconvertibility represents

that the shear deformation along  $[\bar{1} 0 0]$  transforms Form II to a twinned phase, while the opposite load along  $[1 0 0]$  recovers Form II to the original shape, and a further increase of the shear strain leads to the superelasticity and a self-recoverable transition of Form II-to-I. Figure 5.12B plots the corresponding stress-strain responses. A large hysteresis loop in the ferroelastic process, while superelasticity proceeds with a much smaller stress hysteresis.

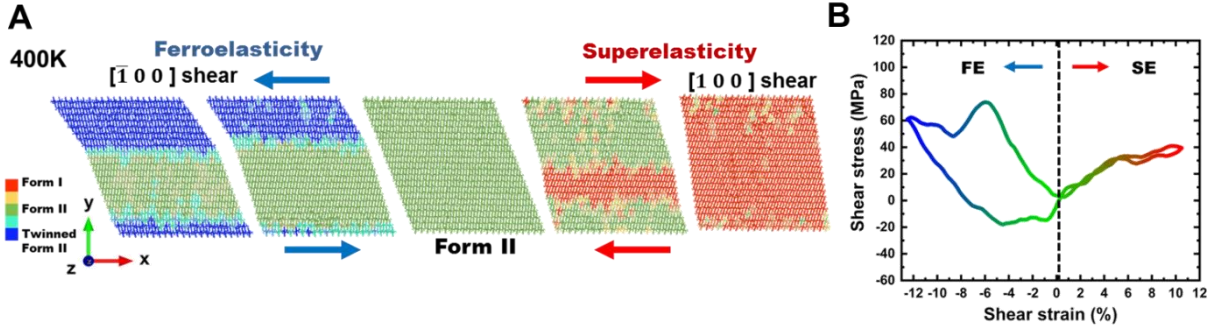


Figure 5.12. (A) The molecular trajectories of the interconvertible SE and FE of Form II by  $\langle 1 0 0 \rangle$  shear at 400 K. Their corresponding stress-strain responses are shown in (B). The molecules in (A) are color-coded by the order parameter representing the different phases as marked in the color bars.

Figure 5.13A illustrates the lattice transformation of ferroelasticity and superelasticity in Form II. The cells of different colors represent different polymorphs of distinct molecular orientations. Although SE and FE involve distinct lattice changes and molecular motions, they share the same  $(0 1 0)$  habit plane, which provides the crystallographic basis for the interconvertible behavior. Lattice transformation in SE and FE can be described by the deformation gradient matrix and the Euler rotational angles. For FE, the lattice deformation

matrix is  $F = \begin{bmatrix} 1.03 & -0.28 & 0 \\ 0.06 & 1.06 & 0 \\ -0.01 & 0 & 1 \end{bmatrix}$ , which shows a simple shear deformation with a shear

component of -0.28 in the  $ab$  plane. The Euler angles  $[\theta, \varphi, \omega]$  are  $[11^\circ, -3^\circ, 0.57^\circ]$ , where the major orientational change is the counterclockwise rotation in  $\theta$  about the  $\vec{w}$  axis. In SE, where Form II-to-I phase transition occurs, the Bain strain matrix<sup>30</sup> is calculated as

$B = \begin{bmatrix} 0.99 & 0.20 & 0 \\ -0.03 & 0.89 & 0 \\ 0.02 & 0 & 1 \end{bmatrix}$ , which shows a simple shear component of 0.20 and a compression of

0.11 along the  $b$  axis upon the transition. The associated Euler angles are  $[-9.8^\circ, 8.9^\circ, 1.8^\circ]$ . The clockwise rotation of  $9.8^\circ$  in  $\theta$  denotes the shear deformation. Meanwhile, a notable change of

$8.9^\circ$  in  $\varphi$  occurs as molecules rotate counterclockwise about the  $\vec{v}$  axis, which is related to the shrinkage in the  $b$  lattice. It's worth noting that the characteristic shear strain in the Bain matrix and the  $\theta$  angle in the Form II-to I superelastic transition are opposite to those of Form I-to-II thermoelastic transition, showing the equivalence of thermal and mechanical load on modulating the polymorphic transitions<sup>31</sup>.

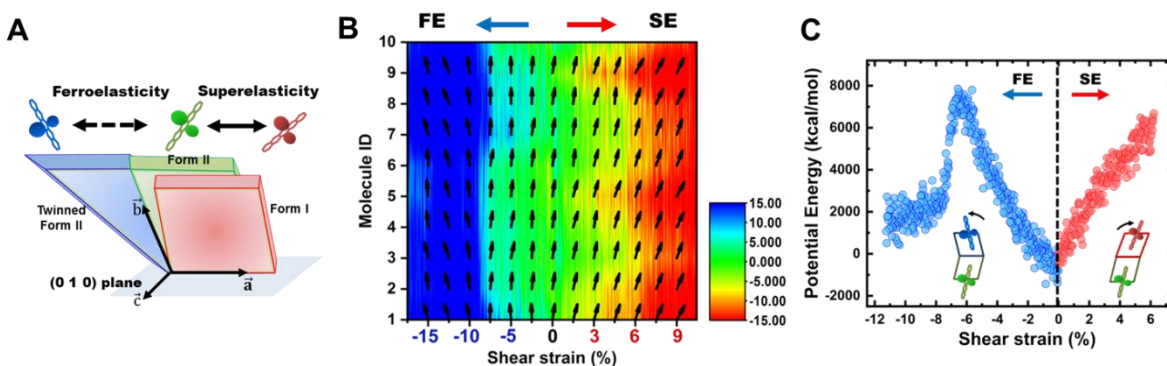


Figure 5.13. (A) Sketch of the lattice transformation of ferroelasticity and superelasticity in Form II. The cells of different colors represent different polymorphs of distinct molecular orientations. (B) Contour plot of the molecular rotation of 10 molecules in Form II under  $\langle 1\ 0\ 0 \rangle$  shear load. The black arrows are the vectors representing the direction of the molecular orientation. (C) The molecular potential energy as a function of the shear strain when Form II is deformed by shear. The insets show the deformation twinning associated with FE (left) and lattice transition from Form II to Form I associated with SE (right).

The concerted molecular rotation is a striking characteristic of SE and FE in the organic crystal. Figure 5.13B shows a contour map of the molecular rotation for 10 molecules in a row under  $\langle 1\ 0\ 0 \rangle$  shear deformation. The color scheme represents the change in angle  $\theta$  with respect to its original value. The black arrow denotes the positive  $\vec{v}$  vector of each molecule, which aligns with the direction of molecular backbone. All molecules in the supercell of Form II are subjected to a shear strain with the magnitude varying from -17.5% to +11.5%. During the shear deformation, the molecular orientation is collectively adapted to the shear direction. Such rotational adapting behavior is perhaps analogous to the process that a magnetic/electric dipole ( $\vec{p}$ ) seeks to align with the applied magnetic/electric field ( $\vec{B}$ ) in favor of the energy reduction  $= -\vec{p} \cdot \vec{B}$ <sup>32</sup>. Intuitively, we may regard each molecule as an independent and rigid “compass needle” exposed to the stress field. Compared to the  $[1\ 0\ 0]$  shear induced superelastic transition, ferroelastic twinning is expected to carry a larger energy reduction of the system because the molecules need to rotate by a bigger angle to align with the  $[\bar{1}\ 0\ 0]$  shear (see the sketch in Figure 5.13A). In FE, a sharp transition front of the molecular orientation is observed at -7.5%

shear strain, where the molecules flip the orientation concurrently so that the projection of the molecular orientation becomes parallel to the shear direction. Such concerted rotational motion is absent when the molecules are subject to  $[1\ 0\ 0]$  shear in SE, where a diffusive transition front at  $\sim 5\%$  strain is observed in the contour map. The asynchronous molecular orientations in the  $(0\ 1\ 0)$  layer are also evident in both the experiments and molecular trajectories of SE (Figure 5.12A). The structural responses of SE and FE are related to their difference in the potential energy profile (Figure 5.13C). The potential energy of ferroelastic deformation increases linearly in the early elastic response to the shear deformation, and then quickly drops after the barrier of the concerted drastic rotation of molecules is passed. In comparison, the potential energy of SE continuously increases with a slight drop when the transition occurs at  $\sim 4.5\%$  shear strain, when the molecules orientate along the shear direction. Overall, the superelastic transition is absent of the dissipation mechanism of the free energy, and the stored mechanical energy facilitates shape recovery upon removal of the shear load. Deformation twinning is the carrier of the substantial energy loss in FE. The molecules restore the initial shape through de-twinning under a reverse load. The inset in Figure 5.13C sketches the lattice change in FE and SE, with the upper cell showing the transformed phase and the lower one the original Form II. From the lattice transformation matrix, we learn that the simple shear deformation in FE renders the original and transformed lattices packed with a mirror symmetry, which minimizes the interfacial energy and stabilizes the phase boundary. In contrast, the compression in the  $b$ -lattice shown in the Bain strain matrix for SE dictates a considerable strain energy at the Form II-I interface, which in turn, contributes to the spontaneous shape recovery upon unloading. The interconvertible SE and FE demonstrates the rich polymorphic changes in TIPS-pentacene adaptive to the external load. Mechanical deformation can be potentially utilized during and/or post solution processing to manipulate the molecular structure and used as an effective way to investigate their structure-property relationships in various polymorphs<sup>19,33</sup>.

### 5.3.3 Molecular Twinning and Molecular Defects

We make a closer examination on the nucleation and crystallographic principle of molecular twinning in the ferroelasticity of TIPS-pentacene. We described two types of ferroelasticity mediated by deformation twinning in Figure 5.13 – FE-I by  $[\bar{1}\ 0\ 0]$  shear and FE-II by  $[0\ 1\ 0]$  tension at 300K. In the two ferroelastic transitions, Form I first transforms to an intermediate

metastable phase and then forms the twinned phase. We determine the molecular kinetics of the two forms of ferroelasticity separately. Phenomenological theories<sup>13,34</sup> are also used here to describe the crystallography of twinning in molecular crystals.

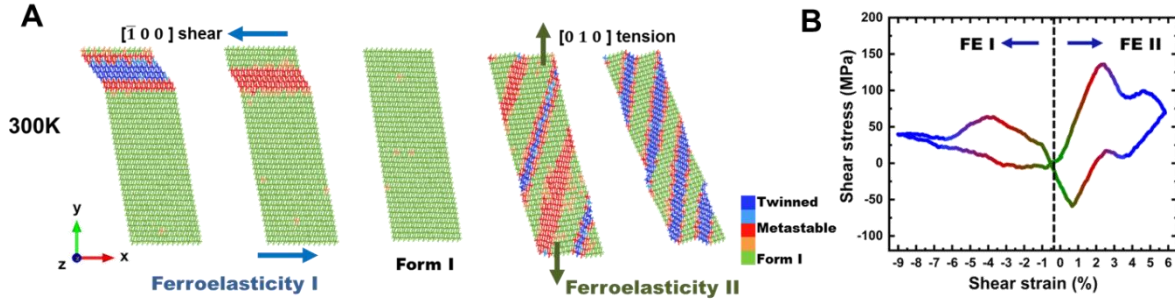


Figure 5.14. (A) The molecular trajectories of FE-I and FE-II of Form I by  $[\bar{1} 0 0]$  shear and  $[0 1 0]$  tension at 300K, respectively. Their corresponding stress-strain responses are shown in (B). The molecules in (A) are color-coded by the order parameter representing the different phases as marked in the color bars.

In FE-I, the base centered lattice shown in Figure 5.15A is used to present the molecular trajectories, where one molecule resides at each corner and two molecules occupy the center of the front and back planes, respectively. The crystallographic relationships between the parent and twinned lattices can be described by four independent twinning elements  $(K_1, K_2, \eta_1, \eta_2)^{36}$ . In FE-I,  $K_1$  is the undistorted and unrotated habit plane  $(0 1 0)$ .  $K_2$  is the conjugated twinning plane which is undistorted but rotated. This plane is marked as  $K_2^T$  in the twinned lattice.  $K_2/K_2^T$  is  $(2 \bar{1} 0)$  plane in FE-I. The molecules in the  $K_2$  plane point to the  $[\bar{1} \bar{2} 0]$  direction, which is defined as the  $\eta_2/\eta_2^T$  conjugated twinning direction.  $\eta_1$  denotes the shear direction  $[\bar{1} 0 0]$ . Along the  $\eta_1$  direction twinning proceeds with a shear amount of  $s = 2\tan(\alpha)$ , where the angle  $\alpha$  represents a half of the angle between  $\eta_2$  and  $\eta_2^T$ . Upon deformation twinning, the molecular backbone along the  $\eta_2$  direction ( $\vec{v}$  axis in Figure 4.8A) rotates in the counterclockwise direction. With the given initial molecular crystallography of Form I,  $\alpha$  can be theoretically determined as  $20^\circ$ . The twinning elements  $(K_1, K_2, \eta_1, \eta_2)$  fully describe the deformation gradient matrix in the following form<sup>14</sup>:

$$S = \begin{bmatrix} 1 + sm_1n_1 & sm_1n_2 & sm_1n_3 \\ sm_2n_1 & 1 + sm_2n_2 & sm_2n_3 \\ sm_3n_1 & sm_3n_2 & 1 + sm_3n_3 \end{bmatrix}$$

where  $\vec{m}$  represents the twinning direction and  $\vec{n}$  is the normal vector of the  $K_1$  plane. In FE-I, the shear amount is given by  $s = 2 \tan(20^\circ) = 0.73$ .  $\vec{m}$  and  $\vec{n}$  are  $[\bar{1} 0 0]$  and  $[0 1 0]$ ,

respectively. These values determine the deformation matrix as  $\begin{bmatrix} 1 & -0.73 & 0 \\ 0 & 1 & 0 \\ 0 & 0 & 1 \end{bmatrix}$ . In the simulation, the deformation matrix is calculated as  $\begin{bmatrix} 1.01 & -0.74 & 0 \\ -0.04 & 1.07 & 0 \\ -0.02 & -0.01 & 1 \end{bmatrix}$ , which agrees well with the theoretical prediction. The Euler angles  $[\theta, \varphi, \omega]$  are further determined as  $[42.7, -4.2, -4.0]$ , which shows the characteristic rotational change of  $42.7^\circ$  in  $\theta$  in the FE-I transformation.

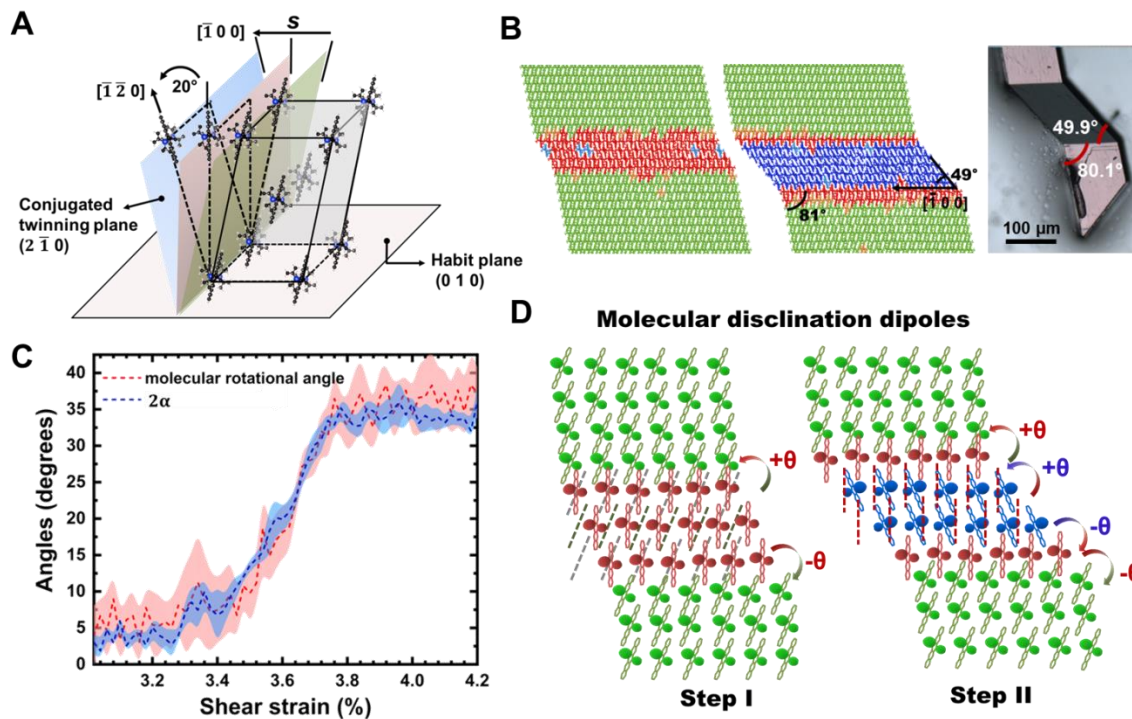


Figure 5.15. (A) Illustration of the twinning elements of FE-I in Form II. (B) Snapshots of the molecular structure showing the metastable phase (red) and the twinned phase (blue). The twinning angles in the modeling match well with the experimental observation (optical image). (C) Correlation between the molecular rotational angle (red) and the angle ( $2\alpha$ ) between the conjugated twinning planes (blue). The dotted curves denote the mean values for five different cells in the modeling and the shaded areas represent the standard deviations. (D) The two-step twinning formation achieved by molecular disclination dipoles.

The molecular structures of the intermediate metastable and twinned phases are shown in the snapshots of Figure 5.15B. Upon  $[\bar{1} 0 0]$  shear, the molecular backbones rotate counterclockwise by  $20^\circ$ , generating a metastable phase with the molecular packing close to Form III. A further counterclockwise rotation of  $20^\circ$  leads to the final phase with a mirror symmetry of the pristine polymorph. The twinning angles in the modeling match well with the experimental results as shown in the optical imaging. Figure 5.15C illustrates the correlation between the molecular

rotational angle and the angle between the conjugated twin planes  $2\alpha$ . The dotted lines denote the mean values for five different cells, each containing five molecules, at different locations of the entire simulation model in order to minimize the statistical variation. The shaded areas represent the standard deviations. The molecular structural features demonstrate that deformation twinning in ferroelastic transformation is dominated by the overall molecular rotation. The orientational motion at the twinning interface is close to the concept of a disclination, which is an extended structure originally proposed by Volterra<sup>37</sup>, and has been used to describe the linear rotational defect in the reorientation of molecules in liquid crystals<sup>38</sup>. Under external (thermal, mechanical, electrical) stimuli, a rapid change in the preferred orientation in the vicinity of a line/point is recognized as disclination<sup>39</sup>. Molecules in TIPS-pentacene in the (0 1 0) plane have sufficient flexibility to adapt their orientations to the external shear as shown in Figure 5.13B, which behave similarly with the loosely packed molecules in liquid crystal. By this analogy, we define the orientational perturbation in the twinning process of FE-I as molecular disclination dipole, as shown in Figure 5.15D. Here, individual layers show molecular rotations, rather than translations, thus are indicative of disclination rather than dislocation movement. In the intermediate phase, a counterclockwise rotation of  $+\theta$  ( $20^\circ$ ) in the upper transformed layer (red molecules) is required while a clockwise operation of  $-\theta$  can recover the initial state at the lower bound. Such paired rotational operations are defined as molecular disclination dipoles. The metastable phase proceeds by an additional pair of  $\pm \theta$  rotational operations and forms the twinned phase (blue molecules). Compared to the continuous variation in molecular orientation in liquid crystals, the disclination dipoles in TIPS-pentacene have well-determined, quantized rotational operations and therefore retain their molecular order. The shearing operation of twinning and martensitic transformation in metals<sup>13,14</sup> are considered to be carried out through coordinated dislocation movement, which translates each (or every other) layer of the crystal individually. The rotational operation of an individual molecular layer does not accumulate with dipoles as it would with individual disclinations, and is carried on sequentially by the successive layers, which eliminates potential molecular packing faults. Hence, the unique molecular disclination dipoles promise a strong structural integrity in FE-I. The molecular packing in both the experiments and simulations is well retained without structural disruption.

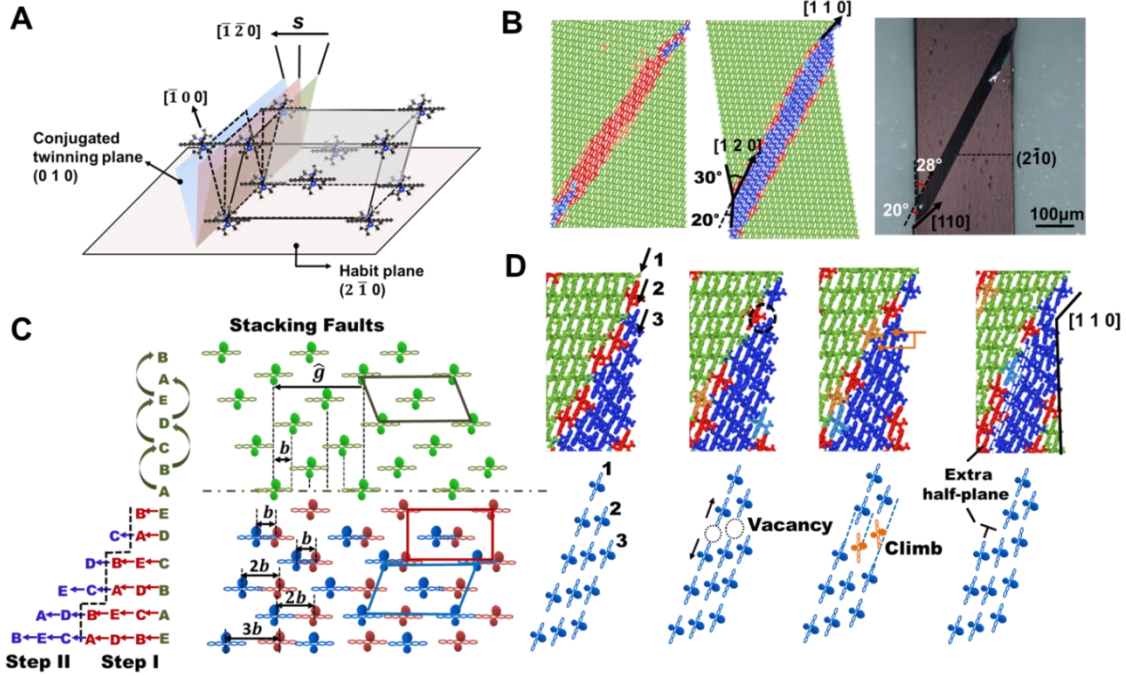


Figure 5.16. (A) The twinning elements of FE-II in Form II. (B) Snapshots of the molecular structure upon mechanical load showing the metastable phase (red) and the twinned phase (blue). The optical image shows the crystallography of twinning and a surface crack in experiments. (C) The two-step formation mechanism of twinning by the stacking faults. (D) Snapshots (upper panel) demonstrate the ejection of a molecular dislocation accompanying the twinning process. Lower panel shows the magnified view of vacancy formation and dislocation climb in the  $(2 \bar{1} 0)$  layers.

Following the same procedure, we analyze the crystallographic principle of twinning in FE-II. As sketched in Figure 5.16A, the base centered lattice cell is subject to a  $[\bar{1} \bar{2} 0]$  shear with a habit plane of  $(2 \bar{1} 0)$ . The conjugated twinning plane and conjugated twinning direction are  $(0 1 0)$  and  $[\bar{1} 0 0]$ , respectively. It is interesting to note that the twinning elements of FE-II are essentially the reciprocal of that of FE-I:  $K_1^{\text{FE-II}} = K_2^{\text{FE-I}}$ ,  $K_2^{\text{FE-II}} = K_1^{\text{FE-I}}$ ,  $\eta_1^{\text{FE-II}} = \eta_2^{\text{FE-I}}$ ,  $\eta_2^{\text{FE-II}} = \eta_1^{\text{FE-I}}$ <sup>13</sup>. The twinning in FE-II is mainly driven by the  $[\bar{1} \bar{2} 0]$  shear component of the applied tension in  $[0 1 0]$ , while other stress components cause tilt of the lattice. In the phenomenological theory, deformation twinning in FE-II is described by keeping its interface plane unrotated during the transition. The twinning elements to construct the deformation gradient matrix are  $s = 2 \tan(20^\circ) = 0.73$ ,  $\vec{m} = [\bar{1} \bar{2} 0]$ , and  $\vec{n} = [2 \bar{1} 0]$ , which yields the

deformation gradient matrix  $\begin{bmatrix} 0.64 & 0.18 & 0 \\ -0.73 & 1.36 & 0 \\ 0 & 0 & 1 \end{bmatrix}$ . The theoretical prediction is again close to the

lattice deformation matrix in the simulation  $\begin{bmatrix} 0.69 & 0.18 & -0.01 \\ -0.64 & 1.21 & 0.08 \\ -0.04 & 0.02 & 1.01 \end{bmatrix}$ . Given that the molecular

backbones are co-aligned on the  $(2\bar{1}0)$  habit plane (Figure 5.16A) and the shear direction  $[\bar{1}\bar{2}0]$  aligns with the backbone orientation, the deformation twinning in FE-II is accommodated by the displacive motion of the molecules rather than the rotational disclination as described in FE-I. The twinning kinetics also consists of two steps, where a metastable phase first emerges along the habit plane before the formation of the twinned phase (Figure 5.16B). The twinned molecular structure in the simulation agrees well with the optical observation in the experiments. We also note that surface cracks along the  $[110]$  direction in the twinning configuration are often observed in the FE-II experiments, which largely compromise the electronic performance of the stretchable semiconductor device over cycles. The formation mechanism of twinning and cracking is understood by the stacking faulting and molecular dislocations. Figure 5.16C demonstrates the stacking sequence of  $ABCDE$  along the  $[2\bar{1}0]$  direction of TIPS-pentacene. Due to the two-dimensional brickwork packing molecular structure, the  $ABCDE$  stacking follows an alternative transformation sequence, that is,  $A \rightarrow C \rightarrow E \rightarrow B \rightarrow D \rightarrow A$ , upon the displacive motion. A stacking fault can be formed by the molecular partial dislocation  $\vec{b} = \frac{1}{5}\hat{g}$ , where  $\hat{g}$  denotes the vector connecting the two adjacent molecules on the  $(2\bar{1}0)$  habit plane (Figure 5.16C). Figure 5.16C illustrates the details of the two-step mechanism of the twinned Form I based on the stacking faults. First, a metastable phase is produced by the motion of the partial dislocations on “odd number” alternate layers, where the original stacking sequence of  $EDCBAE$  is transformed locally into the sequence  $BABABA$ . Then, the twin embryo is generated by a further motion of partial dislocations on the “even number” alternate layers, resulting in the final stacking sequence of  $BCDEAB$ . Such a two-step formation process of molecular twinning in TIPS-pentacene is analogous to the FCC/HCP twinning mechanism where, in the FCC lattice, Shockley partial dislocations transform the stacking of  $ABCABC$  in FCC to an intermediate stacking of  $ABABAB$  (HCP) and eventually to the stacking of  $ACBACB$  as twinned FCC<sup>39</sup>. The stacking faulting correlates with the phenomenological theory (Figure 5.16A). The half of the twinning shear amount is essentially the ratio of the length of the burgers vector  $\vec{b}$  to the spacing of the  $\{2\bar{1}0\}$  plane. This sequential stacking transition guarantees the undistorted conjugated twinning plane  $K_2^T$  in the twinned phase. In the twinning transition, the glide motion of  $(2\bar{1}0)$

molecules may result in the ejection of a full dislocation. The upper panel in Figure 5.16D depicts four representative molecular trajectories in this process. For ease of view, we show the details of three  $(2\bar{1}0)$  molecular layers of interest in the lower panel. The three layers are initially packed as twinned Form I (first snapshot). Two vacancies are generated by the asynchronous gliding of the neighboring molecules within one molecular layer (second snapshot), possibly due to the inhomogeneity of the strain field near the surface or thermal fluctuation. Then, two adjacent molecules (orange in the third snapshot) tilt their backbone orientation toward the center of the vacancies in response to the attractive forces from the dangling intermolecular “bonds” around the vacancies. The newly formed intermolecular bonds migrate the molecules originally in layers 1 and 2 to the layers 2 and 3, respectively, which results in the climb of the vacancies across the  $(2\bar{1}0)$  habit plane (fourth snapshot). After equilibrium, an extra half-plane is formed in the model with the appearance of a step crack along the  $[110]$  direction that verifies the experimental observation. Both the formation and climb of vacancies involve the cooperative motion of a molecule pair, which may arise from the pair attraction between two adjacent backbones as well as the steric hindrance effect of the side groups of two nearest molecules. To prevent crack formation due to the asynchronous molecular glide, a slight increase in temperature may eliminate the precursor of the vacancies or a design of less bulky side groups may help reduce the glide resistance from the neighboring molecules.

### 5.3.4 Electronic Properties

Understanding the electronic structure and charge transport of Tips-pentacene polymorphs is vital to improve the electronic performance of the thin-film semiconductor device. We first examine the molecular orbitals and obtain the band gap information from quantum chemistry calculation. Then, the charge transport in the ferroelastic transition is tentatively investigated based on Marcus theory.

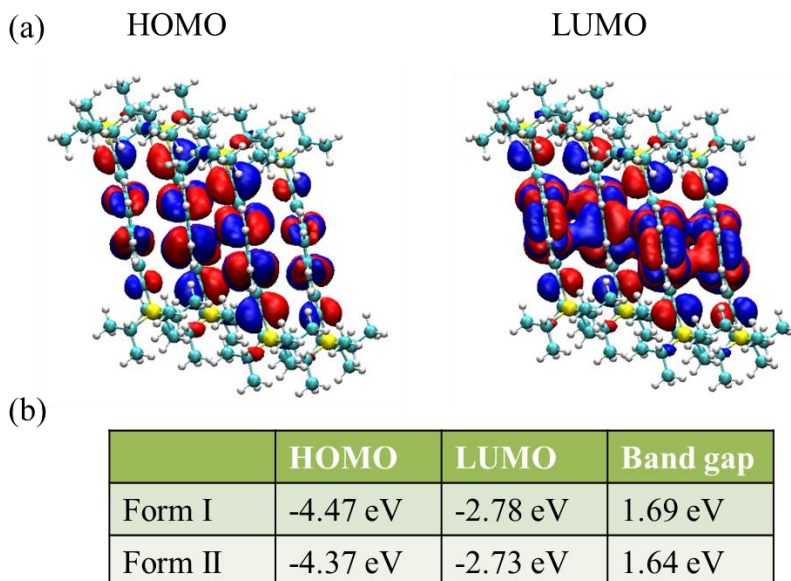


Figure 5.17. (a) HOMO and LUMO orbitals of Form I. (b) The values of HOMO, LUMO, and band gap for Form I and Form II.

Band gap is an important measure of charge transfer of semiconductor molecules. Figure 5.17 shows the HOMO and LUMO orbitals of Form I as well as the band gap of Form I and Form II. We learn that the  $\pi$ -bonding states in the HOMO level of Form I is more stabilized than that of Form II, which results in a higher absolute value of the HOMO energy of Form I, while the  $\pi^*$  anti-bonding states in the LUMO level of the two forms are similar. The 0.1 eV difference in HOMO results in a higher bandgap in Form I, which indicates that Form II has a better charge transfer capability and a longer absorption wave length than Form I. The charge transport rate can be determined by the Marcus theory<sup>40</sup>:

$$k = \frac{|V_{ij}|^2}{\hbar} \frac{\sqrt{\pi}}{\sqrt{\lambda k_B T}} \exp\left(-\frac{(\lambda + \Delta G^0)^2}{4\lambda k_B T}\right) \quad (5.5)$$

where  $k$  is the charge transfer rate,  $|V_{ij}|$  is the electronic coupling between the initial and final states (i.e. charge transfer integral),  $\lambda$  is the reorganization energy (electron or hole),  $\Delta G^0$  is the Gibbs free energy change for the electron transfer,  $k_B$  is the Boltzmann constant, and  $T$  is temperature. The charge transfer in organic molecules is described by the electron or hole hopping among inter-molecules,  $M^{+/-} + M^* \rightarrow M + M^{*+/-}$ , where the reactant  $M^{+/-}$  represents the

molecule in the cationic or anionic state,  $M^*$  is a neighboring molecule in a neutral state, the products  $M$  and  $M^{*+/-}$  indicate the neutral molecule and its charged neighbor molecule, respectively. The reorganization energy for the hole and electron transport is calculated based on the potential energy of neutral and charged states,  $\lambda^{+/-} = E_n(M^{+/-}) - E_n(M^*) + E_c(M^*) - E_c(M^{+/-})$ , where  $E_n(M^{+/-})$  is the energy of a neutral molecule in the charged geometry,  $E_n(M^*)$  is the ground-state energy of a neutral molecule in its optimized neutral geometry.  $E_c(M^*)$  and  $E_c(M^{+/-})$  represent the energy of a charged molecule in the neutral geometry and charged geometry, respectively. For a given molecular system, the chemical driving force (i.e. Gibbs free energy) and reorganization energy can be roughly estimated as constant values. Hence, the charge transfer integral plays an important role in determining the charge transport rate. According to the frozen-core approximation, for an organic semiconductor, the electron transport is supposed to occur in the LUMO while the HOMO orbital is the carrier of hole transport. The magnitude of the electronic coupling is given by,

$$V_{ij} = \langle \varphi_i | \hat{H} | \varphi_j \rangle \quad (5.6)$$

Here,  $\varphi_i$  and  $\varphi_j$  represents the HOMO and LUMO wave functions at sites  $i$  and  $j$ , respectively.  $|\hat{H}|$  dictates the single electron Hamiltonian operator. We calculate the charge transfer integral for 10 molecules across the twinning interface in the FE-II transition as depicted in Figure 5.18. In the contourmap, the value of charge transfer integral increases as the color changes from blue to red. The blue zone represents the twinning region and the white zone marked by the dotted lines stands for the twinning interface. The rest dictates the original Form I region. It infers that the molecular packing in the twinning zone possesses a lower charge transfer rate than the untwinned region. Thus, a slight drop in the electronic conductivity is anticipated once ferroelastic transition happens, which agrees well with the experimental observation. Besides, several spots in the interface zone present a relatively high charge transfer integral, which perhaps indicates a heterogeneous charge transfer in the interface domain wall. Such an intriguing phenomenon is worth further investigation in the future.

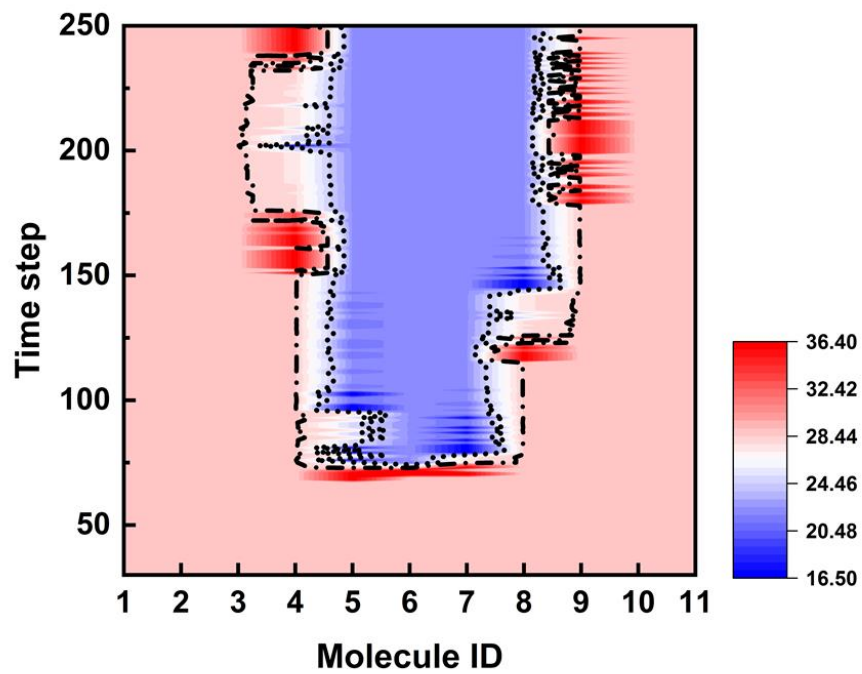


Figure 5.18. The charge integral map for ten molecules across the twinning zone in FE-II transition.

## 5.4 References

1. Ghosh, S.S.; Reddy C.M., *Angew. Chem., Int. Ed.*, **2012**, *51*, 10319– 10323.
2. Worthy, A.; Grosjean, A.; Pfrunder, M.C.; Xu, Y.; Yan, C.; Edwards, G.; Clegg, J.K.; McMurtrie, J.C., *Nat. Chem.*, **2018**, *10*, 65– 69.
3. Panda, M.K.; Ghosh, S.; Yasuda, N.; Moriwaki, T.; Mukherjee, G.D.; Reddy, C.M.; Naumov, P., *Nat. Chem.*, **2015**, *7*, 65-72.
4. Ahmed,E.; Karothu, D.P.; Warren, M.; Naumov, P., *Nat. Commun.*, **2019**, *10*, 1-9.
5. Liu, H.; Lu, Z.; Tang, B.; Qu, C.; Zhang, Z.; Zhang, H., *Angew. Chem. Int. Ed.*, **2020**, *59*, 12944.
6. Ahmed, E.; Karothu, D.P.; Naumov, P., *Angew. Chem. Int. Ed.*, **2018**, *57*, 8837-8846.
7. Zeng, H.; Wasylczyk, P.; Parmeggiani, C.; Martella, D.; Burrelli, M.; Wiersma, D.S., *Adv. Mater.*, **2015**, *27*, 3883-3887.
8. Kim, T.; Zhu, L.;Al-Kaysi, R.O.; Bardeen, C.J., *ChemPhysChem*, **2014**, *15*, 400-414.
9. Koshima, H.; Matsuo, R.; Matsudomi, M.; Uemura, Y.; Shiro, M., *Cryst. Growth Des.*, **2013**, *13*, 4330-4337.
10. Takamizawa, S.; Miyamoto, Y., *Angew. Chem.*, **2014**, *126*, 7090-7093.
11. Engel, E. R.; Takasaki, Y.; Mir, S. H.; Takamizawa, S., *R. Soc. open sci.*, **2018**, *5*, 171146.
12. Tadaki, T.; Otsuka, K.; Shimizu, K., *Annu. Rev. Mater. Sci.*, **1988**, *18*, 25-45.
13. Christian, J.W., *The theory of transformations in metals and alloys: Part I*, Pergamon Press, Oxford, **1975**.
14. Bilby, B.A.; Crocker, A., *P. Roy. Soc. A-Math. Phy.*, **1965**, *288*, 240-255.
15. Van den Ende, J.A.; Ensing, B.; Cuppen, H.M.,*CrystEngComm*, **2016**, *18*, 4420-4430.
16. Sasaki, T.; Sakamoto, S.; Takasaki, Y.; Takamizawa, S., *Angew. Chem., Int. Ed.*, **2020**, *59*, 4340-4343.
17. Sasaki, T.; Sakamoto, S.; Takamizawa, S.,*Cryst. Growth Des.*, **2019**, *19*, 5491-5493.
18. Mei, J.; Diao, Y.; Appleton, A.L.; Fang, L.; Bao, Z., *J. Am. Chem. Soc.*, **2013**, *135*, 6724-6746.
19. Diao, Y.; Tee, B.C.; Giri, G.; Xu, J.; Kim, D. H.; Becerril, H.A.; Stoltenberg, R.M.; Lee, T.H.; Xue, G.; Mannsfeld, S.C., *Nat. Mater.*, **2013**, *12*, 665-671.
20. Chung, H., Dudenko, D., Zhang, F., D'Avino, G., Ruzié, C., Richard, A., Schweicher, G., Cornil, J., Beljonne, D., Geerts, Y., *Nat. Commun.*, **2018**, *9*, 278.
21. Park, S. K.; Sun, H.; Chung, H.; Patel, B. B.; Zhang, F.; Davies, D. W.; Woods, T. J.; Zhao, K.; Diao, Y., *Angew. Chem. Int. Ed.*, **2020**, *59*, 13004.

22. Hutter, J.; Iannuzzi, M.; Schiffmann, F.; VandeVondele, J., *Comput. Molecular Science*, **2014**,*4*, 15-25.
23. VandeVondele, J. ; Hutter, J., *J. Chem. Phys.*, **2007**, *127*, 114105 .
24. VandeVondele, J.; Krack, M.; Mohamed, F.; Parrinello, M.; Chassaing, T.; Hutter, J., *Comput. Phys. Commun.*, **2005**, *167*, 103-128 .
25. Krack, M., *Theor. Chem. Acc.*, **2005**,*114*, 145-152.
26. Grimme, J. Antony, S. Ehrlich, H. Krieg, *J. Chem. Phys.*, **2010**, *132*, 154104.
27. Plimpton, S.; Crozier, P.; Thompson, A., *Sandia National Laboratories*, **2007**, *18*, 43-43.
28. Jorgensen, W.L., Maxwell, D.S., Tirado-Rives, J., *J. Am. Chem. Soc.*, **1996**, *118*, 11225-11236.
29. Meyers, M. A.; Chawla, K. K., *Mechanical behavior of materials*, Prentice Hall, New Jersey, **1999**, pp. 66-75.
30. Christian, J. W., *The theory of transformations in metals and alloys: Part I*, Pergamon Press, Oxford, **1975**.
31. Wollants, P.; De Bonte, M.; Roos, J., *Z. Metallkd.* **1979**, *70*, 113-117.
32. D. Halliday, R. Resnick, K. S. Krane, *Physics*, Jon Wiley & Sons, Inc., Hoboken, NJ USA, **2010**, pp. 600-602
33. Giri, G.; Verploegen, E.; Mannsfeld, S.C.; Atahan-Evrenk, S.; Kim, D.H.; Lee, S.Y.; Becerril, H.A.; Aspuru-Guzik, A.; Toney, M.F.; Bao, Z., *Nature*, **2011**, *480*, 504-508.
34. Niewczas, M., *Dislocations in solids*, (Eds.: F. R. N. Nabarro, J. P. Hirth), Elsevier B.V., Amsterdam, **2007**, pp. 263-364.
35. Volterra, Vito. *Ann. Sci. de l'École Norm. Supérieure*, **1907**, *24*, 401-517.
36. Hall, E., *Twinning and diffusionless transformations in metals*, Butterworths, London, **1954**.
37. Fan, C., *Phys. Lett. A*, **1971**, *34*, 335-336.
38. Chandrasekhar, S.; Ranganath, G., *Adv. Phys.*, **1986**, *35*, 507-596.
39. Olson, G. B.; Cohen, M., *Metall. Trans.*, **1976**, *A 7*, 1897-1904.
40. Marcus, R.A., *Angew. Chem., Int. Ed.*, **1993**, *32*, 1111-1121.
41. Idzik, K.; Cywiński, P.; Kuznik, W.; Glaser, L., Techert, S., *J. Chem. Eng. Process Technol.*, **2017**, *8*, 355.
42. Iwan, A., Mazurak, Z., Sek, D., *Polym. Eng. Sci.*, **2007**, *47*, 1179-1186.

## CHAPTER 6. SUMMARY AND BROAD IMPLICATION

### 6.1 Summary of the Thesis

In this thesis, we employ a spectrum of modeling methods, including quantum chemistry, ab-initio modeling, and molecular dynamics simulation, to systematically investigate the phase dynamics and physico-mechanical behaviors of battery and organic semiconductor materials. The thesis work aims to unveil the fundamental structure-property relationships of electronic materials to develop principles of materials design. We particularly focus on their phase evolution and its influence on the physical transport ability and mechanical adaptability, which are salient to the working performance of the electronics. The key contributions of this thesis work are three-fold.

The first key contribution is that we enrich the fundamental understanding of the energy storage mechanisms of Li-ion battery materials. Specifically, by employing the first-principle simulation, we investigate the electronic structure, thermodynamics, structural dynamics, and resulting electronic, mechanical, and thermal properties of battery materials. The energy storage mechanisms are manifested by the phase dynamics of electrode materials during the (de)lithiation process. Distinct phase behaviors during ion transport suggest different lithium storage mechanisms. The electrode materials with high capacity usually exhibit multiple (de)lithiation stages. With the aid of the Delaunay triangulation algorithm and the energetic analysis, we have identified two steps of lithiation mechanisms in  $\alpha$ -MoO<sub>3</sub> cathode and carbon-rich SiOC anode. The  $\alpha$ -MoO<sub>3</sub> materials first accommodate the Li and maintain high atomic ordering through the insertion mechanism, and then react with the excess Li and distort the structure via the conversion mechanism. The excellent capacity of 1230 mAh/g in carbon-rich SiOC anode originates from Li absorption at the percolated nano-void sites, followed by Li reactions with the C phase and Si-O-C units. Besides, the low volumetric strain in the insertion stage of  $\alpha$ -MoO<sub>3</sub> and the inactive segregated carbon network of SiOC contribute to the high structural stability of the two electrode materials, which promise stable and safe cycling performance in operation. The fundamental understanding of the electro-chemo-mechanical behaviors of battery materials sheds significant sights on designing state-of-the-art materials with high lithiation capacity and high structural stability.

The second contribution is that, for the first time, we leverage the phase transformation theory and genetic-algorithm refined modeling to reveal the versatile cooperative transitions in molecular semiconductor materials. Cooperative phase transitions induced by heat, pressure, or light can rapidly modulate the electronic, optical, and mechanical properties of organic crystals which attracts enormous interest in solid state chemistry. The super- and ferroelastic cooperative transitions in organic semiconductor crystals particularly sparked vast attention in the emerging field of organic electronics. It is imperative to reach the mechanistic understanding of the cooperative transitions in the organic solids to develop principles of molecular design. The intricate molecular dynamics and fast phase evolution (usually within seconds) challenge a direct experimental observation, and a few *in silico* studies are limited to the concepts of “local structural fluctuations” and “cooperative molecular motions”. In this study, we systematically study the thermodynamics and evolution of the lattice structure, molecular conformation, and interfacial kinetics of the versatile cooperative transitions in TIPS-pentacene molecular crystals. The quantitative agreement with experiments and theoretical analysis demonstrates that the three-dimensional molecular rotations dictate the lattice transformation in the thermo-, super- and ferroelastic transitions. The interconvertible behavior of super- and ferroelastic transitions represents the distinct directional responses of the molecular crystal under  $\langle 1\ 0\ 0 \rangle$  shear loading. We elucidate for the first time the molecular defects of disclination dipoles and molecular stacking faults associated with molecular twinning. The mechanistic understanding sheds light on devising the cooperative transitions in a variety of organic solids for a new avenue of environmentally responsive organic electronics through molecular design.

The above scientific findings are enabled by the proposed computational methodologies and theoretical framework, such as the lithium intercalation algorithm, genetic algorithm refined force field, and phase descriptors - that makes the third contribution of the thesis. Multiscale atomistic modeling is desired to elucidate the intricate phase dynamics of materials on various time scales and size scales. Nevertheless, there are many formidable challenges associated with the simulation investigation on electronic materials, especially for organic molecules with large atomic size. The small scale *ab-initio* modeling provides accurate descriptions of atomic interaction and electronic structure, but suffers from the expensive computing cost for a simulation size exceeding 200 atoms. Empirical molecular dynamics simulation works efficiently for relatively large length scales ( $\text{\AA} \sim \mu\text{m}$ ) and time scales (fs  $\sim$  ns) but the adopted

empirical atomic potential may undermine the modeling accuracy. To mitigate such a challenge, the revolutionary genetic algorithm is adopted to refine the empirical force field which enables the successful simulation of phase transition of molecular semiconductor materials. Besides, a few *in silico* studies regarding the cooperative phase transitions in organic systems are limited to the concepts of “local structural fluctuations” and “cooperative molecular motions”. The established theoretical framework, including the deformation gradient matrix and Euler rotational analysis, allow us to quantitatively assess the lattice crystallography and molecular motions of materials in the course of phase evolution. The proposed methodologies and framework can find use in exploring the phase dynamics and physico-mechanical behaviors for a variety of environmentally responsive electronic materials.

## **6.2 Outlook for the Future**

Phase dynamics under external stimuli like heat and stress can rapidly modulate the physico-mechanical properties of electronic materials, which incurs vast attention in the emerging field of environmentally responsive electronics. The materials constituting the important players of electronic devices (e.g., batteries and semiconductors) cover from the transition metals, ceramics, and organic molecules. Among them, the molecular solids with the remarkable versatility of chemical design warrant particular attention, which holds the great promise in producing light, low cost, and environmentally benign devices. Chapters 4 & 5 of the thesis present a systematic study on the striking cooperative transitions unveiled in a model molecular semiconductor crystal, which opens new avenues for rapid, reversible modulation of optoelectronic properties in organic electronics. The fundamental understanding, along with the proposed theoretical framework, will help underpin the molecular mechanisms of a variety of adaptive organic solids, wherein the reversible polymorphic transitions are the norm. The potential contributions of the thesis to the emerging field of adaptive organic electronics are discussed below.

Molecular engineering, an experimental trick of changing chemical moieties, is widely adopted to develop organic materials with the desired physico-mechanical properties. Nevertheless, it suffers from massive trials and errors. To devise the intriguing cooperative transitions (e.g., super- and ferroelastic transition) in organic solids, the profound theoretical understanding is desired to inform and guide the molecular engineering process in experiments. In this thesis, the unveiled transition principles of superelastic organic molecules, along with the

established computational framework, can be employed to screen and predict the potential candidate molecules with the mechanical adaptability. For instance, except the TIPS-pentacene molecules, there are many alternative molecular semiconductor materials like TIPS-ADT and TES-ADT, which share similar chemical features - a five-ring backbone and two flower-like side groups. We may question whether the intriguing super- and ferroelastic properties also exist in those analogous semiconductor molecules. The proposed computational methodologies can help us quickly examine the phase dynamics of the candidate molecules and unveil their mechanical behaviors. Later, embracing the power of machine learning techniques, we can pinpoint the transition mechanisms for a myriad of organic solids, and help develop the generic principles to breed a new avenue of adaptive electronics.

The interplay between the charge-transport physics and interface dynamics plays an important role in determining the working performance of adaptive electronic materials. For organic semiconductors, the packing structure of molecules dictates the ability of charge transport. The adaptive organic molecules rapidly alter their packing structure during the cooperative transitions, leading to a sudden variation in the charge transfer mobility. Fig 5.18 in Chapter 5 reveals the heterogeneous charge transfer across the interface domain wall in the twinning configuration of TIPS-pentacene molecules. Such heterogeneous charge domains may breed a new type of organic memory device which can store information in response to external mechanical stimuli. Besides, an investigation on the charge transport across the interface will help underpin the fundamental correlations between the molecular packing and charge transfer mobility.

In addition to the thermomechanical load, other external stimuli like UV-light and an electric field may also induce the cooperative transitions in the organic solids, leading to the emergence of organic adaptronics with photomechanical or ferroelectric properties. For molecular semiconductor materials like TIPS-ADT, the anisotropic charge distribution is anticipated throughout the triclinic lattice cell. The possible electric dipoles of molecules will seek to align with the external electric field, which may alter the packing structure and lead to the polymorphic transition. The adaptive behaviors of organic molecules in response to the various stimuli will open new doors for next-generation smart electronics.

## VITA

# Hong Sun

Department of Mechanical Engineering, Purdue University

585 Purdue Mall, West Lafayette, IN 47906

Email: [sun530@purdue.edu](mailto:sun530@purdue.edu)

### EDUCATION:

**Ph.D. Candidate** of Mechanical Engineering, *08/2015 – Present*

**Purdue University** - West Lafayette, IN

GPA: 3.93/4.0

**Major Advisor: Professor Kejie Zhao**

**Bachelor** of Materials Science and Engineering, *09/2011- 07/2015*

**Xi'an Jiaotong University** - China

GPA: 91/100

### RESEARCH EXPERIENCE:

**Research Assistant**, *08/2015- Present*

**Purdue University** – West Lafayette, IN

- Developed a Machine-Learning refined molecular potential to discover the versatile super-elasticity in a benchmark organic semiconductor by large-scale molecular simulation.
- Employed automated, iterative structural searching algorithm and ab-initio molecular dynamics to investigate the polymorphic transition of organic solids under thermal and mechanical load.
- Studied the microscopic relations between charge transfer and packing patterns in a conjugated polymer.
- Used the DFT+U method and structural evolution algorithm to target the state-of-the-art composition and understand the electronic structure of  $\text{LiNi}_x\text{Mn}_y\text{Co}_z\text{O}_2$  (NMC) materials.
- Employed the Delaunay triangulation algorithm to simulate the lithiation process and to understand the electro-chemical coupling in the polymer derived SiOC material and  $\alpha$  -  $\text{MoO}_3$  material.

**Teaching Assistant**, *08/2017 - 05/2018*

**Purdue University** – West Lafayette, IN

- Course instructor under supervision. Course tutoring along with preparing and grading of weekly homework.

## AWARDS:

- Sigma Xi Award for 2020 Graduate Student Research Competition 2020
- Estus H. and Vashti L. Magoon Award for Excellence in Teaching 2018
- Outstanding Graduate in Xi'an Jiaotong University 2015

## ASSISTANCE IN SUCCESSFUL PROPOSALS:

- NSF CMMI-1941323 (PI: Prof. Kejie Zhao) 2020-2025  
CAREER: Superelastic Organic Semiconductors (SOSs): A new class of molecular crystals of responsive shape memory.

## PUBLICATIONS:

1. **H Sun**, SK Park, Y Diao, E Kvam, K Zhao, "Molecular Mechanisms of Superelasticity and Ferroelasticity in Organic Semiconductor Crystals" *submitted, 2020*.
2. SK Park†, **H Sun**†, H Chung, B Patel, F Zhang, D Daives, K Zhao, Y Diao (†:denotes equal contribution) "Super- and Ferro-elastic Organic Semiconductors for Ultraflexible Single Crystal Electronics", *Angewandte Chemie International Edition* 59 (2020):13004.
3. X Luo, DT Tran, **H Sun**, T Mi, NM Kadlubowski, Y Zhao, K Zhao, J Mei, "Bis-isoindigos: New electron-deficient building blocks for constructing conjugated polymers with extended electron delocalization", *Asian Journal of Organic Chemistry* 7.11 (2018): 2248-2253.
4. **H Sun**, K Zhao, "Atomistic origins of high capacity and high structural stability of polymer derived SiOC anode materials", *ACS applied materials & interfaces* 9.40 (2017): 35001-35009.
5. **H Sun**, K Zhao, "Electronic structure and comparative properties of  $\text{LiNi}_x\text{Mn}_y\text{Co}_z\text{O}_2$  cathode materials", *The Journal of Physical Chemistry C* 121.11 (2017): 6002-6010.
6. R Xu, **H Sun**, LS de Vasconcelos, K Zhao, "Mechanical and structural degradation of  $\text{LiNi}_x\text{Mn}_y\text{Co}_z\text{O}_2$  cathode in Li-ion batteries: An experimental study", *Journal of The Electrochemical Society* 164.13 (2017): A3333-A3341.

7. Y Li, **H Sun**, X Cheng, Y Zhang, K Zhao , "In-situ TEM experiments and first-principles studies on the electrochemical and mechanical behaviors of  $\alpha$ -MoO<sub>3</sub> in Li-ion batteries", *Nano Energy* 27 (2016): 95-102.

### **CONFERENCE PRESENTATIONS:**

- 1<sup>st</sup> NSF PIRE workshop, Manhattan, KS, July 14<sup>th</sup>, 2018.
- Midwest Society of Experimental Mechanics Student Conference, West Lafayette, IN, March 10<sup>th</sup>, 2018.
- 3rd Midwest Mechanics of Materials and Structures Workshop, West Lafayette, IN, August 11<sup>th</sup>, 2017.
- 2017 MRS spring conference, Phoenix, AZ, April 17<sup>th</sup>, 2017.

### **EXTRACURRICULAR ACTIVITIES:**

- Mentored an undergraduate student and a master student on their research projects.
- *Purdue Women in HPC* (High Performance Computing) Program and *Women in Engineering* Program
- Volunteer for Midwest Mechanics of Materials and Structures Workshop (2017,2018)